FEMTOSECOND NONLINEAR SPECTROSCOPIC STUDIES OF NONPOLAR SOLVATION AND CONFORMATIONAL DYNAMICS OF CYANINES AND CAROTENOIDS

By

Michael Minejiro Bishop

A DISSERTATION

Submitted to
Michigan State University
in partial fulfillment of the requirements
for the degree of

Chemistry – Doctor of Philosophy

2013

ABSTRACT

FEMTOSECOND NONLINEAR SPECTROSCOPIC STUDIES OF NONPOLAR SOLVATION AND CONFORMATIONAL DYNAMICS OF CYANINES AND CAROTENOIDS

By

Michael Minejiro Bishop

This dissertation describes two studies on the structurally related conjugated polyenes, cyanines and carotenoids. The first study aims to elucidate the nature of the nonpolar solvation-and excited-state conformational-dynamics of cyanine 5 (Cy5) in bulk water and compare them to the dynamics in the hydration layer of Zn^{II}–substituted cytochrome *c* (ZnCytc). The second study adds insight into the nonradiative decay pathways from the S_2 state of the carotenoids β-carotene and peridinin, the latter of which was studied in solution and in the peridinin–chlorophyll a protein (PCP).

In the first study Cy5 was used as a probe for nonpolar solvation and was studied using multiple nonlinear spectroscopic methods. Three-pulse photon echo peak-shift experiments revealed two timescales for nonpolar solvation in bulk water corresponding to phonon induced and diffusive responses ($\tau = 21$ and 890 fs). These dynamics were significantly different in the hydration layer of ZnCytc, where the fast phonon induced component appears to decay over multiple timescales, and the diffusive component appears to decay over a timescale much greater than the experimental time window ($\tau \gg 2.5$ ps). Extremely fast damping of excited-state

motions in Cy5 was observed in bulk water and in the hydration layer using pump–probe experiments. This fast damping provides experimental evidence for coherent torsional barrier crossing over a transition state toward a twisted conical intersection in accordance with Olivucci's two state two mode theory.[1] An increased damping rate of torsional modes observed in the hydration layer of ZnCytc along with the slowed polar solvation timescales lead to the conclusion that water in the hydration layer is likely more viscous and contains a distinct hydrogen-bonding structure as compared to bulk water.

The second study utilized electric-field resolved transient grating spectroscopy to observe nonradiative decay from the S_2 state of the carotenoids β-carotene and peridinin. An ultrafast kinetic intermediate was observed in both carotenoids, and the differing decay rates of the absorption and dispersion signals of these carotenoids in solution suggested nonradiative decay to a structurally displaced ground state.[54] The time-resolved transient grating absorption spectra of the carotenoids in solution exhibit features consistent with photo-induced excited-state twisting. The transient grating spectra from peridinin in solution revealed the state consistent with the ultrafast intermediate exists at all times when peridinin is in the PCP protein, where the dynamics are relatively static. This implicates the intermediate as a twisted state, and the two state two mode picture developed for cyanines and protonated Schiff bases[1] was applied to carotenoid systems for the first time. It is suggested that these twisting dynamics enhance the intramolecular charge-transfer character of peridinin in the S_1 state, enabling more efficient energy transfer to chlorophyll a.

To Molly

ACKNOWLEDGEMENTS

The work presented in this dissertation would not have been possible without the help, guidance, and support of Professor Warren Beck. His role in my development from a student to a scientist cannot be overstated and I consider the years in Professor Beck's laboratory as the most fulfilling and enjoyable period of my life thus far. I also acknowledge and thank my coworker Dr. Jenny-Jo Mueller for her significant role in alignment and implementation of all of the instrumentation, her support in writing data-analysis software for the Cyanine 5 work, and most importantly for her friendship and comradery. I thank Nolan Shepherd for his help in software writing and optical alignment, particularly with the heterodyne detection system, and I thank Soumen Ghosh and Dan Roscioli for all their contributions to this work and for their eagerness to carry it forward in exciting directions.

I thank my graduate committee, Professors Jim McCusker, John McCracken and Lynmarie Posey for their support and for challenging me intellectually, and I thank Professor Blanchard for lending the Beck group a CCD camera that made heterodyne work possible. I would also like to thank the excellent support staff at Michigan State University, in particular Glenn Wesley for his help in developing some of pivotal hardware during the construction of the photon echo spectrometer. Most importantly, I thank my wife Molly Dobb, whose patience and support on every imaginable level has allowed me to excel in all of my endeavors.

I thank the Department of Chemistry at Michigan State University for Teaching Assistantships (2009–2013), and the College of Natural Science for a Dissertation Completion Fellowship (2013).

Funding for the research conducted over the 2009–2013 period and stipend support during several semesters was obtained from a grant from the National Science Foundation, Biomolecular Systems Cluster, Molecular Biophysics Program, award number MCB-0920101; Principal Investigator: Professor Warren F. Beck; Co-Principal Investigator, Professor Lynmarie A. Posey. Stipend support during the analysis of data and preparation of manuscripts in the carotenoid project was obtained from a grant from the Department of Energy, Basic Energy Sciences, Photosynthetic Systems program under Award number DE-SC0010847; Principal Investigator: Professor Warren F. Beck; Co-Principal Investigator: Professor Harry A. Frank, University of Connecticut.

TABLE OF CONTENTS

LIST OF TABLES

LIST OF FIGURES

LIST OF ABBREVIATIONS

3PEPS, three-pulse photon echo peak-shift

ADP, adenosine diphosphate

ATP, adenosine triphosphate

BChl, bacteriochlorophyll

BPP, Brewster prism-pair

BS, beam-splitter

CCD, charge-coupled device

Chl, chlorophyll

CI, conical intersection

Cy5, cyanine 5

Cy5–ZnCytc, cyanine 5–ligated zinc^{II}-substituted cytochrome *c*

DO, diffractive optic

EET, excitation energy transfer

ESA, excited-state absorption

FC, Franck–Condon

FSS, fluorescence Stokes shift

ICT, intramolecular charge-transfer

LHCII, light-harvesting complex II

LO, local oscillator

LP–SVD, linear prediction-singular value decomposition

MALDI-TOF MS, matrix-assisted desorption/ionization time-of-flight mass

MC, monochrometer

MD, molecular dynamics

MEP, minimum energy path

MRD, magnetic relaxation dispersion

N, conjugation length

ND, neutral density

NHS, N-hydroxysuccinimidyl

NMR, nuclear magnetic resonance

NPQ, nonphotochemical quenching

ODL, optical delay line

OKE, optical Kerr effect

OPA, optical parametric amplifier

PB, photobleaching

PCP, peridinin–chlorophyll *a* protein

PD, photodiode

PSB, protonated Schiff base

SE, stimulated emission

SM, spherical mirror

TG, transient grating

TPM, triphenylmethane

TS, transition state

WP, waveplate

ZnCytc, zinc^{II}-substituted cytochrome *c*

CHAPTER 1

Background and Significance

1.0 Summary

This dissertation describes studies on the structurally related conjugated polyenes, cyanines and carotenoids utilizing a number of femtosecond nonlinear optical techniques. In the first study, cyanine 5 (Cy5) was used as a probe for nonpolar solvation in bulk water and in the hydration shell of Zn^{II}–substituted cytochrome *c* (ZnCytc). Their relative dynamics and timescales are compared in order to better understand the structural nature of hydration shell water. The second study utilizes electric-field resolved transient-grating spectroscopy to study nonradiative decay dynamics of carotenoids in solution and bound within a protein. This work provides insight into the structural nature of these decay intermediates.

The first chapter reviews the background for these two areas with emphases on carotenoid photophysics and the two-state two mode theory proposed by Olivucci *et. al.*[1] Chapter 2 measures the nonpolar solvation dynamics of Cy5 in water using three-pulse photon echo peak-shift (3PEPS) spectroscopy, and compares the excited-and ground-state motions of Cy5 using pump–probe and transient-grating spectroscopies. It is suggested that excited-state dynamics of Cy5 is consistent with the two-state two-mode theory and that coherent and diffusive barrier-crossing occur over a transition-state to a conical intersection (CI). Chapter 3 compares the nonpolar solvation times and excited-state motions of Cy5 in water to that of Cy5 in the hydration shell of ZnCytc. The stretched nonpolar solvation dynamics and

increased damping of torsional dynamics in the hydration shell lead to the conclusion that water in the hydration shell is more viscous and probably contains a different hydrogen-bonding network than that of bulk water.

In Chapters 4 and 5, electric-field resolved transient grating spectroscopy is utilized to study nonradiative decay from the S_2 state of β-carotene and peridinin in solution and peridinin in the peridinin-chlorophyll a protein (PCP). The main conclusion of this work is that evolution on the S_2 excited-state of these carotenoids in solution likely involve twisting coordinates consistent with the two-state two mode theory. The spectral signatures for twisting, which evolve on the ultrafast timescale ($\tau = 30$ fs) for peridinin in solution, exist at all times within PCP. It is suggested that this twisting which is prepared by PCP enhances the intramolecular charge-transfer (ICT) character of peridinin, increasing energy-transfer rates to chlorophyll a.

1.1 Photosynthesis

There are a great variety of photosynthetic light-harvesting structures in nature, but they all serve the same general purpose–to convert photonic energy into a trans-membrane potential, enabling conversion of ADP to ATP. The light-harvesting antennae in Photosystem II contain carotenoid and chlorophyll (Chl) pigments bound within the protein architecture and typically utilize the chlorophyll pigments for absorption and long-range transfer of excitation energy. This excitation energy is typically funneled to the reaction center via the weak coupling Förster mechanism where charge-separation reactions allow the splitting of water to form protons and O_2. For this overall process to be efficient, the rate of excitation energy transfer (EET) must be sufficiently fast to compete with deactivation via fluorescence or nonradiative processes, and indeed EET to the reaction center occurs on the ~100 ps timescale, which is significantly faster than the fluorescence lifetime of chlorophyll *a* (~1 ns).[2] The overall efficiency of EET to the reaction center is ~95%, where the charge separation efficiency is near unity.[2] These excited-state species within the protein can be reactive, especially under high-light conditions, and it is thought that the carotenoid's primary role is photoprotection, or deactivation of excess excitation and neutralization of reactive species.[2,3]

Detailed knowledge of photosynthetic mechanisms has become possible in large part due to advances in structural biology, allowing for the high-resolution structural determination of many important photosynthetic proteins and protein complexes. The high resolution structure of LHCII, the antenna protein in the Photosystem II supercomplex in green pea, by x-ray diffraction[4,5] is shown in

Figure 1.1. This provides a high-resolution look into the detailed protein structure and arrangement of pigments. LHCII contains multiple varieties of carotenoids as well as Chl *a* and Chl b molecules, leading to very complex pathways for EET. LHCII is trimeric, with each subunit containing 14 Chls (8 Chl a, 6 Chl b) and two carotenoids. The Chl a and Chl b pigments are packed tightly together in clusters of 2-4 molecules. This tight packing of Chl pigments allow for strong-coupling, where exciton relaxation occurs within a few hundred femtoseconds of photoexcitation, and subsequent long-range energy transfer to one of a few low energy Chl *a* molecules within the supercomplex occurs in about 20 ps.[2] In LHCII, the carotenoid species are bound both within the protein matrix and near the surface, often adopting nonlinear and twisted conformations, due to protein packing forces and the carotenoid's proximity to charged residues. One of the primary aims of this dissertation is to better understand the role of twisted carotenoid states, both in solution and in protein systems, and impact of these states on energy transfer processes.

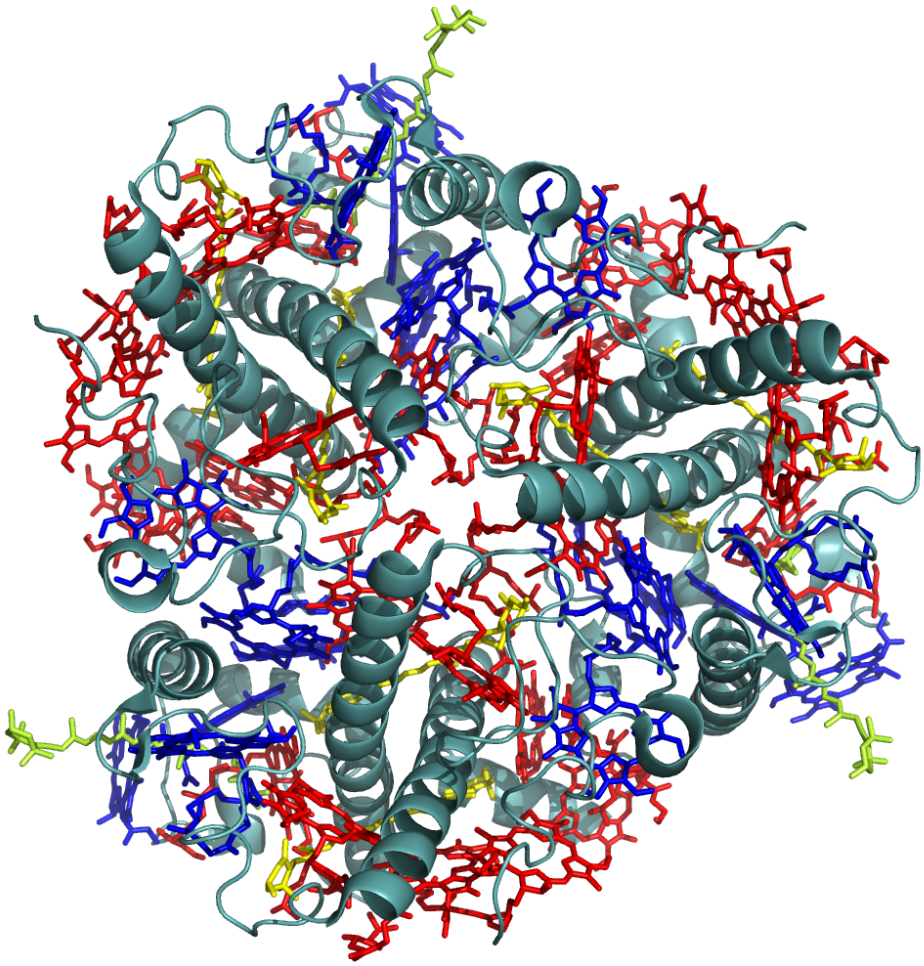

Figure 1.1. Structure of the light-harvesting complex II (LHCII) trimer from *Pisum sativum* (green pea) (2BHW.pdb) determined by Standfuss *et al*.[5] For interpretation of the references to color in this and all other figures, the reader is referred to the electronic version of this dissertation.

1.2 Carotenoid Photochemistry and Photophysics

Carotenoids are abundant in nature and are found in the tissues of both plants and animals, but are only synthesized by plants and microorganisms.[3] Carotenoids play diverse roles in organisms: They are known to scavenge singlet oxygen and other radical species[2,3,6] and may play a role in mitigating disease, such as certain kinds of cancer and cardiovascular disease via their antioxidant properties.[7] In light harvesting, carotenoids fill gaps left by Chl spectra, where the solar spectrum is

most intense, but typically play only a minor, yet nontrivial role in EET as short-range energy transfer donors to Chl. A number of studies on LHII-type proteins have estimated that EET efficiencies from carotenoids to Chl is highly variable between systems (35-70% *Rps. acidophila*, 80-100% *Rb. sphaeroides*) and dependent on the specific carotenoid donor.[2] As mentioned above, the primary roles of carotenoids in green plants and purple bacteria are thought to be the regulation of energy flow to and from Chl molecules and photoprotection via non-photochemical quenching (NPQ).

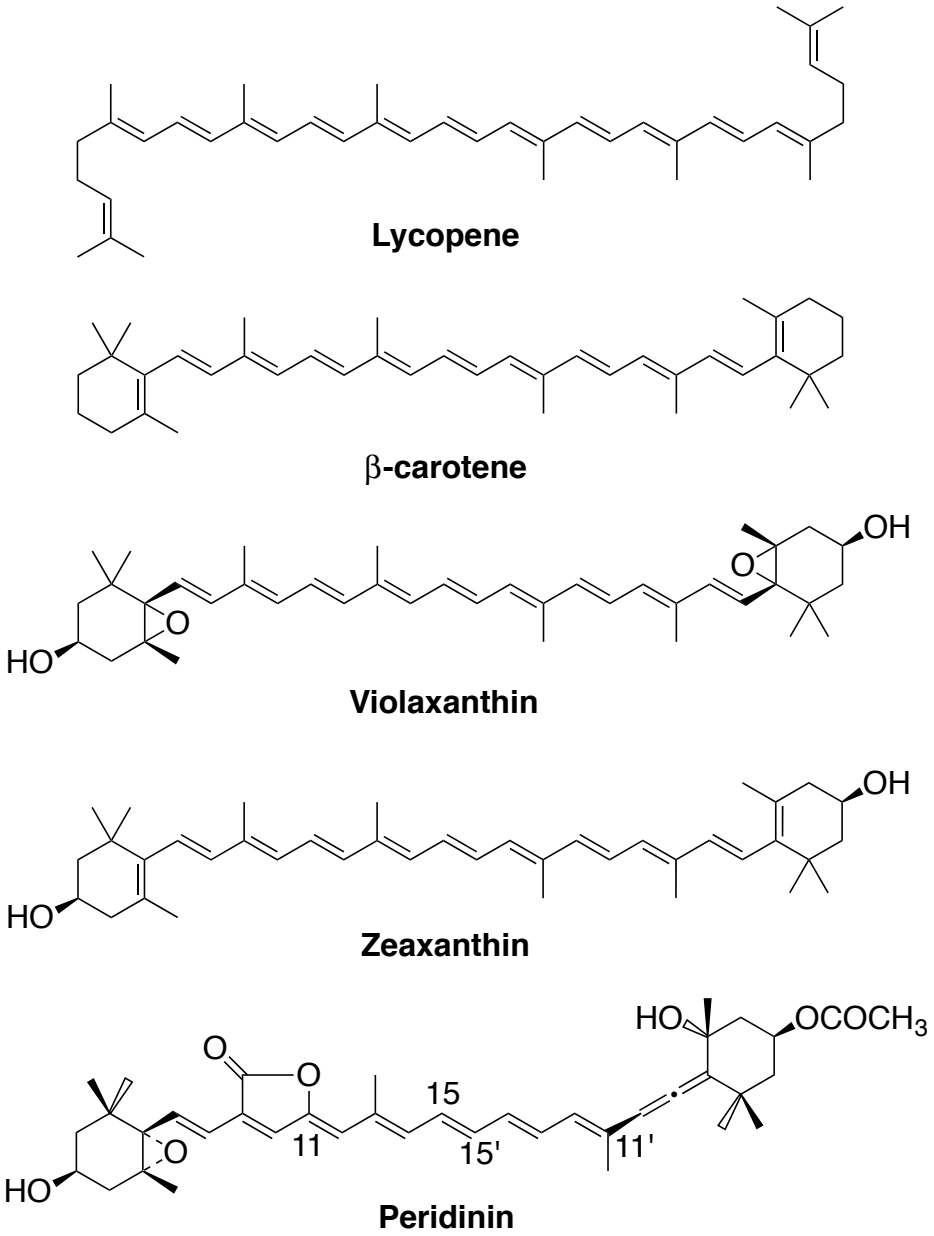

Figure 1.2. Structures of common carotenoids.

1.2.1 Carotenoid Photophysics

Carotenoids belong to a class of linear conjugated polyenes with extended π-electron systems of varying conjugation lengths (N), which contain various functional groups and end groups. Figure 1.2 shows a few examples of common carotenoids. Many of the interesting physical properties of carotenoids are

governed by the symmetry of the molecule. Carotenoids mostly follow the symmetry rules of the C_{2h} point group; the symmetry group to which many of the planar structures belong. Figure 1.3 shows a schematic energy-level diagram of a prototypical carotenoid with the associated symmetry labels, highlighting the transitions that lead to nonlinear optical signals. The S_0 and S_1 states have A_g^- symmetry, while the S_2 state has $1B_u^+$ symmetry. Single-photon transitions between states with similar symmetry and/or parity (i.e. $S_0 \rightarrow S_1$) are forbidden, leading to the *dark* nature of the S_1 state from the ground state, and indeed $S_0 \rightarrow S_2$ is the lowest energy allowed transition. Weak fluorescence, however, is observed from the S_1 state,[3,8] showing this state is populated from nonradiative decay from the S_2 state. The energy gaps and relative spacing of the carotenoid states vary greatly depending on conjugation length and the presence of functional groups, and even subtle changes in the carotenoid can change the function within a photosynthetic complex.[2]

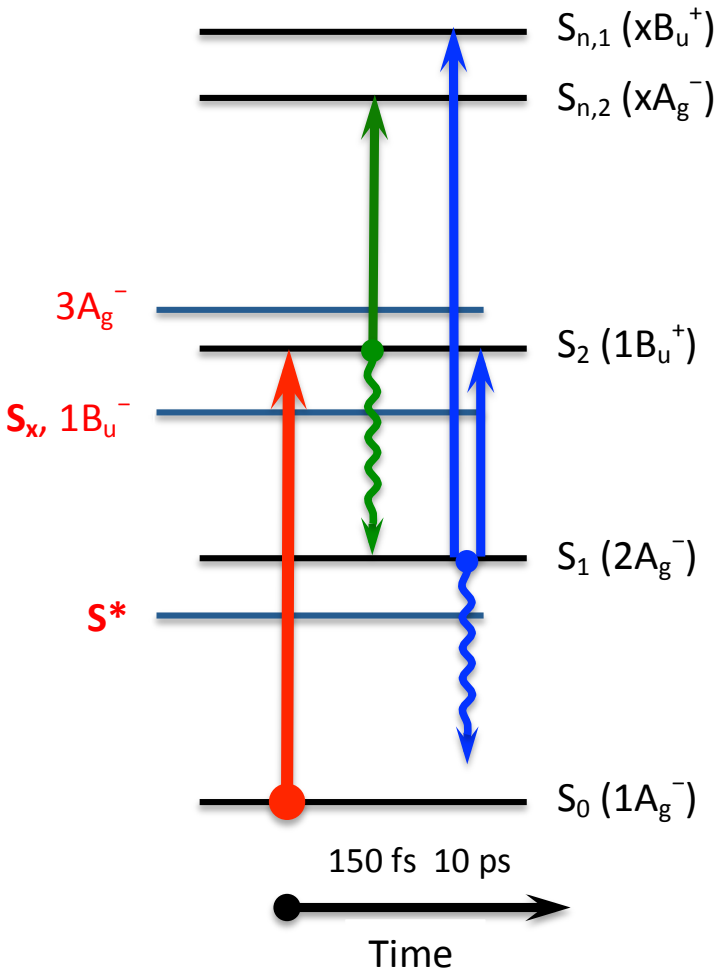

Figure 1.3. Electronic energy levels of carotenoids and transitions that contribute to nonlinear optical signals following optical preparation of the S_2 state, after Polívka and Sundström.[9] The one-photon transitions of most carotenoids effectively follow the selection rules for molecules belonging to the C_{2h} point group; transitions between states of the same symmetry (g→g, u→u) and pseudoparity (+→+, −→−) are electric-dipole forbidden.[10,11] The first strongly allowed optical transition is $S_0 \rightarrow S_2$. Weak fluorescence is observed from the formally dark S_1 state,[12,13] which shows that the S_1 state is rapidly accessed via internal conversion. Dark states suggested by previous work are marked by blue lines and red labels. Nonradiative decay transitions that deactivate the S_2 state are indicated with wavy arrows; excited-state absorption transitions that contribute to pump–probe and transient-grating signals are shown as solid arrows. The timescale increases from left to right in the diagram.

1.2.2 Non-photochemical Quenching

Carotenoids are known to quench various different types of reactive Chl excited states (singlet and triplet) as well singlet oxygen.[2,3] The schematic diagram in

Figure 1.4 shows energy flow within carotenoids and Chls and EET transfer between weakly coupled carotenoids and Chls. For certain carotenoid–Chl pairs, the S_2 and S_1 states are higher in energy than the Chl Q_x an Q_y states, while the triplet state is lower in energy. This leads to favorable energy transfer from carotenoid to Chl while simultaneously being able to deactivate long-lived triplet Chl states freeing the Chl to absorb subsequent photons, thereby increasing overall EET. It should be obvious that tuning of the energies of the carotenoid states relative to the Chl will effect the energy transfer rates and can even change the direction.

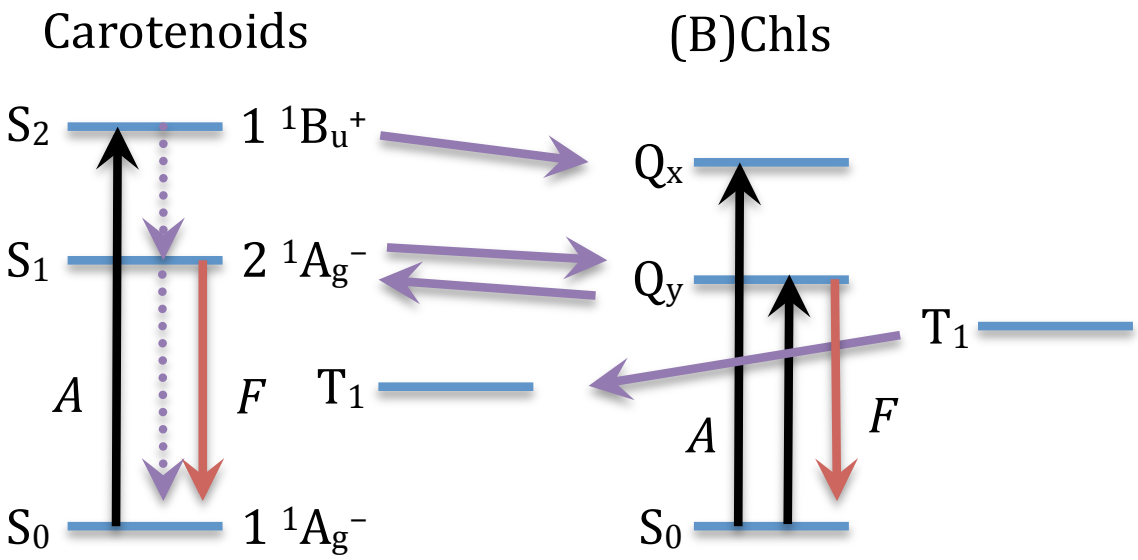

Figure 1.4. Energy level diagram depicting the relative positions of the low-lying singlet and triplet states of carotenoids and (B)Chls and various pathways for intra- and intermolecular energy conversion. The state representations are those for the C_{2h} point group. Dashed arrows represent intramolecular non-radiative processes; energy-transfer pathways are depicted with horizontal arrows.

Under high photon flux within the LHCII protein, the carotenoid violaxanthin is known to be enzymatically converted to zeaxanthin, whose presence is known to stimulate quenching of Chl *a*.[14-16] Frank *et al.*[17] proposed a so-called "molecular

gear shift" mechanism for NPQ under the assumption that the S_1 state energy for violaxanthin was above the Chl *a* Q_y state and the corresponding zeaxanthin state's energy was below the Chl *a* Q_y state. In this picture, the conversion of violaxanthin to zeaxanthin would "turn on" quenching of the Chl *a* Q_y state, explaining zeaxanthin's role in NPQ. Later direct measurements of the S_1 state energies of violaxanthin and zeaxanthin uncovered that S_1 state energies were above the Chl *a* Q_y state for both carotenoids in solution and in the LHCII protein, invalidating the gear-shift mechanism for zeaxanthin quenching. It was subsequently shown that zeaxanthin does indeed play a direct role in Chl a excited-state quenching,[18,19] but it has since been proposed that the essential function of zeaxanthin in NPQ involves the promotion of changes in the structure or organization of the light harvesting complex that is favorable for quenching. Crofts *et al.*[20] show evidence for a change in protein structure in the presence of zeaxanthin that facilitates the formation of a Chl *a* exciton pair which then plays a role in quenching. This example illustrates how the change in structure of the carotenoid or surrounding structure can affect energy transfer and quenching mechanisms and highlights the importance of chromophore-protein interplay.

1.2.3 Carotenoid Nonradiative Decay and Dark States

The resonant S_2 state in carotenoids is known to have a short lifetime ($\tau < 100$ fs) that decays non-radiatively to the S_1 state. Between the S_2 and S_1 states exist one or more states that have been predicted by theory[21] and observed in experiment.[22-26] The precise timescales and nature of these intermediate states are

a matter of hot debate. Calculations involving $S_2 \rightarrow S_1$ internal conversion rates of carotenoids of varying lengths[12] and subsequent experiments[27] showed that these rates do not follow the energy gap law; while the $S_2 \rightarrow S_1$ energy gap increases with increasing conjugation length, the S_2 lifetimes decreased for longer carotenoids. This anomalous behavior became the grounds for the plausible existence of an intermediate state mediating the $S_2 \rightarrow S_1$ internal conversion. Although a number of femtosecond nonlinear spectroscopic studies have provided evidence for the existence of intermediate-energy states between the S_2 and S_1 states, it is still unclear whether such intermediate states are involved in $S_2 \rightarrow S_1$ internal conversion.

The fist spectroscopic evidence for an intermediate state mediating $S_2 \rightarrow S_1$ internal conversion came from transient absorption studies of neurosporene by Zhang and coworkers[28] who assigned a near-infrared band (800-950 nm) as a transition coming from the $1B_u^-$ state predicted by Tavan and Schulten.[21] It was concluded that the S_2 state decays on the <70 fs timescale, which subsequently decays to the S_1 state on the $\sim$230 fs timescale for neurosporene. This same intermediate-type behavior was later observed in other carotenoids.[29]

In transient absorption studies of β-carotene and lycopene with 10 fs pulses, Cerullo and coworkers observed a 12 fs decay of the S_2 state and the corresponding population rise of a spectrally resolved state (near 800 nm).[30] This state was attributed to a distinct electronic state, S_x, where subsequent $S_x \rightarrow S_1$ internal conversion occurs on a 150 fs timescale. Similar to previous studies, the S_x state was assigned to the $1B_u^-$ state. The observable "S_2 emission" was then attributed as

arising form the $1B_u^-$ state, a transition that is formally symmetry forbidden. The authors attributed this emission as possibly occurring via vibronic coupling of the S_2 and S_x state due to their small energy difference, or more likely a departure from ideal C_{2h} symmetry via twisting or bending coordinates in the carotenoid excited states.[30]

A number of four wave mixing experiments have studied radiationless decay in carotenoids. Femtosecond resonance Raman experiments on β-carotene in cyclohexane showed the rise of a C=C stretching signal characteristic of the S_1 state, commensurate with the decay of a C–C stretching signal characteristic of the S_2 state.[31] It was concluded that no intermediate state was needed to account for the Raman observations. Degenerate four-wave mixing experiments on β-carotene showed time-evolving oscillatory behavior that confirmed S_1 behavior during the supposed intermediate's timescale, again suggesting that no intermediate is needed to explain the dynamics. Christensson *et al*. performed three-pulse photon echo peak-shift (3PEPS) measurements on lycopene and astaxanthin, which have similar effective conjugation lengths, led the authors to suggest that the S_2 state decay occurs via a conical intersection where the solvent plays a role.[32] It was concluded that the ring end-group structures in astaxanthin slowed the trajectory toward a torsional conical intersection on the S_2 state surface compared to the linear lycopene molecule by a factor of two (S_2 lifetimes 80 and 160 fs respectively).

In more recent 2D optical experiments of the LH2 complex in purple bacteria and the corresponding isolated carotenoids,[24,25] Ostromumov and coworkers observed an intermediate (denoted X) assigned to the $1B_u^-$ state. This X state was

shown to have coupling to the S_2 state in the isolated carotenoid and in the LH2 complex, and in the latter case, the X state showed coupling to the Q_x state of bacteriochlorophyll *a*, implicating this intermediate as an energy-transfer state. Interestingly, this intermediate state was detected as a bleaching signal from the S_0 ground state in contrast to all other previous experiments where the ESA signals in this spectral region were dominant. The bleaching signal for this formally forbidden $S_0 \rightarrow S_x$ transition was attributed to possible intensity borrowing from the S_2 state due to nontotally symmetric vibrations via a Herzberg-Teller mechanism. In both the Cerullo[30] and Ostroumov pictures, the dipole strength of the intermediate can be explained by distortions from the planar C_{2h} configuration.

There are a number of problems with assigning this intermediate to the $1B_u^-$ state predicted by Tavan and Schulten,[21] as explained in a review article on carotenoid dark states by Polivka and Sundstrom.[9] The first of these problems is accounting for the "S_2 emission", which actually occurs during the intermediate's timescale. This has been explained due to possible mixing of the S_2 and $1B_u^-$ state, which would tend to increase the dipole strength of the $1B_u^-$ state,[24,30] but if this were true, increasing the conjugation length should widen this gap and decrease mixing. Emission from this $1B_u^-$ state should also cause an asymmetry in the overall emission spectrum of the carotenoid that becomes less symmetric with decreasing conjugation length. This trend is true with β-carotene and leutene,[33] which contain β-ionyilidene rings (similar to β-carotene), but this effect is not observed in a series of linear carotenoids with N = 9-13.[34,35] A reasonable explanation for the spectral asymmetry of β-carotene and leutene could be due to enhanced twisting afforded by

the steric interactions of the terminal rings,[36] which would be further amplified for carotenoids with shorter conjugation lengths.

If this intermediate were the $1B_u^-$ state, then the strong absorption band should correspond to a $1B_u^- \rightarrow 1A_g^+$ transition. The N dependence of the $1A_g^+$ state can be easily determined from the absorption spectra of *cis* carotenoids, where transitions to this state from the ground state become allowed.[9] The N dependence of the proposed $1B_u^-$ state was determined by resonance Raman experiments[22] and supported by calculations from Tavan and Schulten.[21] Figure 1.5 shows the relative N dependence of the $1B_u^-$ and $1A_g^+$ states and predicts a blue shift with increasing N. The transient absorption spectra assigned to the $1B_u^-$ state do not show this trend: Polli *et al.*[37] show peaks at the same wavelength (~900 nm) for N=15 and 9, while they should be spaced by ~3000 cm^{-1}. This transition was seen in β-carotene at ~1000 cm^{-1} for N=10. Koyama *et al.*[28,38] saw shifts from 900 to 1050 cm^{-1} for N=9 and 13, the opposite of what is predicted form Figure 1.5. Given this evidence, the assignment of the transient absorption NIR peaks near 1 μm appear poorly assigned to the $1B_u^-$ state.

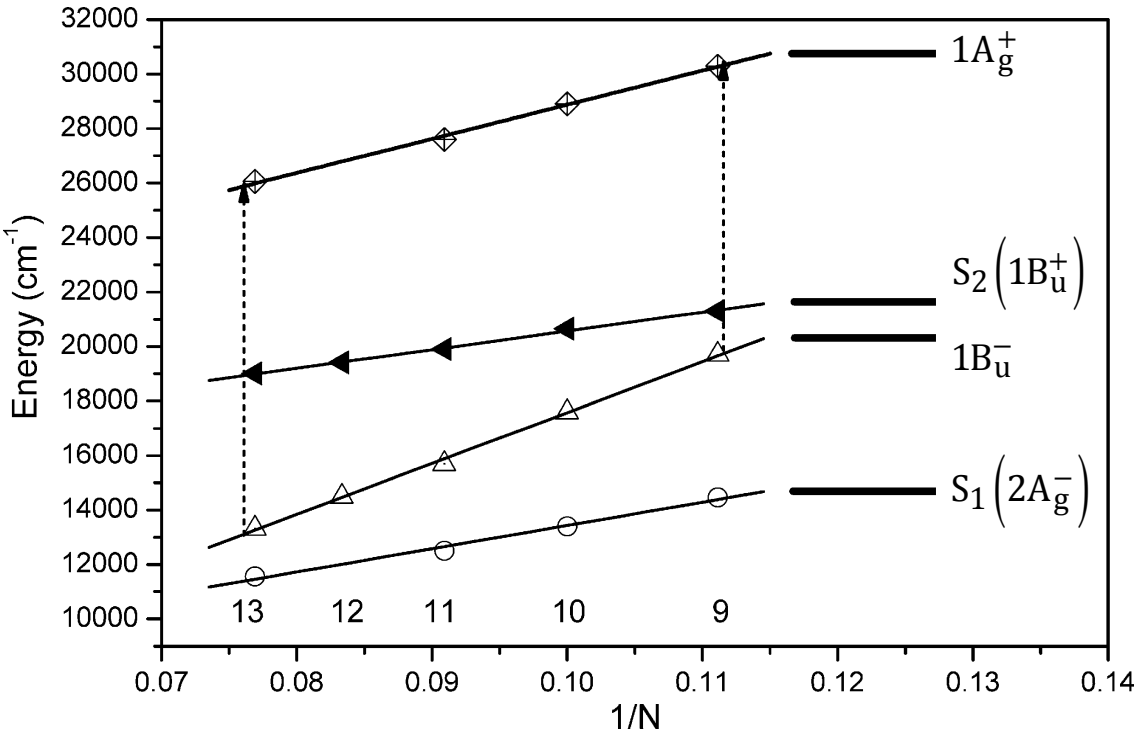

Figure 1.5. Conjugation length (N) energy-dependence of various carotenoid excited states. The S_1 state energies (open circles) are determined from S_1–S_2 spectra,[3] the $1B_u^-$ state energies are determined from resonance Raman profiles,[22] and the S_2 and 1Ag+ energies are determined from absorption spectra. The dotted arrows show the expected energies of transitions between the $1B_u^-$ and $1A_g^+$ states for N=9 and 13. (Used with permission from a review by Polivka and Sundstrom[9]. Copyright 2009 Elsevier.)

There also exists an S^* state in carotenoids that can be readily identified as a blue shoulder on the S_1 band of the transient absorption spectrum of spirilloxanthin and similar carotenoids.[26] This state was first assigned as a hot ground state[39] in a long N = 18 homolog of β-carotene, and was later supported by pump-dump probe experiments on spirilloxanthin by Wholleben.[23] This hot ground state's sub-100 fs time-evolution in transient absorption experiments, however, makes it unlikely to be a hot ground state populated through nonradiative decay processes. A more likely explanation for this hot ground state behavior in these experiments would be that the signals generated arise from a stimulated resonance Raman mechanism.

Frank *et al*. proposed that the S^* state was a twisted conformation of the S_1 state using the results from a series of transient absorption studies of different carotenoids at varying temperatures and in varying solvents and comparing them with electronic structure calculations.[40-42] In this model, a portion of the S_2 excited state population undergoes a conformational change before relaxing to an S_1-like state, creating a conformationally distinct S^* state. It has also been observed that the S^* signal is enhanced when bound in a protein compared to in solvent,[23,43] which is consistent with the twisting picture because carotenoid structures strongly deviate from linearity when bound in the protein matrix.

1.3 The Peridinin-chlorophyll *a* Protein

The light harvesting antennae of most dinoflagellates utilize the peridinin carotenoid whose blue-green absorption is responsible for the so-called red tides. In most light harvesting structures, such as those from green plants and purple bacteria, carotenoids play only a minor role in light harvesting due to the short lifetime of the strongly absorbing S_2 state and the small dipole strength of the subsequently populated S_1 state.[2,9] In the peridinin-chlorophyll *a* protein (PCP), isolated from the dinoflagellate *Amphidinium cartarae*, however, the peridinin carotenoid plays the role of the primary light-harvesting unit. EET from peridinin to Chl *a* molecules is unusually efficient (> 90%) owing to a number of structural adaptations. The peridinin carotenoid itself contains an allene group and a lactone ring in conjugation with the extended π network of the polyene which is thought to invoke the ICT character,[8] which is thought to be the origin of the increased EET

efficiencies to Chl *a* in PCP. The arrangement of the pigments in the protein structure has also evolved to maximize EET efficiencies.

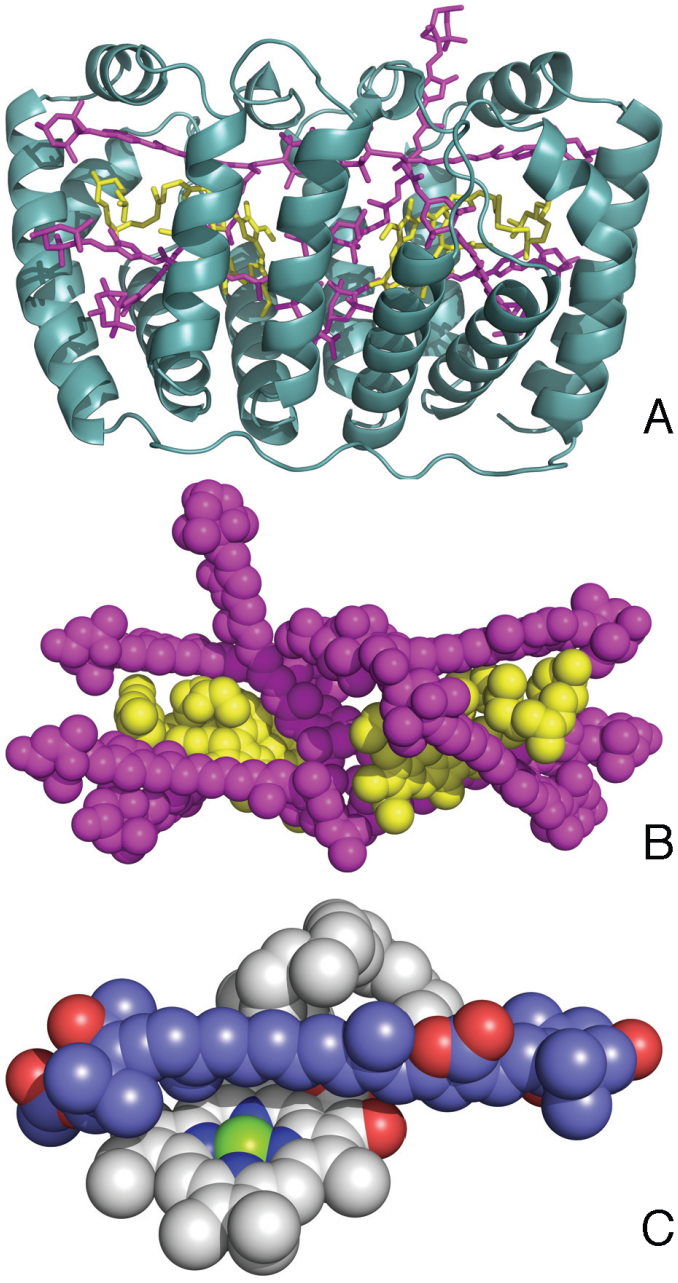

Figure 1.6. Structure of the peridinin–chlorophyll *a* protein (PCP) from *Amphidinium carterae* (1PPR.pdb) determined by Hofmann et al.:[44] (a) single subunit showing peridinin (magenta) and Chl *a* (yellow) chromophores; (b) space-filling view of chromophores after 180° rotation around the *z* axis; (c) Chl *a* and peridinin complex.

The X-ray crystal structure of one subunit of PCP (Figure 1.6) consists of a basket of α helices that binds a dense cluster of eight peridinin carotenoids and two Chl *a* chromophores in a C_2-symmetric, two-domain assembly. The two Chl *a* molecules are approximately 17 Å apart. In contrast, the four peridinins in each domain are effectively in van der Waals contact (3.3 to 3.8 Å separation) with a central Chl *a*, and one peridinin is especially closely associated.[44] Despite having all of this structural information at hand, the mechanisms that mediate energy transfer from peridinin to Chl *a* via the S_2 and S_1 states are incompletely understood. It remains to be established how the dark (electric-dipole forbidden) S_1 state of the peridinins is coupled to that of the Chls so that energy transfer is efficient, and it is an open question whether the peridinin singlet excited states are delocalized over the cluster of chromophores in a given domain.[45]

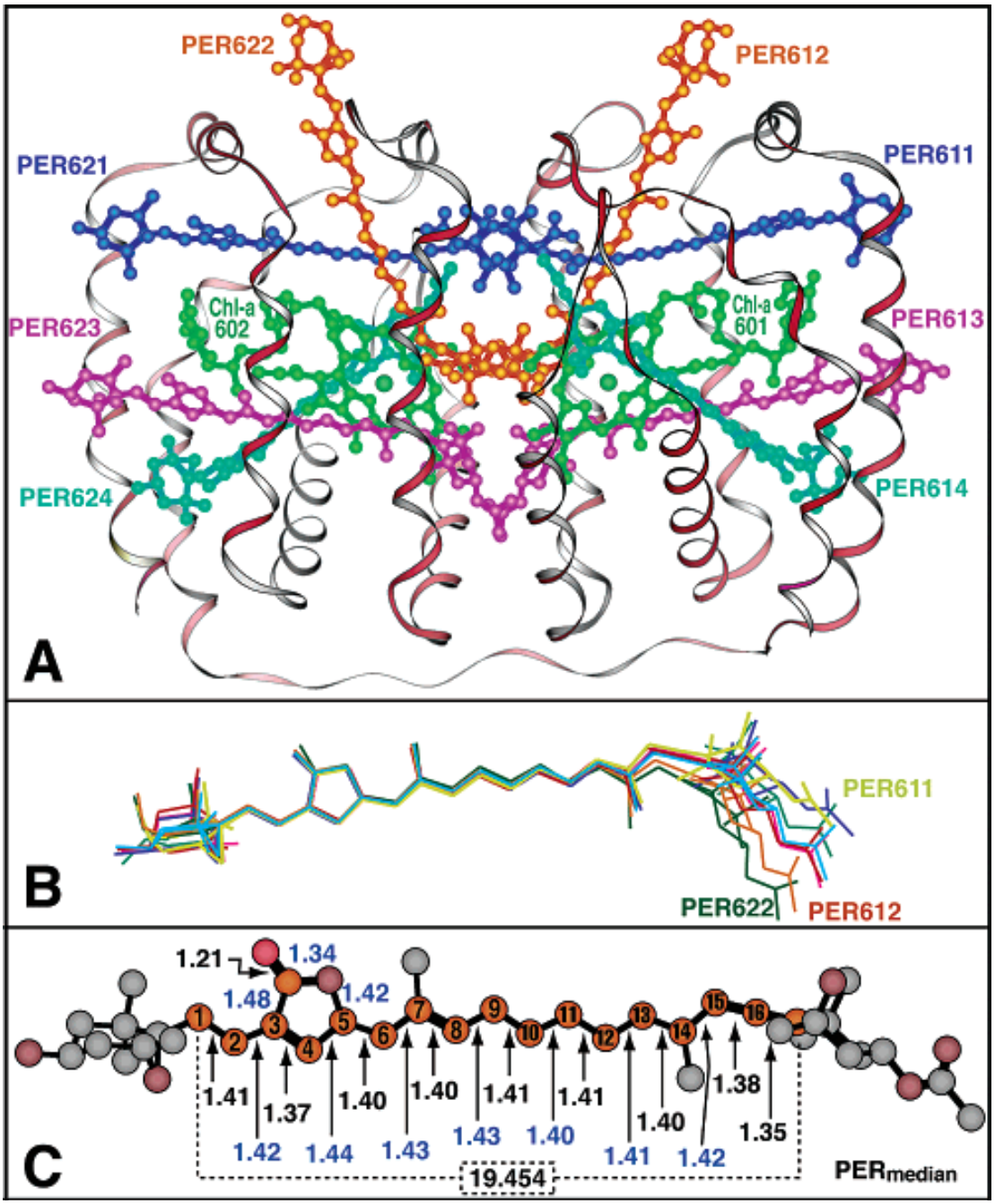

Figure 1.7. Structure of the chromophores in each PCP subunit: (a) four peridinins (Per) and one Chl *a* are located in each of the two domains. The numbering is that in the X-ray crystal structure (1PPR.pdb),[44] and the coloring reflects the pseudo 2-fold symmetry axis; (b) comparison of the conformation of the peridinins showing the distinctive distortions of the symmetry related Per 622 and Per 612 chromophores; (c) median structure of the peridinins. (Used with permission from Shima *et al.*[46] Copyright 2003 American Chemical Society.)

Another optimization of structure in PCP that is thought to enhance the yield of the S_1-state energy-transfer channel to the Q_y state of Chl *a* comes from changes in the conformations of the peridinin chromophores in a given subunit (Figure 1.7) due to packing forces in the folded PCP protein. Although all of the peridinin chromophores in PCP are distorted from the gas-phase minimum-energy structure obtained from electronic structure calculations, the conformations of Per 612 and Per 622 are especially strained in the PCP protein; observe that the allene end of these chromophores is bent and twisted well away from the other peridinins. While the excited-state properties of the other peridinins are similar to those of the isolated all-trans molecule in solution, Per 612 and Per 622 are predicted to have significantly blue-shifted spectra (Figure 1.8) and an inverted ordering of the S_1 and S_2 states. Frank and coworkers conclude that these changes result in a tenfold enhancement of energy-transfer yield that arises from mixing in of the symmetry allowed $1B_u^+$ character of the S_2 state and to an increase in the overall lifetime.[46]

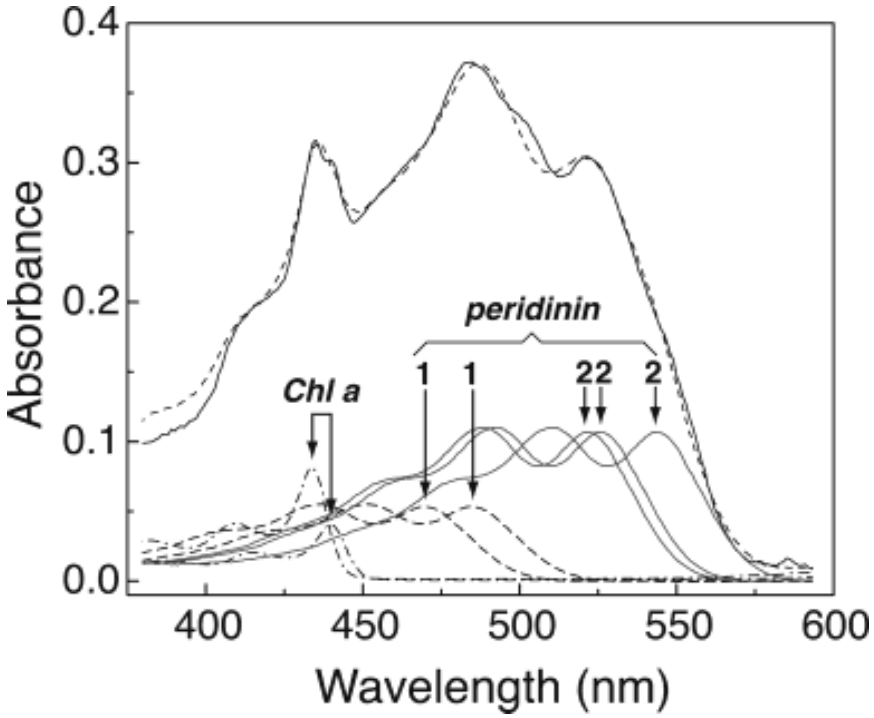

Figure 1.8. Analysis of the absorption spectrum from PCP at 10 K in the Soret and peridinin absorption regions. The calculated spectrum (dashed line) is a linear combination of the spectra from two Chls (dashed dotted) and eight peridinins (solid). The two blue-shifted peridinin spectra labeled 1 arise from Per 612 and Per 622. (Used with permission from Shima *et al*.[46] Copyright 2003 American Chemical Society.)

Note that the discussion of the PCP absorption spectrum reviewed above treats the peridinins as having localized excited states, but calculations by Damjanovic *et al*.[45] indicate that the peridinins interact with each other strongly enough in the S_2 state that a ladder of exciton (delocalized) states is produced. In contrast, because the S_1 state has a much lower dipole strength, a set of localized peridinin excited states would be expected. The results obtained recently by Frank and coworkers[47] favor the localized picture even for the $S_0 \rightarrow S_2$ absorption transition: they observed that a single mutation near Per 614 (N89L, changing an asparagine residue to a leucine residue) blue shifts the spectrum of that chromophore without

altering those of the other peridinins. Moreover, the peridinin component spectra have lineshapes that resemble that of peridinin in solution. The Per 614 chromophore has the strongest electronic interaction with the Chl *a* in its domain. Nevertheless, because the ICT character and the structural deformations of Per 612 and Per 622 are hypothesized to enhance the dipole strength of the peridinin chromophore. Whether or not delocalized excited states play a role in energy transfer to Chl *a* deserves further attention. The presence of even an intermediate level of exciton coupling can be sensed in 2D spectra by observing off-diagonal cross peaks between donor and acceptor states as shown previously in work on marine algae[48,49] and in the Fenna-Matthews-Olson complex.[50]

Recent homodyne transient-grating studies were performed on peridinin in solution and in the PCP protein, utilizing ~40 fs pulses centered at 515 nm.[51] The dynamics of peridinin in solution showed a large (likely solvent-induced) spike, followed by a fast, solvent-independent rising component that was assigned to decay of the S_2 state with a timescale of ~75 fs. The subsequent slower, solvent-dependent rising component with timescales of 600 fs and 2.5 ps in acetonitrile and benzene respectively was assigned to equilibration of the S_1 state. The solvent sensitivity of the S_1 state is thought to arise from the ICT character of this state, so this data further strengthens the idea that the S_1 and ICT states are strongly coupled. The homodyne transient grating of PCP showed an initial spike followed by a monotonic decay. The differences in the behavior of the signals were reconciled utilizing a model that accounted for energy transfer to Chl *a*, and the observed timescales corresponding to the S_2 and S_1 states (700 fs and 2.4 ps) were

consistent with previous pump-probe experiments.[52,53] It has been argued that timescales derived from the direct fitting of homodyne transient-grating signals of multi-level systems may not be physically meaningful because the homodyne signal consists of the squared sums of the absorption and dispersion signals.[54] These absorption and dispersion signals have different signs and amplitudes at specific wavelengths corresponding to the various electronic transitions in multilevel systems, so the interplay of these competing signals will manifest in the homodyne signal to form timescales that do not directly report the kinetics of the system, at least not in a straightforward manner.

1.4 Polyene Twisting and the Two-State Two-Mode Theory

Olivucci and coworkers discuss the isomerization of cyanines and protonated Schiff bases (such as retinals in rhodopsin and bacteriorhodopsin) in terms of a reaction coordinate consisting of two classes of normal modes.[1] The potential energy surface-calculations were carried out using a complete active space (CASSCF) with the 6-31G basis set as implemented in Gaussian[1] on simple cyanines (NH_2 terminated polymethine chains). The reaction coordinate should be considered in this picture as a minimum energy path (MEP) on the multicoordinate potential-energy surface. Figure 1.9 shows the reaction trajectories (black lines) on the potential energy surfaces for short cyanines (Figure 1.9a) and longer cyanines and PSBs (Figure 1.9b). The potential energy surfaces for short and long cyanines differ in two distinct ways. The Franck-Condon (FC) region for the short cyanines (e.g. 1144-C) is sloped along bond-alternation coordinates (stretching of C–C and

C=C bonds of the conjugated polyene backbone) and along torsional modes, where the bond-alternation coordinates correspond to the totally symmetric modes. Both the bond-alternation and torsional modes exhibit resonance Raman activity because of the forces along those coordinates in the FC geometry. The FC region for longer cyanines is different in having a minimum along the torsional coordinates as shown in Figure 1.9b.

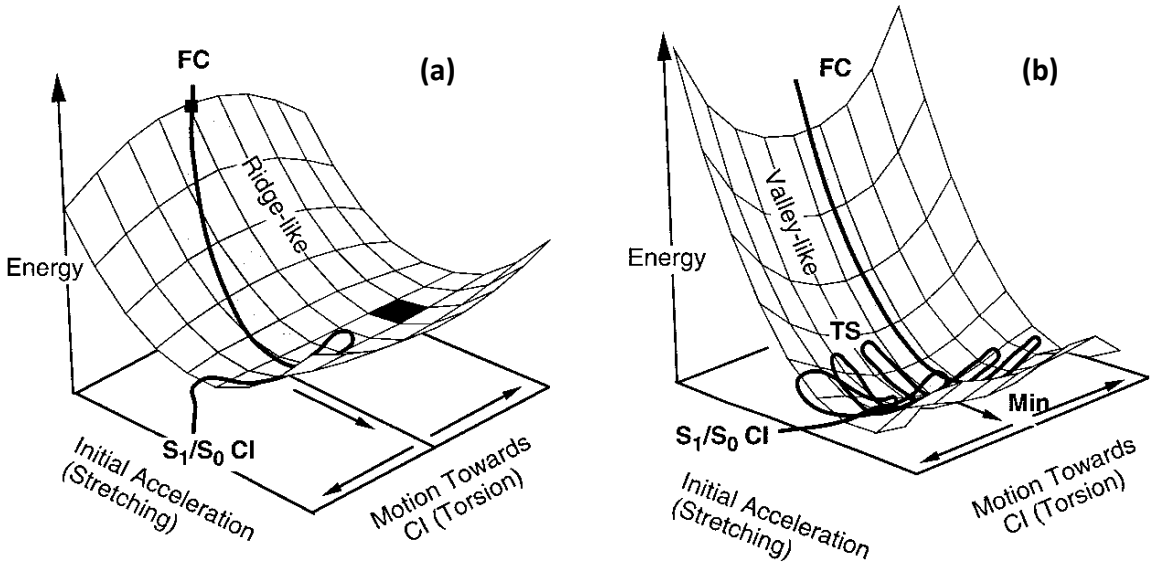

Figure 1.9. Potential energy surfaces near the Franck–Condon (FC) geometries for (a) short cyanines and (b) longer cyanines and PSBs along two normal coordinates: stretching and torsion. The black lines show minimum-energy pathways (MEPs) that lead to the conical intersection. Torsional motion is strongly coupled to stretching coordinates near the FC geometry in short cyanines, but weakly coupled to stretching coordinates in longer cyanines and PSBs due to a minimum in torsional potential existing near the FC geometry for these molecules. (Used with permission from Olivucci *et al*.[1] Copyright 2000 American Chemical Society.)

The short cyanines evolve structurally initially form the FC region by stretching and twisting; the two motions are said to be coupled.[1] In contrast, the potential energy surfaces for the longer cyanines have a minimum along the torsional coordinates at the Franck–Condon geometry, so the initial evolution is purely along

the stretching modes. The torsional modes are activated in the longer cyanines only after the system evolves significantly along the stretching coordinates and after perhaps only a few vibrations of the stretching coordinates. The shorter PSBs exhibit a saddle point where the stretching modes and the torsional modes intersect; the longer PSBs and cyanines have a barrier along the stretching modes prior to the intersection with the torsional modes that increases in height as the length of the polyene backbone increases. As the system approaches the minimum along the stretching coordinates, an increasing slope along the twisting coordinates brings the system to a conical intersection (CI) with the ground state. Figure 1.10 shows the potential energy along a single-dimension reaction coordinate corresponding to twisting for short cyanines such as 1144-C (Figure 1.10a) and longer cyanines such as cyanine 3 and cyanine 5 (Figure 1.10b).

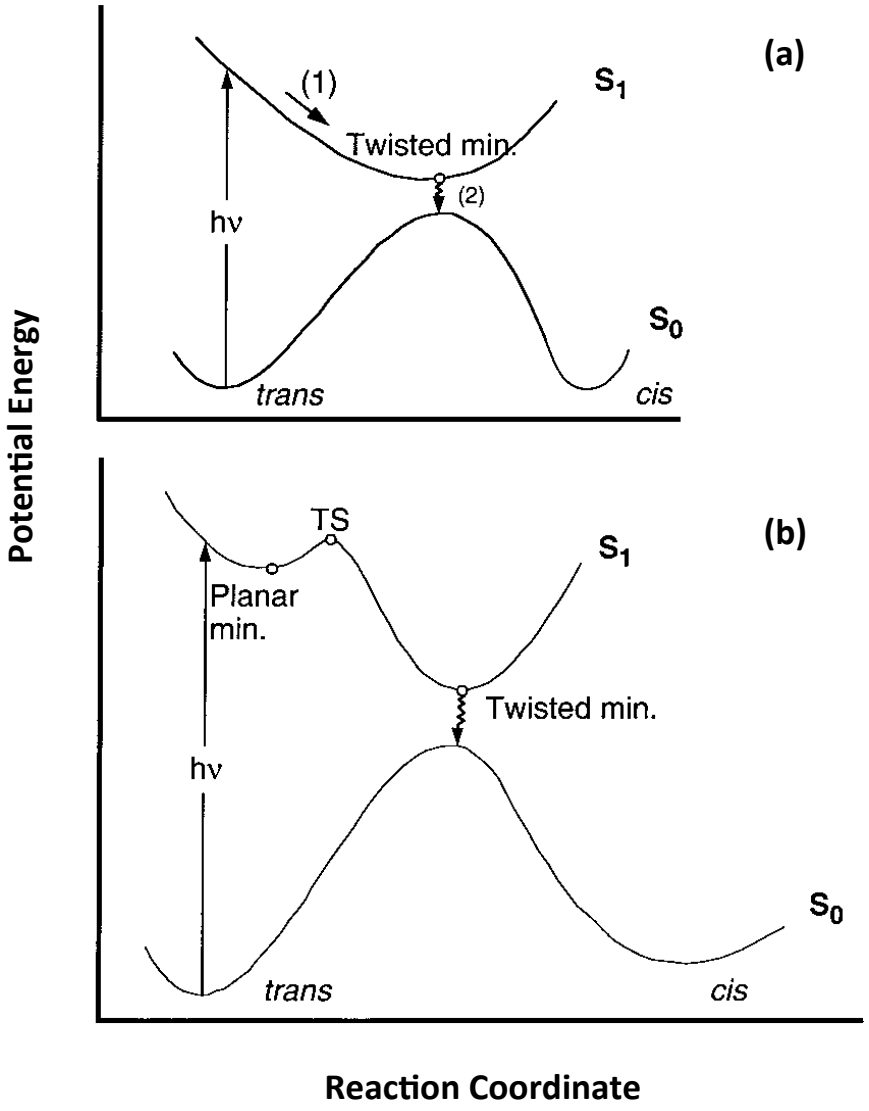

Figure 1.10. Potential-energy scheme for torsional dynamics of (a) a short cyanine, like 1144-C and (b) longer cyanines. Upon optical preparation of the S_1 state of short cyanines (a), torsional motion away from the Franck–Condon (FC) structure takes the system to the twisted minimum where radiationless decay can occur at the conical intersection (CI). For longer cyanines, optical preparation of the S_1 state involves displacements initially along bond-alternation coordinates to a planar minimum. The transition state (TS) marks the position along the reaction coordinate that divides the potential-energy curves between the planar region associated with the Franck–Condon (FC) structure and that along torsional coordinates leading to a twisted minimum-energy structure. (Used with permission from Olivucci *et al.*[1] Copyright 2000 American Chemical Society.)

The shape of the potential energy surface along the torsional coordinates of short cyanines resembles that of ethene. The photophysics of ethene is discussed in

detail in the review by Levine and Martinez.[55] Briefly, the CI is the region of the potential energy surfaces for the two ground state configurations (*cis* and *trans*) would intersect in the diabatic limit. Interaction between the surfaces of the two configurations results in a quantum-mechanical mixing, and a continuous ground and excited state surface that links the configurations is formed. The ground state is cosinusoidal, with minima for the two configurations and a barrier at the structure corresponding to a 90° torsion along the C=C bond axis. The excited state surface has a single minimum at the 90° torsion. This is similar to the Olivucci picture for short cyanines and PSBs (Figure 1.10a), where upon photoexcitation, the force in the Franck-Condon region of the S_1 state pushes the system barrierlessly toward the CI. At the CI the system non-radiatively transfers to the S_0 state surface where the system partitions to reform the initial ground state, or can form the photoisomer.[1,55] The dynamics for the longer cyanines and PSBs, then, are ethene-like after the transition state that divides the MEP along the stretching and torsional coordinates is passed (see Figure 1.10b). The barrier height controls whether isomerization is important in the photophysics, and this height can be controlled by many factors including local electrostatics, the molecular polarizablilty, the dipole moment, and charges in the vicinity.[55]

In addition, the dynamics of isomerization of the cyanines and PSBs are also profoundly affected by solvent friction. Hynes and coworkers[56] performed simulations of the isomerization of PSBs in water and acetonitrile solvent by adding a third normal coordinate corresponding to an interaction with the solvent bath. The main conclusion of this work was that friction from the solvent generally

accelerates the passage through the CI to the ground-state products and generally favors the photoisomerized product rather than the original configuration. In the solvent-free picture, the *cis* and *trans* ground-state products are formed with equal yield because the ground state surface is at a saddle point at the 90° torsion/CI geometry so that the excited state population is divided equally as it falls toward either minimum on the ground-state surface. It should be noted that the large preference for the photoproduct (13-*cis*-*trans*) observed by Mathies, Shank, and coworkers for retinal in rhodopsin[57] was assigned to conservation of momentum crossing the CI according to a Landau-Zener surface-hopping model, where the probability of hopping from one surface to the other was controlled by the velocity of the system prior to crossing the CI. An interesting (and counterintuitive) conclusion from the Hynes group study is that the presence of the solvent mode accelerates the formation of product by repelling the system after passage through the CI. This feature of the dynamics involves the formation of an ionic or intramolecular charge transfer (ICT) character at the CI.[56] As prototypically discussed in the case of ethene, but applicable to all polyenes,[55] as a C=C double bond is twisted, the energy of a charge-transfer state converges toward that of the neutral (valence) state. The formation of this twisted ICT state formally involves transfer of an electron across the bond; in the PSBs and cyanines this is promoted by the presence of the nitrogen at one end of the polyene. One might suggest, then, that the retention of vibrational coherence observed in the product state of retinal in rhodopsin[58] might have a solvent-dependent contribution arising from the interaction of the chromophore with the surrounding protein.

1.5 Dynamic Solvation

1.5.1 Dynamic Polar Solvation

A commonly used approach for determining the timescales for solvent response around a chromophore in solution is the method of dynamic solvation.[59-62] In polar solvation, optical excitation of a chromophore results in an instantaneous change in charge distribution that typically manifests as a permanent dipole moment that is significantly larger than that of the ground state. The reorientational movement of the solvent in response to the new charge distribution or dipole moment is knows as dynamic solvation. This reorientational movement of the solvent results in a dynamic Stokes shift; a time-dependent red-shift of the chromophore's emission spectrum. The solvent response can be described as the normalized response function,[59]

$$S_\nu(t) = \frac{\nu(t) - \nu(\infty)}{\nu(0) - \nu(\infty)} \tag{1.1}$$

where $\nu(t)$ is the mean frequency at emission time *t*. This normalized response function is measured in fluorescence Stokes shift (FSS) experiments. The observed response function, $S_\nu(t)$, measured in FSS experiments can be compared to the normalized time correlation function,

$$M(t) = \frac{\langle \Delta\omega(0)\Delta\omega(t) \rangle}{\langle \Delta\omega(0)^2 \rangle} \tag{1.1}$$

derived from molecular dynamic (MD) simulations.[63] This time correlation function, $M(t)$, provides a molecular description of the loss of memory over time of

the instantaneous transition frequency $\omega(0)$, , where $\Delta\omega(t)$ (defined as $\Delta\omega(t)=\omega-\omega(t)$) compares the time evolving energy gap, $\omega(t)$, to that of the ensemble average, ω. At high (room) temperatures, in the linear response regime, $M(t)$ is a very good approximation of the solvent response function $S_V(t)$.[62,64,65] This requirement is generally fulfilled in the case of a probe/solvent system because the optical excitation of the probe results in a small change in the probe's dipole moment and accordingly presents only a small perturbation to the motions and structure of the solvent.[66,67]

The instantaneous normal mode theory of liquids[59,68,69] developed by Stratt and co-workers provides some insight for the types of motion associated with the solvent response and their corresponding timescales. This theory, along with dynamic solvation experiments, lead to the current understanding of bulk solvent dynamics. Molecular dynamics simulations of liquids have revealed three regions of the solvation response: a fast inertial, or ballistic free rotor motion regime in the short-time limit (~100fs), an intermediate time regime in which oscillatory motions are observed, and a relatively long-time regime (> 500 fs) in which oscillatory motions are damped out, and random diffusive motions dominate the solvation response. According to the model, the ordering of these timescales reflect the onset of intermolecular forces, where initially the solvent responds without the impeding forces of the surrounding molecules. The subsequent coherent and incoherent motions during their respective time regimes are associated with intermolecular forces. From the MD trajectories of a solvent/solute system, the instantaneous normal mode theory predicts that the intermolecular frequencies dominating these

time regimes are predominately associated with hindered translational and hindered rotational (librational) movement of the solvent. This bimodal type of solvent response was later confirmed experimentally by Fleming and co-workers.[63,70]. An initial Gaussian-shaped solvation response, which accounted for about half of the total solvation response and occurred on the <100 fs timescale, was assigned as the inertial response. The subsequent exponential solvent response occurring on a slower timescale of <1 ps was assigned to the diffusive stage.

1.5.2 Nonpolar Solvation Dynamics

In polar dynamic solvation, chromophores with a change in dipole moment upon photoexcitation are sensitive to the reorientation of dipoles of the surrounding solvent as well as the diffusion of the solvent molecules. Chromophores with no significant change in dipole moment upon photoexcitation are relatively insensitive to dipole reorientation and are good probes for nonpolar solvation dynamics. Measured nonpolar solvation dynamics predominantly report the movements of the solvent molecules' center of mass relative to the probe and thus is a good measure of solvent viscosity.[71] In the nonpolar solvation picture, photoexcitation drives an instantaneous change in molecular size, and forces in the Franck–Condon region of the solvent-solute excited-state structure can be thought to cause a redistribution of the solvent to a red-shifted equilibrium structure (see Figure 1.11).

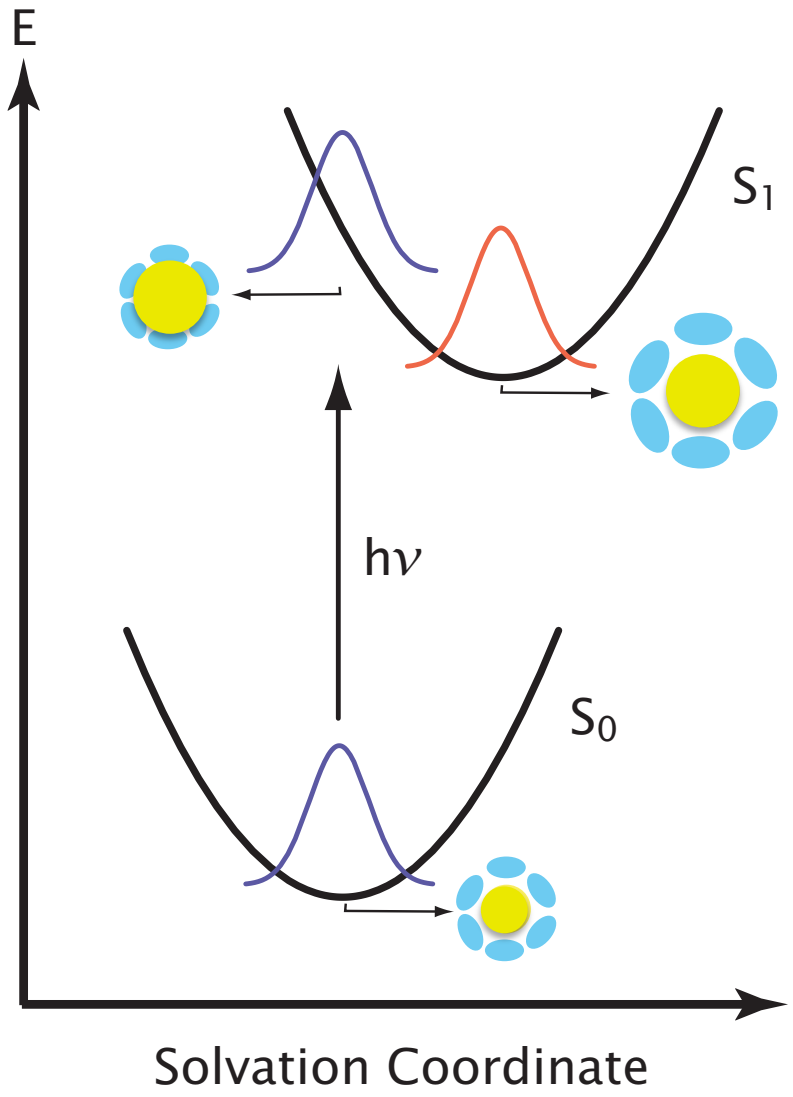

Figure 1.11. Schematic energy diagram depicting dynamic nonpolar solvation. Excitation drives a solvent-equilibrated chromophore (yellow circle) from the ground (S_0) state to the S_1 state causing an increase in molecular size to a non-equilibrated excited state. Forces in the Franck–Condon region of the S_1 state can be thought to reorganize the solvent around the chromophore excited state to a red-shifted S_1 equilibrium structure.

Similar to polar solvation, nonpolar solvation exhibits a bimodal response consisting of an ultrafast Gaussian, and subsequent exponential component. In solids, the fast nonpolar component arises from interactions with environmental phonons. This response in liquids is a high-temperature extrapolation of

phenomenon, so the term "phonon induced" is used for this fast, Gaussian component, where "inertial" is used in polar solvation.[71] The rate of this phonon-induced component is known to be relatively viscosity independent, where the slow component is directly proportional to solvent viscosity.[71] In this dissertation, we use cyanine 5 as a probe for nonpolar solvation in bulk water and in the hydration shell of Zn^{II}–substituted cytochrome *c* (ZnCytc).

CHAPTER 2

Nonpolar Solvation and Excited-State Torsional Dynamics of the Cyanine Dye Cy5 in Water

2.0 Summary

The nonpolar solvation response of bulk water and excited-and ground-state vibrational dynamics of the symmetric indolecyanine dye cyanine 5 (Cy5) were studied using multiple nonlinear optical techniques. Three-pulse photon echo peak-shift (3PEPS) experiments measured the nonpolar response of bulk water surrounding Cy5. This response consisted of a large amplitude, Gaussian phonon-induced component ($\tau = 21$ fs) and a relatively small, exponential diffusive component on the 900 fs timescale. Pump–probe measurements of the pure stimulated emission (SE) region of Cy5 in water, corresponding to the pure excited-state population, show strongly modulated vibrational coherence signals that exhibit unusually fast damping. Degenerate transient grating measurements in the photobleaching + stimulated emission (PB+SE) region show less strongly-modulated vibrational coherence signals with significantly longer damping times.

The unusually fast damping of this excited-state torsional wavepacket motion was attributed to coherent barrier crossing of a transition state toward a "twisted-minimum" conformation in accordance to the two-state two-mode picture presented by Olivucci.[1] In addition, population decays visible in the pump–probe and transient-grating signals are consistent with the timescales for diffusive nonpolar solvation as measured by 3PEPS spectroscopy. This suggests that there

are two timescales for twisting in this intermediate-length cyanine: coherent barrier crossing along torsional modes, and diffusive barrier crossing that appears to be affected by solvent viscosity.

2.1 Introduction

The structural characteristics of cyanines include a conjugated polymethine chain with amino end groups. Figure 2.1 shows some representative cyanines with varying polymethine chain links. Cyanine dyes have been widely employed as probes in microscopic imaging,[72-74] in single molecule fluorescence studies, [75] and even as sensitizers in dye-sensitized solar cells.[76,77] A distinctive aspect of the photophysics and photochemistry of cyanines is their tendency to photoisomerize, which helps explain some of their characteristics such as viscosity-dependent fluorescence yields[78-81] and single-molecule fluorescence blinking.[75] Short cyanines such as 1144-C have been exploited as model systems for the study of *trans–cis* photochemistry in polyenes.[82-88] This work presented in this dissertation provides a direct view of the nature of the transition-state motions and possible changes of spin state that occur in longer polyenes on the way to photoisomerization by characterizing the excited-state vibrational coherence and dynamic nonpolar solvation of the symmetrical, water-soluble tricarbocyanine dye, cyanine 5 (Cy5) (see Figure 2.1: structures). A comparison of the Franck–Condon (FC) and transition-state vibrational motions in Cy5 provide experimental support for the first time for the two-state two-mode pathway suggested by Olivucci and coworkers,[1] that longer polyenes initially populate a planar structure prior to activating torsional motions near the transition state.

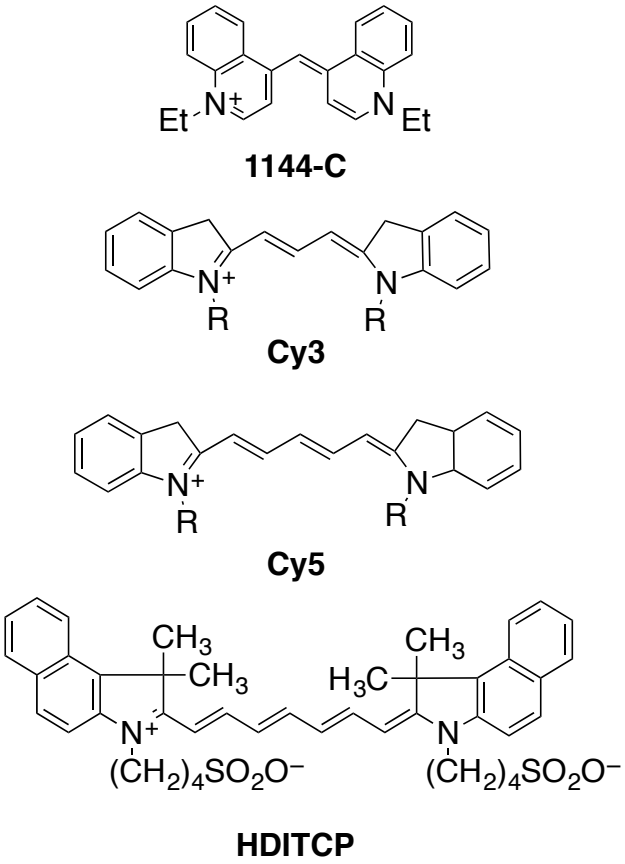

Figure 2.1. Structures of typical cyanine dyes with varying conjugation lengths.

The consensus view is that the S_1-state ($\pi \rightarrow \pi^*$) potential surface for conjugated polyenes such as Cy5 includes a conical intersection (CI) near its minimum, from which *trans–cis* isomerization and possibly singlet to triplet spin conversion[89-91] occurs (see Figure 2.2). In this picture, which has been widely tested in computational[92-94] and experimental[82-88] studies of cyanine photophysics, progress of the excited-state structure toward the CI is increasingly hindered by a barrier that divides the S_1 surface between the FC structure and the CI as the length of the conjugated polymethine chain increases.

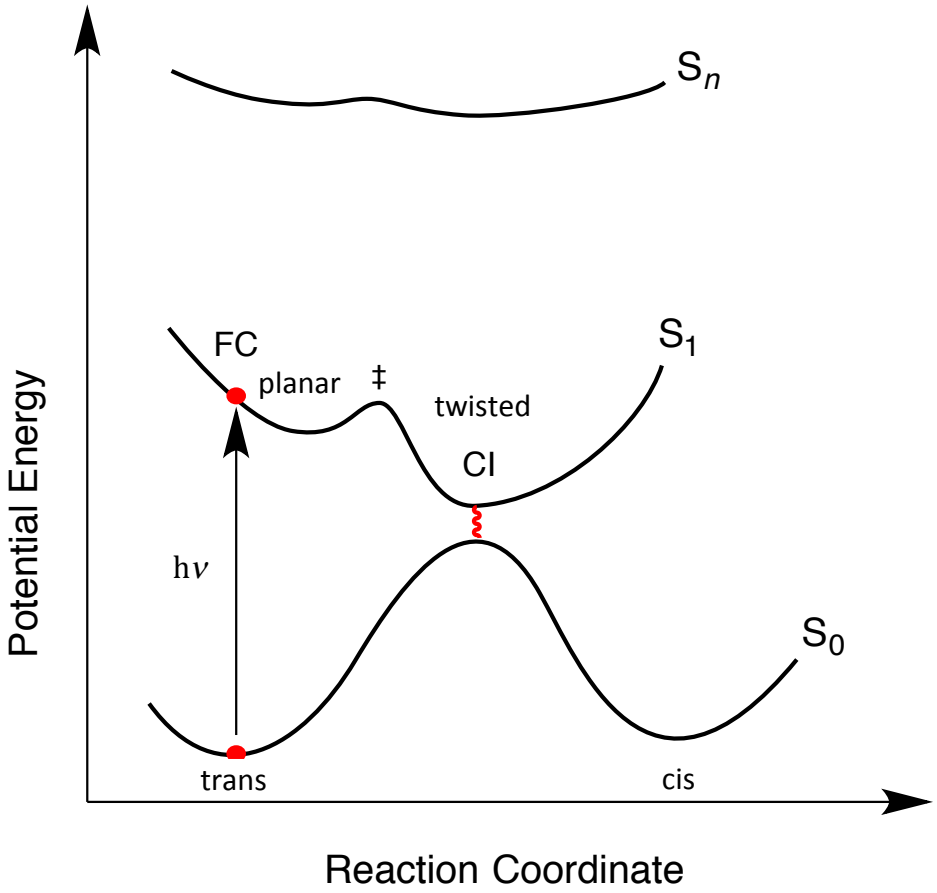

Figure 2.2. Schematic potential energy scheme for cyanine 5 after optical preparation of the S_1 state. A transition state (‡) marks the intersection between the planar minimum near the Franck–Condon (FC) geometry, and the torsional coordinates leading to a twisted minimum near the conical intersection (CI). After Olivucci *et al.*[1]

Upon photoexcitation, the shortest cyanines are thought to evolve along strongly coupled stretching modes and torsion motions on a barrierless or low barrier[87] trajectory toward a CI that subsequently populates the initial FC state or the *cis* product on an extremely short timescale (< 50 fs).[95-98] Considerable effort to affect the relative yields of the *cis* and *trans* isomers in cyanines have been applied in coherent control experiments[99,100] with the supporting theory.[101,102] The photophysics of longer cyanines, however, are not as well studied, but a key difference between the potential surfaces for the monomethine cyanines and longer

cyanines is that the torsions are uncoupled from the FC motions in longer polyenes.[1] For these longer polyenes, the Olivucci picture anticipates a barrier that separates the FC modes from torsions, and MD simulations actually suggest that the vibrationally displaced structure in the FC region undergoes several vibrations prior to redistributing energy to the torsions that subsequently take the polyene to the CI region on the potential energy surface. This two-state two-mode picture is used to account for the photochemistry of the retinal pigment in bacteriorhodopsin[103] and rhodopsin[57] which are thought to undergo ultrafast isomerization as the first step in vision.

Supposing the character of the FC and transition state active modes are different suggests a different action of the surrounding solvent in the two stages of dynamics. The FC-active motions are predominantly in-plane motions that might not exhibit strong solvent-viscosity effects[82,83,86,104-106] and should give rise to prompt red-shifting in transient spectra. In contrast, the transition state motions are out-of-plane in character, so they should be strongly limited by solvent viscosity, and thus the timescales of nonpolar solvation. In order to address these issues, we use Cy5 as a probe for nonpolar solvation. Cy5 is available commercially (GE Healthcare PA25001) with a ~10 Å tether terminated either with a N-hydroxysuccidimidyl (NHS) ester for linkage to amines, or a maleimide group for linkage to cysteine residues. This linker would enable tethering to a protein such that the dye molecule would reside within the hydration sphere of the molecule. The electronic structure of the Cy5 chromophore is comparable to that of the structurally related cyanine dyes IR125 and HDITCP, which have been discussed as nonpolar probes for

solvatochromism and nonpolar solvation dynamics by Jonas and co-workers.[107] Two resonance structures like the one shown in Figure 2.1, each with a formal positive charge on one of the indole nitrogen atoms at the end of the conjugated polymethine chain and a mirror image of the other, contribute equally to the average structure of Cy5. The π-electron density and charge are extensively delocalized over the full length of the conjugated region; the $\pi \rightarrow \pi^*$ transition results in a symmetrical change in electron density with respect to the mirror plane, so a negligible change in dipole moment occurs. The nonpolar assignment is supported by a computational study of related indocyanine dyes in comparison to the measured linear line-shapes.[105] Thus, the time-integrated shift to the red of the continuous-wave fluorescence spectrum with respect to the absorption spectrum arises in Cy5 primarily from a nonpolar mechanism; using the continuum viscoelastic theory advanced by Berg,[71] the shift is treated in terms of the change in solute size or shape that accompanies the optical excitation and the phonon-induced and structural responses of the surrounding solvent cavity.

2.2 Experimental

2.2.1 Sample Preparation. Cy5 solutions in water were prepared using the sulfonated amine monoreactive NHS ester of Cy5 (GE Healthcare, PA25001) at pH 7.0 in the 25 mM sodium phosphate buffer solution; the NHS ester hydrolyzes to yield a carboxylate at the end of the tether after prolonged exposure in aqueous solution as shown in Figure 2.3. For use in the femtosecond pump–probe experiments, solutions of Cy5 in water were prepared by diluting concentrated

solutions to obtain an absorbance of 0.3 for a path length of 1.0 mm at the center of the laser spectrum at 665 nm. The samples were held in the femtosecond pump–probe spectrometer at room temperature (23 °C) in a stirred fused-silica cuvette (1.0-mm path length). The sample's absorption spectrum was monitored for changes arising from photochemistry or permanent photobleaching.

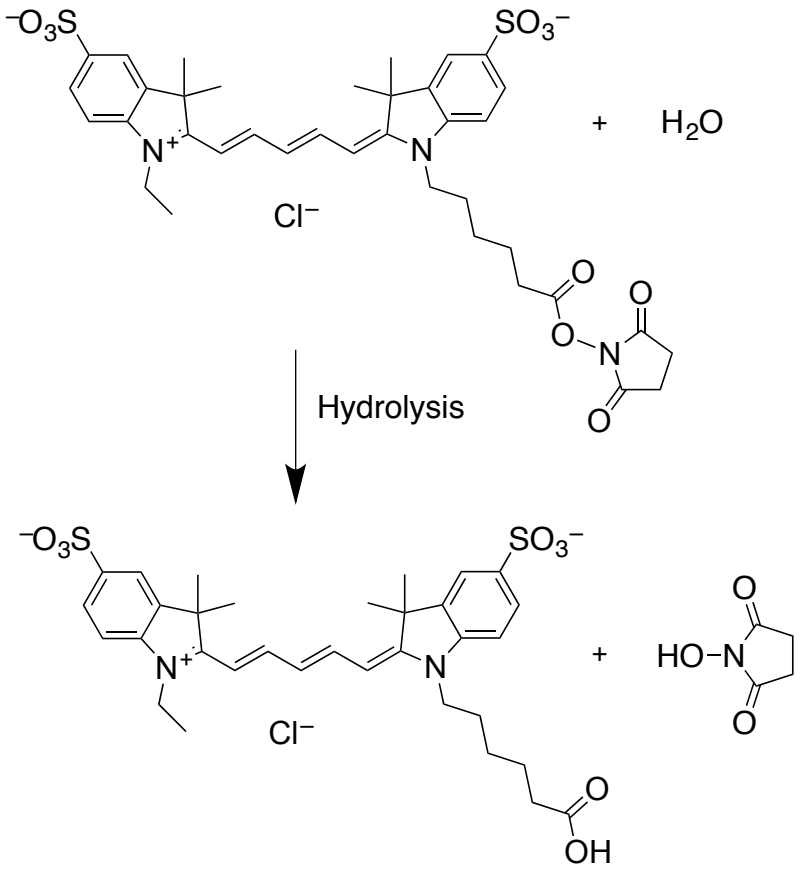

Figure 2.3. The hydrolysis reaction that occurs with the cyanine 5 N-hydroxysuccinimidyl ester in water.

2.2.2 Linear Spectroscopy. Absorption spectra were acquired with a Hitachi U-4001 spectrophotometer (2 nm bandpass). Fluorescence spectra were obtained using a home-built fluorescence spectrometer consisting of a Jobin-Yvon AH10 100 W tungsten-halogen light source, a Jobin-Yvon H10 excitation monochromator

(4 nm bandpass), an Acton Research SP-150 emission spectrograph (2 nm bandpass), and a Jobin-Yvon Symphony CCD detector. The spatially integrated power of the excitation beam, as estimated using a Coherent Fieldmaster power meter and associated silicon photodiode detector, was 11 μW at 522.9 nm. Fluorescence emission spectra were acquired as the average of twenty 60-second exposures of the CCD detector. The CCD detector employs a liquid nitrogen cooled, back-illuminated, 2000 × 800 pixel silicon detector chip (EEV corporation). A 300 groove/mm diffraction grating (500 nm blaze wavelength) was mounted in the emission spectrograph, resulting in a 270 nm spectral range imaged over 2000 vertically binned channels on the CCD detector chip. As presented as a function of wavenumber, the fluorescence intensities are multiplied by the square of the wavelength in order to compensate for the fixed (in wavelength units) spectral bandpass of the emission spectrograph. The absorption instrument is controlled by Hitachi UV Solutions. The fluorescence instrument is controlled by LabVIEW (National Instruments) programs.

2.2.3 Femtosecond Pump–Continuum-probe Spectroscopy. Femtosecond pump–continuum-probe experiments were conducted with pump pulses from an optical parametric amplifier (OPA, Coherent OPA 9450), which was driven by a 250-kHz regeneratively amplified Ti:sapphire laser (Coherent RegA 9050 amplifier and Coherent Mira-Seed oscillator). The oscillator and amplifier were continuously pumped by Coherent Verdi V5 and V10 Nd:YVO_4 lasers. Figure 2.4 shows a schematic representation of the transient absorption instrument. The signal-beam output of the OPA was compensated for group-delay dispersion by an SF10

Brewster prism pair and variably delayed by a retroreflector on an optical delay line driven by a Melles-Griot Nanomover actuator. The pump-pulse duration was measured to be 45 fs at 665 nm by a zero-background autocorrelator using a 100-μm KDP crystal; the spectrum was determined to be 18-nm in width (FWHM) centered at 665 nm by an Ocean Optics U2000 spectrometer (0.5-nm bandpass).

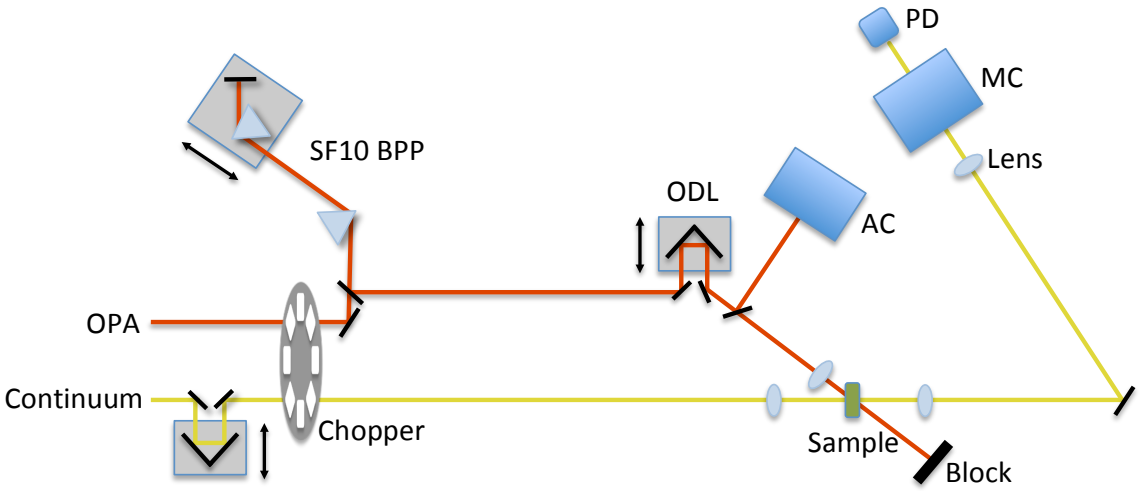

Figure 2.4. Schematic diagram for the pump–probe transient absorption spectrometer used in the pump–continuum-probe experiments. Optical parametric amplifier (OPA) beam, SF10 Brewster prism-pair (BPP), optical delay line (ODL), autocorrelator (AC), monochrometer (MC), photodiode (PD).

Probe pulses were obtained from a single-filament, chirp-compensated femtosecond continuum, which was generated as the seed pulses for the first gain pass in the OPA. The chirp on the probe beam was compensated over the 500–780-nm range using a pump-delay program controlled by a third-order polynomial with respect to the probe wavelength shown in Figure 2.5. The chirp program was determined using optically heterodyne-detected optical Kerr-effect measurements of the probe arrival delay at the sample position as a function of probe wavelength.

The rise time (10% to 90%) for the pump–probe signal was typically 75 fs for a 4-nm probe bandpass.

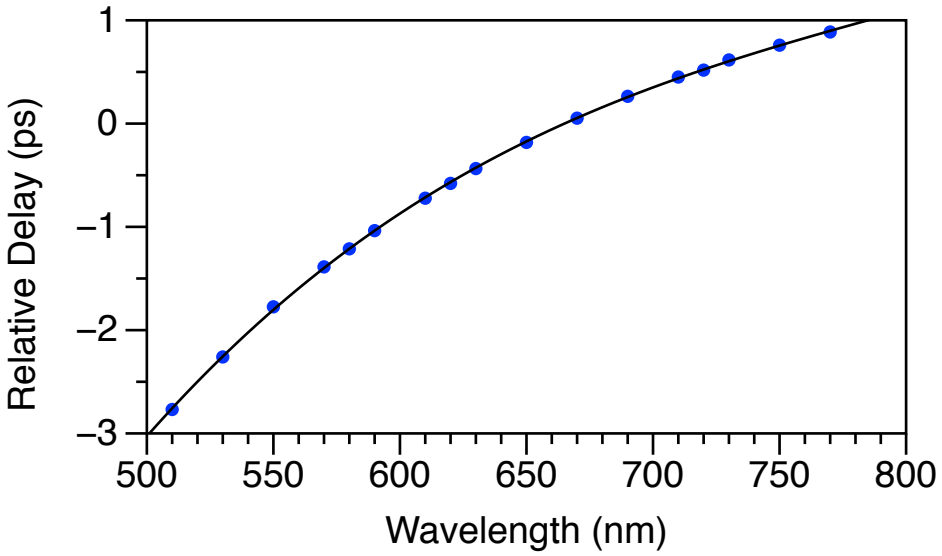

Figure 2.5. Time-dependent wavelength (chirp) of the continuum pulse relative to the pump wavelength (665 nm) as determined by optical Kerr effect (OKE) experiments of carbon disulfide at the sample position. The OKE data (blue dots) were fit to a cubic polynomial to correct for the relative timing of the continuum at different wavelengths in the pump–probe spectra.

For pump–probe measurements, the planes of linear polarization of the pump and probe beams were set to the magic angle (54.7°) using calcite polarizers and $\lambda/2$–retarding wave plates. The probe intensity was detected by a Thorlabs PDA-55 amplified photodiode after it passed through the sample and a double-subtractive monochromator (Spectral Products CM112) with a 4-nm bandpass. The pump–probe signal was obtained as the normalized pump-induced change in probe transmission ($\Delta T/T$) signal using a SRS SR-830 lock-in amplifier referenced to the sum frequency of the pump and probe modulation frequencies (4.1 kHz for ΔT, Palo

Alto Research model 300 chopper) and a SRS SR-850 lock-in amplifier referenced to the probe modulation frequency (2.5 kHz, for T).

2.2.4 Photon Echo Spectroscopy. Degenerate transient-grating and three-pulse photon echo peak shift (3PEPS) measurements were acquired with the same 665 nm pump pulses described above with parallel (0° relative) polarization. The passively phase-stabilized photon echo spectrometer was constructed following aspects of the designs discussed by Moran and Scherer[108] and Brixner *et al.*[109] Figure 2.6 shows a schematic representation of the instrumental setup.

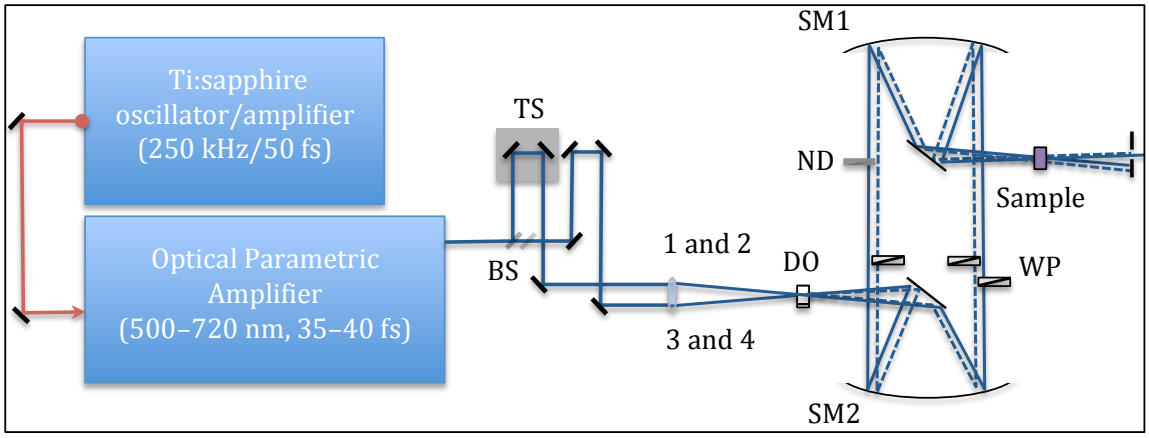

Figure 2.6. Schematic representation of the diffractive optic-based photon-echo spectrometer for use in transient-grating (TG) and three-pulse photon echo peak-shift (3PEPS) spectroscopy. For homodyne experiments, the local oscillator (LO) is blocked prior to the sample. Beam splitter (BS), translation stage (TS), diffractive optic (DO), spherical mirror (SM), neutral density (ND) filter, wedged prism (WP) pair, charge-coupled device (CCD) camera.

After compression via an SF10 Brewster prism-pair pulse compressor, a beam splitter splits the pulses into identical replicas, where the pump pulse can be variably delayed to control the population time T before entering the diffractive optic experiment. The two parallel beams are focused onto a transmissive

diffractive optic (DO; 400 gr/mm) and a mask allows the ± 1 order beams to be reflected off a 45° oriented mirror onto a 20 cm focal-length spherical mirror that collimates the four beams in the BOXCARS geometry. A pair of 1° wedged optics is introduced to each of the two pump pulses and one of the probe pulses, while the remaining probe pulse is attenuated by a factor of $10^{3.5}$ using a neutral density filter to act as the local oscillator (LO). Translation of one wedge relative to the other adds variable delay (coherence delay, τ) at a rate of about 60 fs per mm of wedge movement without disturbing the alignment (see Figure 2.7). This coupled with the highly precise Melles Griot Nanomover (<50 nm step size with 100 nm repeatability) translates to a pulse timing precision of about 6 as. An identical second spherical mirror and 45° oriented mirror image the four beams onto the sample position where the third order signals are generated. A mask and two tight aperture irises around the signal beam ensure only the homodyne signal (LO is blocked prior to sample) is detected by the detector.

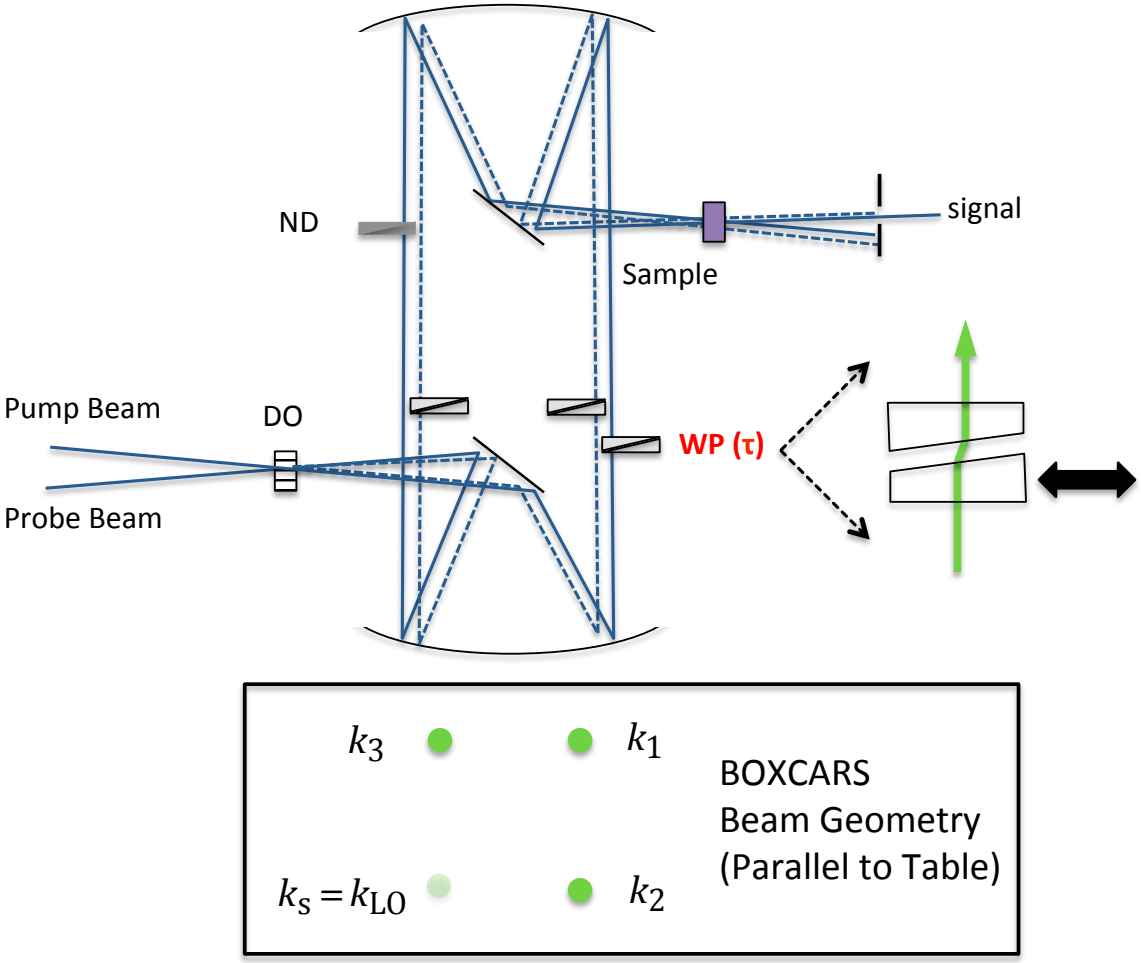

Figure 2.7. Detailed schematic of the photon-echo interferometer. The diffractive optic (DO) splits the pump and probe beams vertically, and the ±1 diffraction orders are utilized to form the BOXCARS geometry. A turning mirror and a spherical mirror collimate these beams along the table . The pulse trains travel along the **k** wave-vectors and are imaged onto the sample position using a second spherical mirror oriented at 0° and a turning mirror. Paris of 1° wedged prisms (WP) are inserted in beams 1–3 antiparallel as to minimally disturb the initial alignment at the sample position. Parallel translation of these wedged prisms add extremely precise variable delay without changing the alignment. The fourth beam is attenuated by a factor of $10^{3.5}$ using a neutral density (ND) filter to act as a local oscillator. Photon echo signals (along $\mathbf{k}_S$) are generated in the direction of $\mathbf{k}_{LO}$ and can interfere in a spectrometer to create heterodyned spectra.

For the 3PEPS experiment, the coherence delay was scanned from negative to positive values of τ while maintaining a fixed population time T between the temporal second and third pulse. The time integrated echo intensity was measured

in the $\mathbf{k}_s = -\mathbf{k}_1 + \mathbf{k}_2 + \mathbf{k}_3$ direction and is the sum of the photobleaching (PB), stimulated emission (SE) and excited-state absorption (ESA) signals corresponding to the Feynman pathways shown in Figure 2.8. The signals were detected using a silicon photodiode and lock-in amplifier, using sum-frequency detection of the pump (beams 1 and 2) and probe(beam 3). The transient-grating signal was detected similarly, but with the coherence time set to zero and scanning the population time *T*. These homodyne measurements were made at room temperature in a 1 mm stirred cuvette with an optical density of ~0.3 at the laser wavelength of 665 nm.

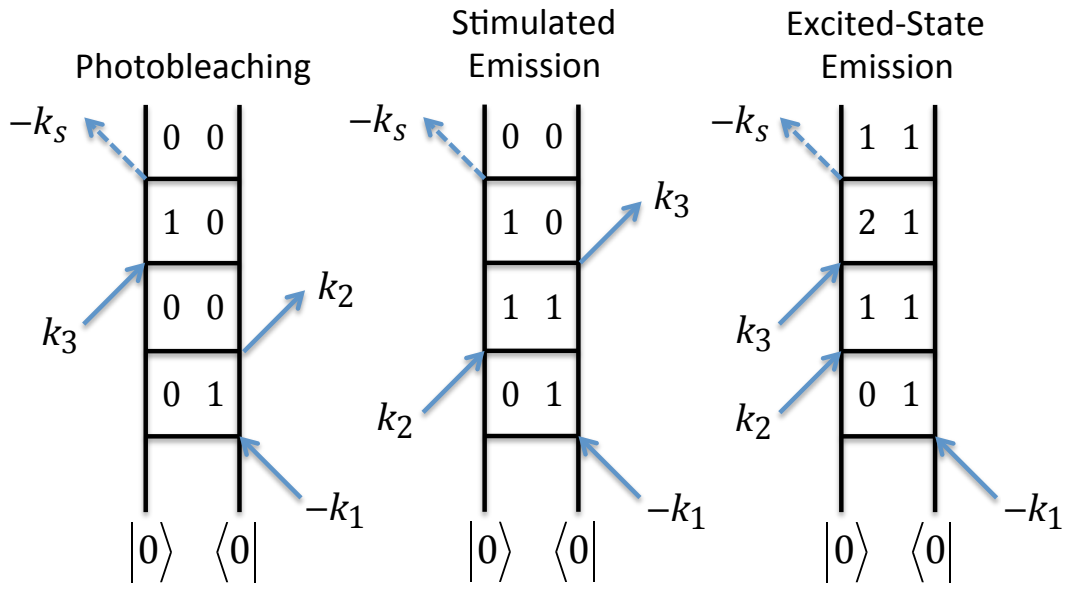

Figure 2.8. Double-sided Feynman diagrams corresponding to the photobleaching, stimulated emission, and excited-state absorption rephasing signals detected in the $\mathbf{k}_s = -\mathbf{k}_1 + \mathbf{k}_2 + \mathbf{k}_3$ phase-matching direction.

2.2.5 Computational Chemistry. The optimized structure for the Cy5 chromophore was obtained using Gaussian 03[110] using the B3LYP density functional and the 6-31G(d) level of theory. The length of the flexible tether between

the tagged lysine residue's α carbon and the N atom in the indole moiety at the other end of the tether was estimated with structures optimized using the UFF molecular mechanics force field.

2.3 Results

2.3.1 Linear Spectra. Figure 2.9 shows the continuous-wave absorption (blue) and fluorescence (red) spectra of Cy5 in water superimposed with the laser excitation spectrum (solid black). The excitation spectrum was chosen to hit low on the vibronic manifold (near the 0–0 vibronic transition) to minimize any contributions from vibrational relaxation. The spectra can be modeled by a sum of vibronically displaced ($\sim$1200 cm^{-1}) lognormal lineshapes with a full width at half-maximum (FWHM) of $\sim$780 cm^{-1}. The dotted black line in Figure 2.9 shows the mirror reflection around the 0–0 wavenumber. The increased florescence intensity to the red suggests structural displacement of the emitting state, possibly along torsional coordinates.

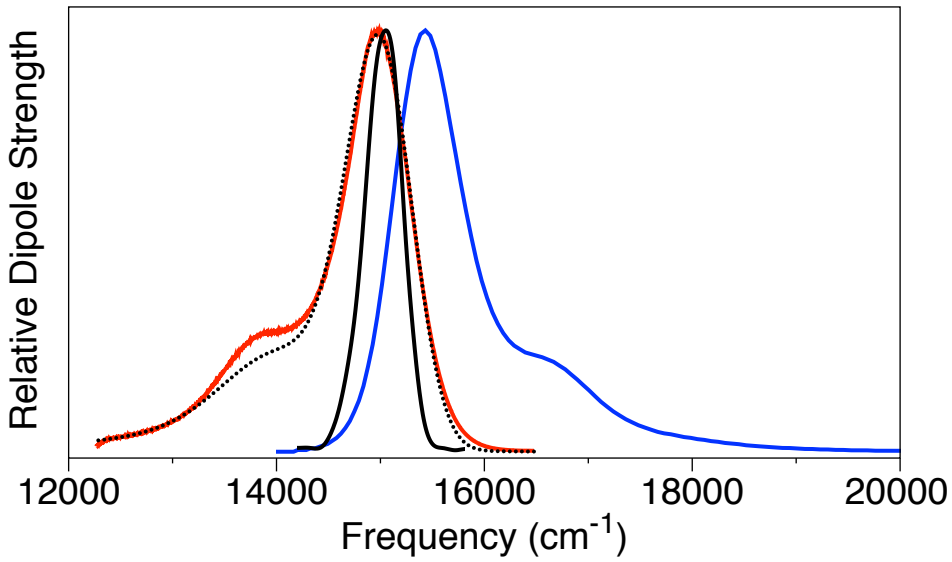

Figure 2.9. Room-temperature absorption (blue) and fluorescence (red) spectra of Cyanine 5 in water. Superimposed is the output spectrum of the 40 fs OPA signal beam (665-nm center wavelength, solid black line), as tuned for the pump–probe, transient-grating, and three-pulse photon echo peak-shift (3PEPS) experiments. The black dotted line corresponds to a mirror reflection of the absorption spectrum around the 0–0 vibronic wavenumber.

2.3.2 Pump–Continuum probe spectroscopy. Time resolved pump–probe spectra shown in Figure 2.10 show contributions from excited-state motion and nonpolar solvation. The PB panel shows a photobleaching spectrum, estimated from the product of the laser spectrum and ground state absorption spectrum. PB and SE signals are positively signed reflecting an increase in transmittance, and ESA signals are negatively signed reflecting a decrease in transmittance. The early-time spectra show PB+SE character well outside of the hole-burning PB region (top panel Figure 2.10), suggesting the homogeneous line width spans the absorption spectrum. The earliest-time spectrum (Figure 2.10, –20 fs) shows a relatively mirror-symmetric signal around the 0–0 vibronic position corresponding to the sum of the photobleaching and stimulated emission (absorption and emission) spectra.

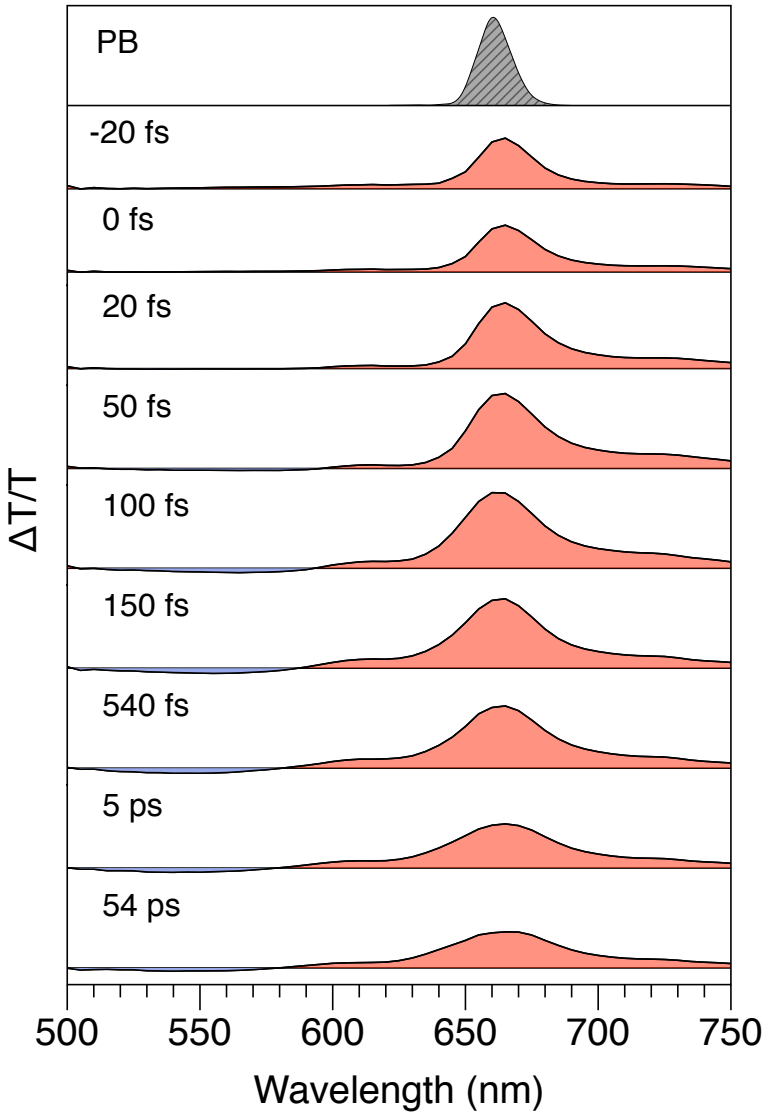

Figure 2.10. Time-resolved pump–continuum-probe spectra from cyanine 5 (Cy5) in water at selected pump–probe delay times *T*. The top panel (PB) shows the instantaneous photobleaching spectrum, which is estimated as the product of the laser spectrum and the absorption spectrum of Cy5 in water (see Figure 2.9).

By 0 fs the blue shoulder is decreasing due to the onset of an ESA signal which builds and blue-shifts. This evolution of the ESA feature is mostly complete by 500 fs. During this same time period, the red shoulder of the main peak grows in to maximum at about 50 fs owing to photobleaching of the ground state and red-shifting SE due to solvation. This blue shifting ESA and red-shifting SE during this

time period is also consistent with excited-state twisting, similar to what Mathies and Shank *et al*. observed during the photoisomerization of rhodopsin[111] and bacteriorhodopsin.[103] After about 500 fs, most of the dynamic character of the spectra is complete, and the spectra decay according to repopulation of the ground state.

The 720 nm transient in Figure 2.11a shows the time evolution of the pure SE region, which is fully resolved from the PB (absorption) spectrum. The transient is modeled by a sum of exponentials convoluted with an instrument response function (Figure 2.11a, solid line). The signal shows an instrument-response limited rise, reporting exclusively stimulated emission from the excited state, followed by a multiexponential decay with timescales of 1.1 ps and 637 ps. Rapidly damped oscillations arising from vibrational coherence are clearly visible on the pump–probe transient.

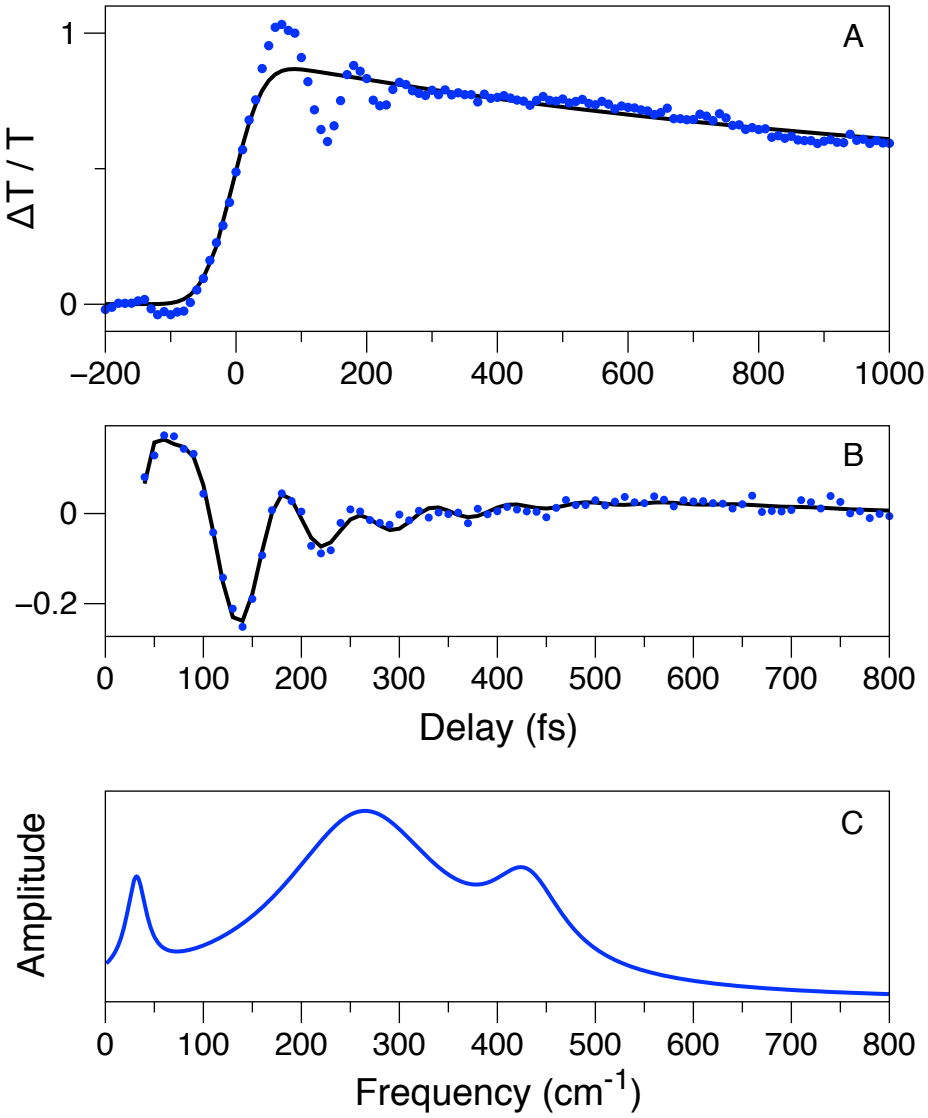

Figure 2.11. 665-nm-pump–720-nm-probe transient of Cyanine 5 in water (blue dots) modeled with an iterative reconvolution function (black line) consisting to two decay components (τ = 1.1 and 637 ps). The residuals (signal – model, blue dots), (b), are fit with a linear prediction–singular value decomposition (LPSVD) routine (black line in (b)). The power spectrum of the model in (b) is shown in (c). The LPSVD data is shown in Table 2.1.

Figure 2.11b shows the oscillatory components of the residuals (signal - model) from Figure 2.11a modeled with a linear prediction–singular value decomposition (LPSVD) method[112] (Figure 2.11b, solid line). The LPSVD model shows three

frequency components (Figure 2.11c) at 32, 260 and 430 cm^{-1} with respective normalized amplitudes of 0.04, 0.8 and 0.16 (Table 2.1).

Table 2.1: Damped cosinusoids and exponentials determined by LPSVD analysis of the pump–probe transient of cyanine-5 in water

Amplitude	Damping Time (fs)	Phase (°)	Frequency (cm^{-1})
0.04	430	149	32
0.80	50	161	260
0.16	120	238	430

2.3.3 Transient-grating Signals. The transient-grating signal probes a region of the Cy5 spectrum containing both PB and SE components and the generated signal contains dynamical information on the ground and excited states. The signal is modeled similar to the pump–probe transients. The transient-grating signal in Figure 2.12a shows an instrument-response limited rise in PB + SE followed by decays on the 21 and 900 fs timescales. The oscillatory component of the residuals with a LPSVD model is shown in Figure 2.12b. There are three main oscillatory components of 40, 120 and 255 cm^{-1}, and their associated weights and amplitudes are shown in Table 2.2.

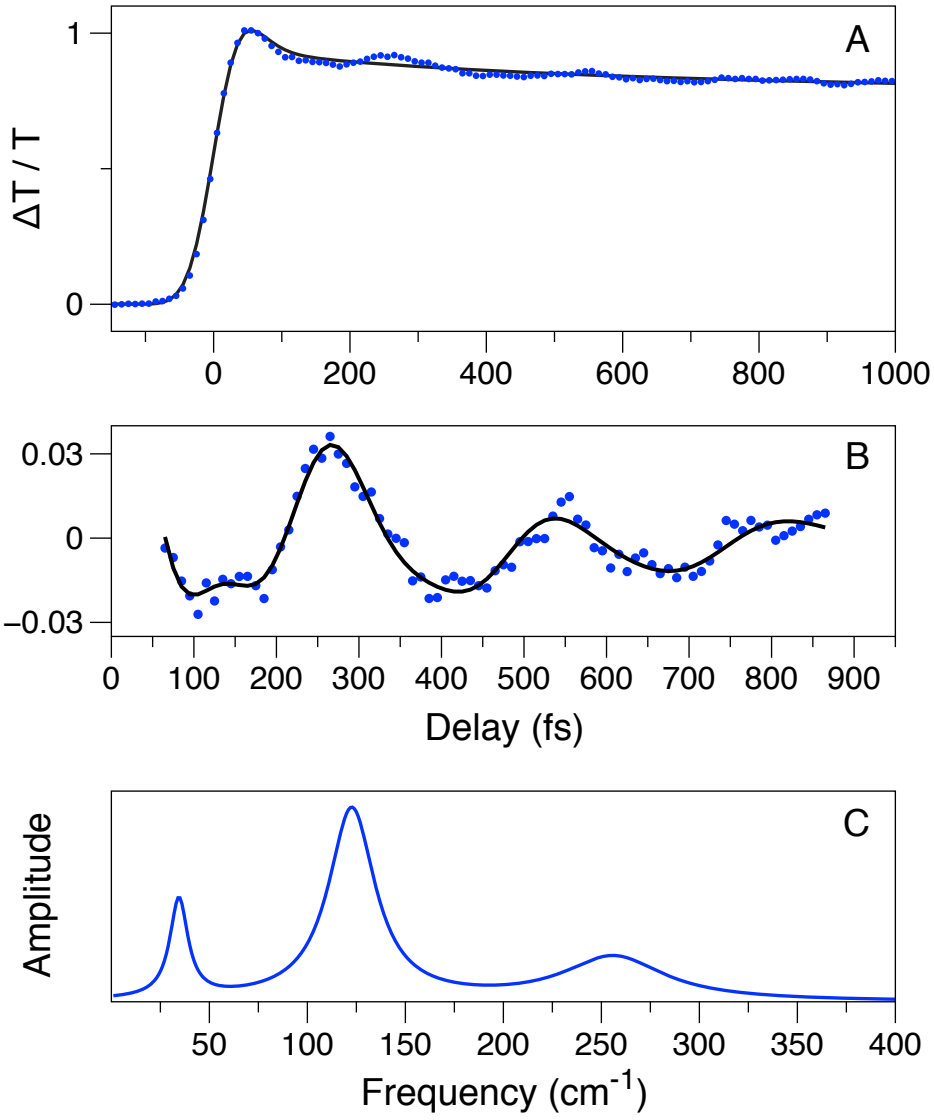

Figure 2.12. 665-nm degenerate transient-grating signal of Cyanine 5 in water (blue dots) modeled with an iterative reconvolution function (black line) consisting to two decay components (τ = 21 and 900 fs). The residuals (signal – model, blue dots), (b), are fit with an LPSVD routine (black line in (b)). The power spectrum of the model in (b) is shown in (c). The LPSVD data is shown in Table 2.2.

Table 2.2: Damped cosinusoids and exponentials determined by LPSVD analysis of the transient-grating signals of cyanine-5 in water.

Amplitude	Damping Time (fs)	Phase (°)	Frequency (cm^{-1})
0.14	1040	–47	40
0.54	395	–6	120
0.32	160	–18	255

2.3.4 Three-pulse Photon Echo Peak-shift Signals. The 3PEPS experiment is a population-free, indirect measure of the memory function $M(t)$,[113] which measures the time-evolving rephasing ability of a probe molecule. In the case of solvation, the memory function corresponds to a solvent time-correlation function which measures how well the energy of the time evolving state of a probe molecule remains correlated with an initial state under the influence of the surrounding solvent. For nonpolar solvation there is a negligible change in the transition dipole moment of the probe molecule upon photoexcitation, so scrambling of the initial state's energy occurs as solvent moves with respect to the probe. Unlike polar solvation, a nonpolar solvation probe is relatively insensitive to the orientation of the solvent dipole. The solvation response to a nonpolar probe is, therefore, a good measurement of solvent viscosity in keeping with the viscoelastic continuum theory.[71] The 3PEPS traces at each measured population time T were fit to a Gaussian and their peak-shifts relative to $\tau = 0$ are plotted in Figure 2.13. The ultrafast data is modeled as a sum of a Gaussian and an exponential by

$$M(t) = A_1 e^{-(t/\tau_1)^2} + A_2 e^{-(t/\tau_2)} + A_0 \qquad (2.1)$$

where t is the population time, τ_n is an exponential timescale, and A_n is the component amplitude. The fit parameters are shown in Table 2.3. The ultrafast 21 fs Gaussian component was followed by an 890 fs exponential decay.

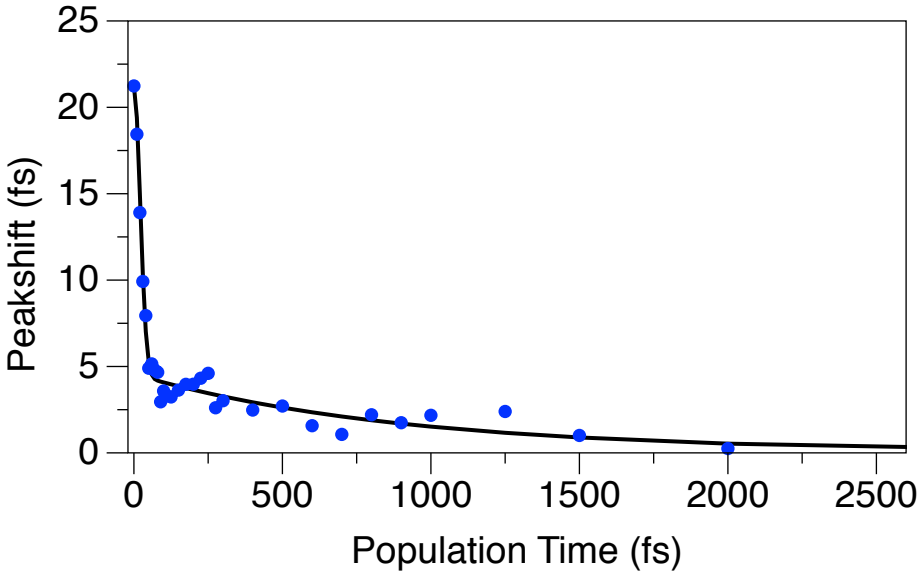

Figure 2.13. Three-pulse photon echo peak-shift (3PEPS) data for cyanine 5 in water. The data are fit to Equation 2.1 (black line) and the parameters are shown in Table 2.3.

Table 2.3: Model parameters of the 3PEPS data from cyanine 5 in water fit to Equation 2.1.

A_1	τ_1	A_2	τ_2	A_0
0.78	21 fs	0.22	890 fs	0 fs

2.4 Discussion

The absorption and emission spectra of the Cy5 NHS ester (Figure 2.9, blue and red lines) show a departure from mirror symmetry, where the main emission lineshape is 25 cm^{-1} wider, and the fluorescence at lower energies is more intense

than the mirrored absorption spectrum (Figure 2.9, dotted black line). This red-shifting of the emission likely arises from barrier-crossing as a population of Cy5 isomerizes, but this is not nearly as quantitative as the related shorter cyanine, 1144-C.[95,96,114] This is consistent with the two-state two-mode theory,[1] where the barrier for isomerization is lower for shorter cyanines as shown in Figure 2.2.

The 3PEPS data in Figure 2.13 show two main components for nonpolar solvation dynamics in water: a large amplitude, 21 fs Gaussian "phonon induced" component, and a smaller amplitude, 890 fs exponential diffusive component (Table 2.3). Similar to what was shown by Joo *et al.*,[64] the transient-grating signals report similar dynamics (20 and 900 fs decays) with similar amplitudes, where the transient-grating solvation signal lies on top of a population signal.

The very early-time pump–probe transient absorption spectra exhibit intensity outside of the hole-burned PB region (see Figure 2.10, 20 fs) with the vibronic structure conserved, suggesting that Cy5 is relatively free of inhomogeneous broadening due to a conformational distribution in the ground state. As the population time increases, the stimulated emission to the red of the main PB + SE peak rises according to the instrument response function, while an ESA feature to the blue begins to build, cancelling intensity in the blue side of the initial PB + SE region. By 50 fs a net ESA feature is apparent and the ESA intensity begins to build and shift to the blue. This blue-shifting of the ESA feature is evidenced by the blue-shifting of the zero-intensity point created by the sum PB + SE – ESA in the ultrafast time regime ($t < 5$ ps); if the ESA were merely building in intensity or shifting to the red relative to the PB + SE, this zero intensity point would shift to the red. The blue-

shifting of the ESA in this time-region is consistent with twisting of a polyene similar to that observed in the visual pigments bacteriorhodopsin[103] and rhodopsin.[57,111]

Pump–probe transient absorption data was taken at 720 nm to observe dynamics of the SE in region that are completely resolved from PB contributions. Figure 2.11a shows the early-time transient data modeled by a sum of exponentials convoluted with an instrument response function. The simplest model includes two exponential decays with timescales of 1.1 and 637 ps. The data is also modeled well with an additional ultrafast decay component (τ = 20 fs); this model would be attractive because it would show population loss on the timescale of phonon-induced nonpolar solvation, and would also be on the order of the wavepacket damping timescales, but because of the rapid signal oscillations due to vibrational coherence in this timescale, the existence of this component cannot be known with certainty. The transient absorption data shows an instrument-response limited rise followed by a multi-exponential decay. These dynamics appear to be dominated by contributions from excited-state conformational dynamics rather than those of nonpolar solvation due to a lack of additional rise components that would otherwise be apparent from red-shifting of the SE if nonpolar solvation contributions were dominant over this timescale. In addition, clear wavepacket motion is observed in the transient data. Figure 2.11b shows the residuals for Figure 2.11a (data – model) modeled using an LPSVD routine. The power spectrum of this model (Figure 2.11c) reveals three frequency components (see Table 2.1). The 260 and 430 cm^{-1} components are damped on extremely fast timescales (50 and 120 fs respectively). Due to the constant relative amplitudes of the 720 nm region compared to the main

PB + SE peak, the decay of the signal appears to be due to a loss of population rather than decay due to peak-shifting. In this light, the ultrafast damping of the vibrational coherence is likely to be due to coherent barrier crossing over the transition state to the CI in the excited state (Figure 2.2). Nonradiative decay via the CI can reform the ground-state *cis* isomer or the *trans* photoproduct. The subsequent decay of the pump–probe signal on the 1.1 ps is on a very similar timescale to the diffusive solvation component in the 3PEPS measurements and could correspond to incoherent barrier-crossing to the CI in the diffusive regime. If this two-timescale picture is valid, then this strongly suggests solvation control for the transition-state barrier crossing.

The integrated transient-grating experiment is a one color experiment, and due to the position of the laser emission spectrum relative to the absorption and emission spectra of Cy5 (Figure 2.9), the transient-grating data (Figure 2.11) show dynamics on the ground and excited states. The transient-grating data exhibit a net decay arising primarily from the solvation response and show the same timescales for nonpolar solvation as the 3PEPS data, but with a population offset. Wavepacket motion is readily observed in the transient-grating signal, arising mainly from three frequency components, similar to the pump–probe data. Both the pump–probe and transient-grating data show wavepacket motion with frequencies around 35 and 250 cm^{-1} (see Tables 2.1 and 2.2), but the damping times are significantly longer in the transient-grating signals. A comparison of the damping times from the transient-grating and pump–probe SE-region wavepacket motion lends support to picture of coherent barrier crossing along torsional modes in the excited state; the

transient-grating experiment is much more sensitive to the ground-state dynamics and the damping times in the transient-grating signal are significantly longer than the pure SE (excited-state) region measured by the 720 nm pump–probe transient.

In contrast to the shorter conjugated cyanine dye 1144-C which is thought to experience relatively high yields for photoisomerization,[96] Cy5 appears to have a much lower yield where a fraction of isomerization occurs essentially on the nonpolar solvation timescales. Population loss and ultrafast damping of excited-state coherent wavepacket motion evidenced by the 720 nm probe transient absorption measurement suggest coherent barrier crossing aided by the momentum of the wavepacket as it departs from the Franck–Condon excited state. Subsequent damping of these motions due to solvent viscosity appear to impede this isomerization, where subsequent population transfer occur on much longer timescales (640 ps), competing with the fluorescence lifetime (~1 ns[115]). It appears in these longer conjugated cyanine molecules the barrier heights for isomerization are significantly higher than short cyanine molecules and appear to be controlled, at least in part, by the ability of the solvent to accommodate this torsion motion to the CI.

CHAPTER 3

Nonpolar Solvation and Excited-State Torsional Dynamics of Cy5 in the Hydration Shell of Zn^{II}–Substituted Cytochrome *c*

3.0 Summary

Nonpolar dynamics within the hydration shell of Zn^{II}-substituted cytochrome *c* (ZnCytc) were measured using cyanine 5 (Cy5) utilizing femtosecond pump–probe and three-pulse photon echo peak-shift (3PEPS) spectroscopies. The commercially available Cy5–N-hydroxysuccinimidyl (NHS) ester allows linkage of Cy5 to the surface of ZnCytc at a distance of about 10 Å. The nonpolar solvation dynamics in the hydration layer showed a similar fast, Gaussian phonon-induced component to dynamics in bulk water, but with a significantly smaller amplitude. This is consistent with dynamics in more viscous solutions. Interestingly, the hydration shell dynamics show a faster exponential component than bulk water, which decay to a linear offset. The fast exponential component in the hydration layer is interpreted as lengthened phonon-induced component, and the offset to a diffusive component that decays on a timescale much longer than the experimental window ($\gg$ 2.5 ps).

The vibrational coherence signatures in the pump–probe signals of the pure stimulated emission (SE) region of Cy5 in the hydration layer of ZnCytc (Cy5–ZnCytc) exhibit significantly lower torsional mode frequencies compared to in bulk water and this is attributed to an increase in viscosity. The significantly increased damping rates of torsional motion in the hydration layer compared to bulk water

can be attributed to increased viscosity, a decreased barrier height to torsional deactivation in accordance with Olivucci's two state two mode theory,[1] or a combination of the two. It was concluded that the hydration shell is likely more viscous in character, but is also likely different in structure, perhaps consisting of hydrogen-bonded chains of waters induced by surface charges.

3.1 Introduction

The water at the surface of the protein is commonly referred to as the hydration shell, and is known to have significantly different properties[116] and dynamics than water in the bulk.[117-119] The hydration-shell water is thought to account for a large proportion of the thermodynamic stability of a folded protein,[120] where the hydrophobic effect segregates nonpolar groups to the interior of the protein, and polar and charged groups are exposed at the surface. Proteins in their native states are known to undergo a wide range of motions on very short timescales,[121,122] and these protein motions are thought to be intimately related to the dynamics of the hydration shell.[119] Observations of "proteinquakes" upon photodissociation of carbon monoxide from myoglobin led Ansari and co-workers to propose that long-range, slow protein motions were slaved in large part to the fast dynamics of the surrounding solvent.[123] Given the above, it is clear that the water directly surrounding the protein has biological significance, yet a precise understanding of the organization, interactions, and dynamics of this water is not well understood.

Water in the hydration shell of a protein is known to have slower dynamics than bulk water The thickness of the hydration shell can be inferred from a comparison of the hydrodynamic radius with the radius of gyration calculated directly from an X-ray diffraction or NMR structure[124]; the dynamics of water molecules at least as far as 10 Å from a protein's surface can be distinguished by terahertz spectroscopy from those of the bulk.[119] Using the dynamic fluorescence Stokes shift (FSS) response of a chromophore on the surface of a protein or on a tether, Zewail and coworkers[117,118,125] measured relatively long polar solvation timescales, in the 10–

100-ps regime. In contrast, almost half of the FSS response of bulk water is observed on the ultrafast (< 50-fs) timescale associated with inertial motions;[126,127] the remaining diffusive part of the solvation response that arises from reorientational motions exhibits sub-ps (126 fs and 880 fs) time constants.[70]

The long polar solvation timescales observed in the hydration layer were modeled phenomenologically by a dynamic exchange of water molecules between the hydration shell and binding sites on the protein surface.[117,128] Halle[124] has pointed out that the FSS results and exchange model are in conflict with the results of ^{17}O NMR relaxation dispersion (MRD) experiments and of molecular dynamics simulations of the dielectric response of a protein and its surrounding solvent, which suggest that the motions of water molecules in the hydration shell are only somewhat slowed compared to those in the bulk.[67] Halle and Davidovic[116,124] suggested that the apparent disagreement between the FSS and MRD experiments might be resolved if the viscosity of the hydration shell is larger than that of bulk water. This is in line with the hypothesis by Matyushov[129] that water is polarized by surface charges, which would lead to an increased viscosity of the hydration layer, which is indicative of changes in the long-range H-bonding structure of water near the surface of a protein.

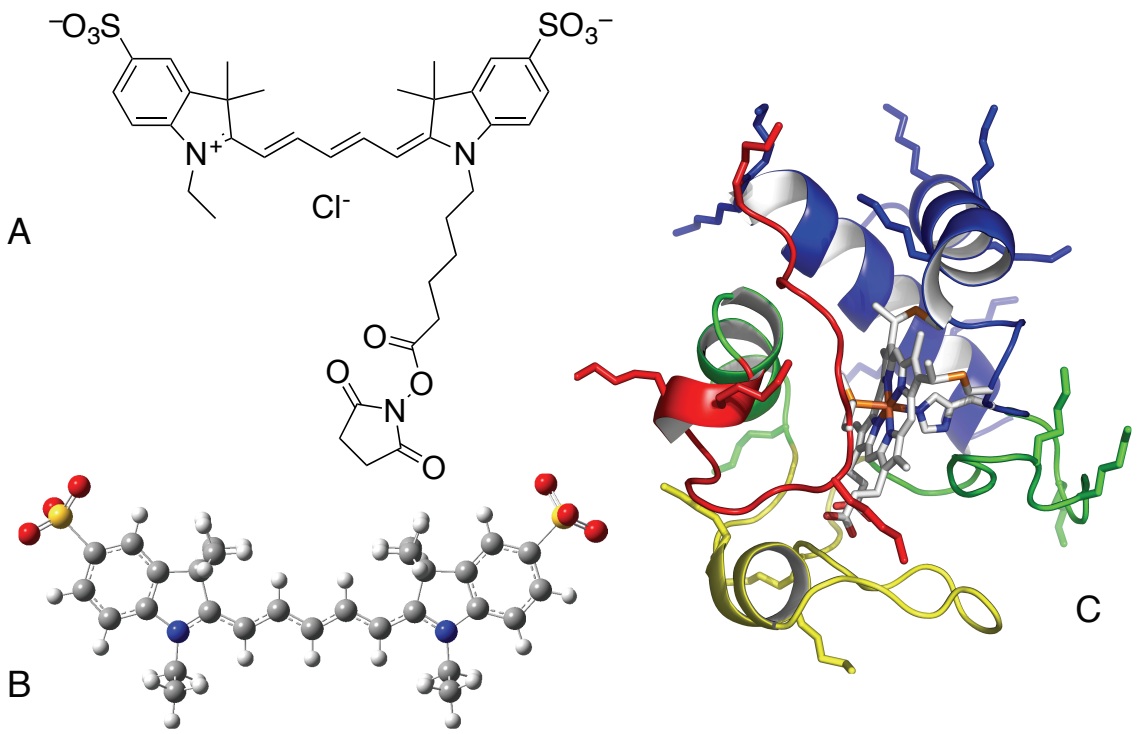

Figure 3.1. The structures of (a) the cyanine 5 NHS ester, (b) B3LYP geometry optimization of the cyanine 5 structure, and (c) ZnCytc protein with explicit lysine residues drawn.

In order to address these issues, we use cyanine 5 (Cy5) as a probe for nonpolar solvation in the hydration shell of Zn^{II}–substituted cytochrome *c* (ZnCytc). The assignment of Cy5 as a probe primarily for nonpolar solvation dynamics is discussed in **Section 2.1** of this dissertation. The Cy5 dye is available commercially (GE Healthcare PA25001) with a ~10 Å tether terminated either with a N-hydroxysuccinimidyl (NHS) ester for linkage to amines (see Figure 3.1a), or a maleimide group for linkage to cysteine residues. Cyanine dyes are commonly used in this capacity as probes for microscopic imaging,[72-74], and the varying chain lengths and substituents of commercially available cyanines allow for their utilization across relatively large spectral regions. Figure 3.2 shows the conjugation reaction of an R_1–substituted NHS ester with a lysine residue.

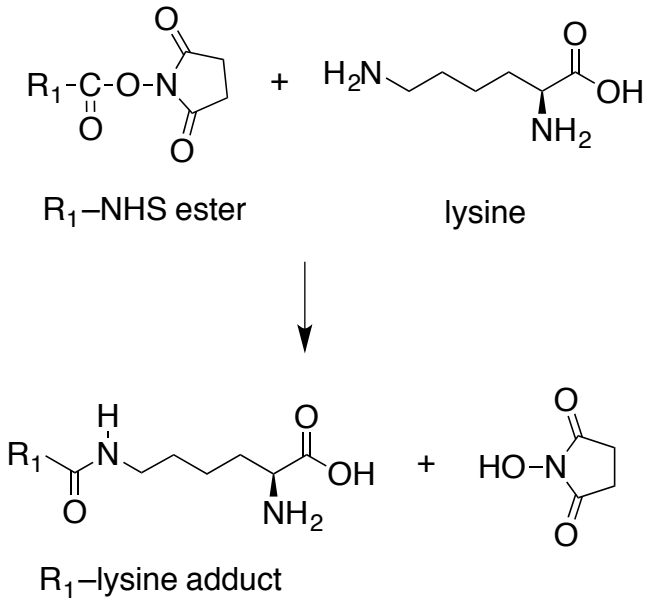

Figure 3.2. Example of an R_1–lysine conjugation reaction using an R_1–NHS ester.

3.2 Experimental

3.2.1 Sample Preparation. ZnCytc was prepared from horse-heart ferricytochrome *c* (Sigma C2867, >99%) using the procedure described by Vanderkooi.[130] Liquid anhydrous hydrogen fluoride (Linde) was used as the demetalating agent. The reaction was run on a home-built gas-handling system in Teflon reaction vessels. The metal-free or free-base protein (fbCytc) was isolated using strong cation ion-exchange chromatography on a Whatman CM-52 column. Reconstitution with Zn^{II} was performed at 50 °C in the presence of a 10-fold molar excess of zinc acetate (Sigma 379786, 99.999%). Completion of the demetalation and metal-reconstitution reactions were determined spectrophotometrically by observing differences in the number and position of bands in the Q band region of the absorption spectrum.

The ZnCytc product solution was further prepared using methods described by Winkler and coworkers[131] and by Kostić and coworkers.[132] The protein solution was desalted and the protein was isolated by cation-exchange chromatography on a clean Whatman CM-52 column. Fractions containing ZnCytc were equilibrated with 25 mM sodium phosphate buffer at pH 7.0 by repeated concentration over an Amicon YM-10 ultrafiltration membrane (Millipore) and subsequent dilution with the buffer solution. The final product was concentrated, aliquoted, flash-frozen, and stored at -80 °C prior to use.

The Cy5–ZnCytc complex was prepared by reacting a thawed sample of ZnCytc with the amine monoreactive N-hydroxysuccidimidyl (NHS) ester of Cy5 (GE Healthcare, PA25001, see Figure 3.1a) to prepare nonspecifically, a singly-labeled lysine adduct (see Figure 3.1c) according to the vendor's protocol. The reaction was conducted with protein concentration of ~3 mg/mL at pH 9.3 at room temperature in a 100 mM sodium bicarbonate sample buffer solution with enough Cy5 dye to obtain at best a 1:1 stoichiometry; the low protein concentration favors a lower adduct yield. Repeated ultrafiltration cycles with additions of 25 mM sodium phosphate buffer solution at pH 7.0 over YM10 membranes were used to separate unreacted and weakly bound Cy5 from the protein adducts. The adducts were concentrated further to obtain solutions for storage at −80 °C, as above. The final concentrated product was stored in 25 mM sodium phosphate buffer solution at pH 7.0. Cy5 solutions in water were prepared using the NHS ester of Cy5 at pH 7.0 in the 25 mM sodium phosphate buffer solution; the NHS ester hydrolyzes to yield a carboxylate at the end of the tether after prolonged exposure in aqueous solution.

For use in the femtosecond pump–probe experiments, solutions of Cy5–ZnCytc or Cy5 in water were prepared by diluting concentrated solutions to obtain an absorbance of 0.3 for a path length of 1.0 mm at the center of the laser spectrum at 665 nm. The samples were held in the femtosecond pump–probe spectrometer at room temperature (23 °C) in a stirred fused-silica cuvette (1.0-mm path length). The sample's absorption spectrum was monitored for changes arising from photochemistry or permanent photobleaching.

3.2.2 Mass Spectrometry. For use in mass spectrometric analyses, Cy5-ZnCytc and ZnCytc were treated with trypsin to obtain peptide fragments. After incubation overnight, the samples were analyzed using a Shimadzu Axima CFR Plus matrix–assisted laser desorption/ionization time-of-flight mass spectrometer (MALDI–TOF MS). The samples were prepared by placing 1 μL of sample (33.2 μM ZnCytc or 29.5 μM ZnCytc-Cy5 in 1 mM phosphate buffer) on a MALDI plate with 3 μL of the matrix α-cyano-4-hydroxycinnamic acid in 3:1 acetonitrile:0.1% trifluoroacetic acid. The samples were allowed to dry before being placed into the mass spectrometer. For mass calibration, the YAGFLR peptide (726.4 Da), bradykinin (1059.6 Da), and angiotensin I (1297.5 Da) were used as standards. Peaks were processed using the mass list display in the Shimadzu Biotech MALDI–MS program.

3.2.3 Linear Spectroscopy. The absorption and fluorescence instrumentation and methods are identical to what is reported in **Section 2.2.2** of this dissertation.

3.2.4 Femtosecond Pump–continuum-probe spectroscopy. The pump–continuum-probe instrumentation and methods are identical to what is reported in **Section 2.2.3** of this dissertation.

3.2.5 Photon Echo Spectroscopy. The photon-echo instrumentation and methods are identical to what is reported in **Section 2.2.4** of this dissertation.

3.2.6 Computational Chemistry. The optimized structure for the Cy5 chromophore shown in Figure 1b was obtained using Gaussian 03[110] using the B3LYP density functional and the 6-31G(d) level of theory. The length of the flexible tether between the tagged lysine residue's α carbon and the N atom in the indole moiety at the other end of the tether was estimated with structures optimized using the UFF molecular mechanics force field.

3.3 Results

3.3.1 Mass Spectrometry. MALDI–TOF mass spectrometry of enzymatically digested ZnCytc was performed to assign the positions of the Cy5 molecule near the surface of the protein. The results show that peptides 81-87, corresponding to Lys86 or Lys87, are the most likely to contain the Cy5 adduct. The next most likely Cy5 conjugated residues are Lys22 and Lys72. Gibson and coworkers[133] determined that the six most reactive lysines (of the 18 total) in the cytochrome *c* protein are residues 86 ,25, 72, 13 ,87, and 22 in order of decreasing reactivity. Taken with our results, this suggests that Lys86 is the most probable site for Cy5 conjugation. Our results show strong evidence for conjugation to three peptide fragments, corresponding to four possible lysines, but this does not rule out the possibility of conjugation to other lysines, below the detectable limit of the MALDI–TOF experiment. These results suggest that the measured dynamics are not specific to a single environment relative to the protein surface, but are likely a more

heterogeneous combination of three to four sites on the protein surface. Further, it is likely that a Cy5 molecule attached to a specific lysine residue inhabits multiple orientations relative to the protein at any given time.

3.3.2 Linear Spectra. Figure 3.3a shows the linear absorption (blue) and fluorescence (red) spectra of Cy5–ZnCytc along with the laser emission spectrum (black) and the absorption spectrum of a solution of the ZnCytc protein only (green). In Figure 3.3a, it can be easily observed that the additional structure on the blue side of the Cy5–ZnCytc absorption spectrum arises from the absorption of the ZnCytc protein. In Figure 3.3b, the same absorption and fluorescence spectra of Cy5–ZnCytc are overlaid with the absorption and fluorescence spectra of Cy5 in bulk water (dotted blue and dotted red respectively).

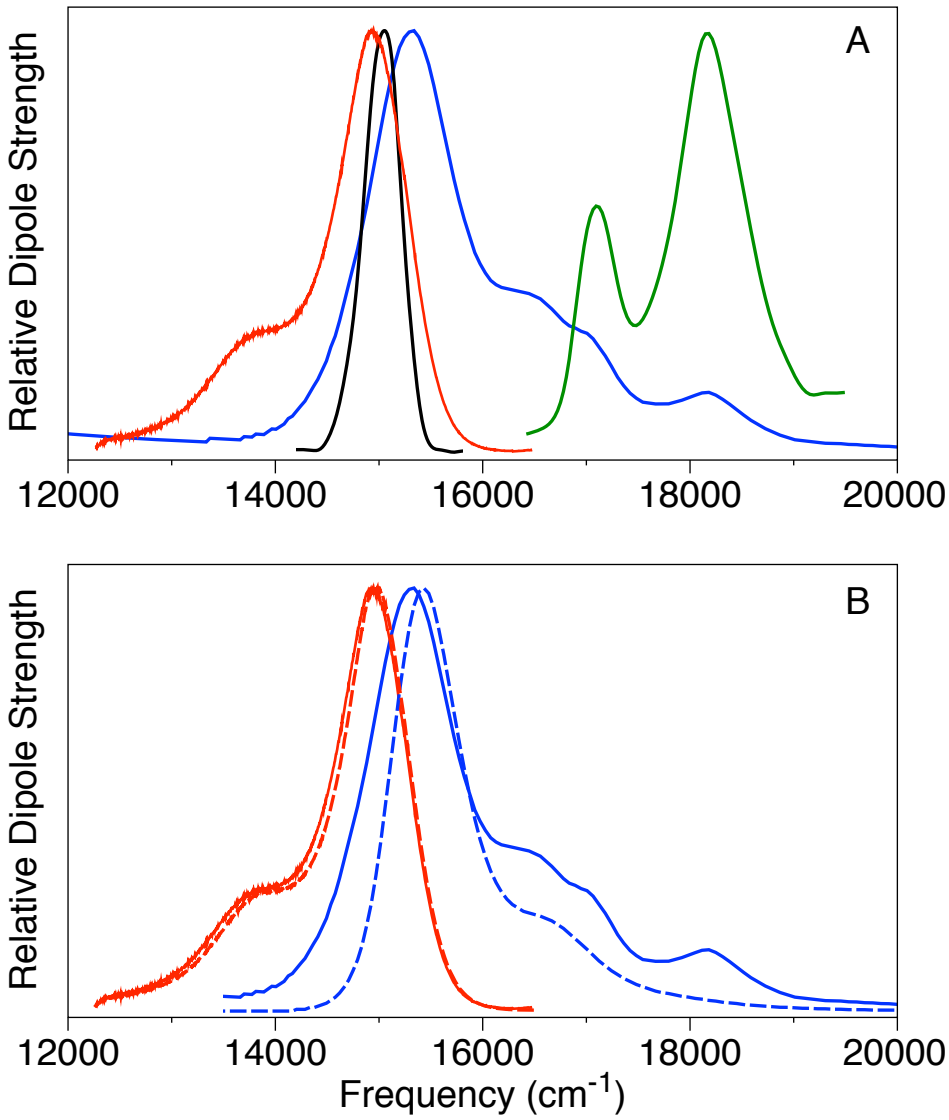

Figure 3.3. Room-temperature absorption (solid blue) and fluorescence (solid red) spectra of Cy5–ZnCytc. The spectra in (a) are superimposed with the laser emission spectrum (665-nm center wavelength, solid black line) and the absorption spectrum of isolated ZnCytc (green line). The spectra in (b) are superimposed with the absorption and fluorescence spectra of Cy5 in water (blue and red dotted lines, respectively) to accentuate the differences in overall profile and relative peak positions due to the hydration-shell environment.

The absorption and fluorescence spectra of Cy5 in water are modeled well by a sum of harmonically displaced lognormal line-shapes with a mode frequency of

1045 cm^{-1}. The red shift of the 0–0 peak of the fluorescence (F) spectrum relative to the absorption (A) spectrum provides an estimate for the solvation reorganization energy, λ,

$$\lambda = \frac{(\nu_{0-0,A} - \nu_{0-0,F})}{2} \tag{3.1}$$

The solvation reorganization energies for the similar symmetric cyanine dyes HDITCP and IR125 were determined by Jonas and coworkers[107] to be entirely nonpolar; the reorganization energies were insensitive to solvent polarity. We similarly assign the solvent reorganization energies for Cy5–ZnCytc and Cy5 in bulk water (195 and 225 cm^{-1}) primarily to nonpolar solvation, where the dynamics arise primarily from solvent and solute polarizability.[134] The reduced solvent reorganization energy observed for Cy5–ZnCytc may indicate that the hydration-shell medium is less polarizable than bulk water owing to its assumption on average of a different hydrogen-bonded structure than in bulk water.

3.3.3 Pump-Continuum-probe Spectra. Figure 3.4 shows the time evolution of the pump–probe spectra with the top panel showing the photobleaching spectrum (PB), which is the product of the laser and linear absorption spectrum. The very early-time spectra ($T < 0$ fs) show a nearly symmetric rise of the PB + SE signals centered near the 0–0 vibronic wavelength. This is evidence for pumping the entire homogeneous line-width as opposed to a subset of an inhomogeneously broadened ensemble. The red side of the main PB + SE peak increases with the instrument response function, while the blue side of the peak increases less quickly. An ESA feature to the blue of the main PB + SE peak appears around 50 fs and shifts to the

blue. These spectral dynamics are very similar to those of Cy5 in bulk water, though the pump-probe spectral widths for Cy5 in the hydration layer of ZnCytc are larger, owing to the increased width of the Cy5–ZnCytc linear absorption spectrum.

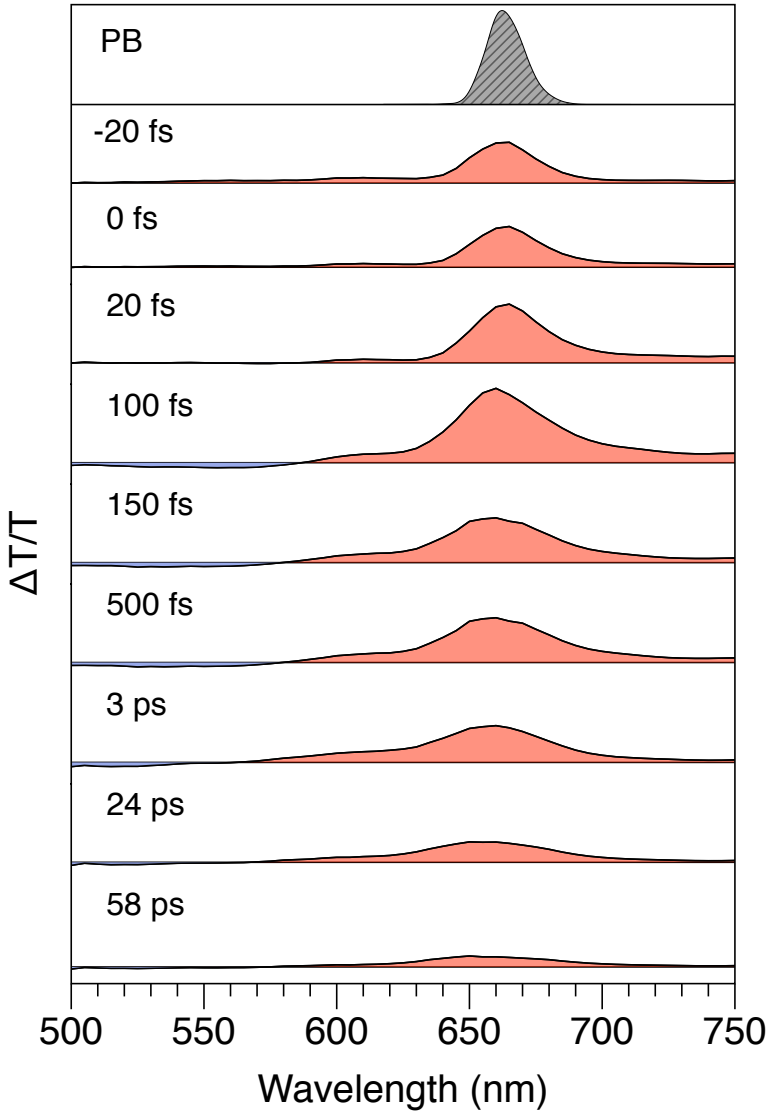

Figure 3.4. Time-resolved pump–continuum-probe spectra from cyanine 5 (Cy5) in water at selected pump–probe delay times *T*. The top panel (PB) shows the instantaneous photobleaching spectrum, which is estimated as the product of the laser spectrum and the absorption spectrum of Cy5–ZnCytc in water (see Figure 3.3a).

Figure 3.5a shows a pump–probe transient where the observed dynamics are entirely in the stimulated emission region (720 nm, 4 nm bandpass), with approximately no contribution from the PB component. The signal exhibits an instrument response-limited rise followed by a mulitexponential decay on top of which are multiple oscillations. The signal is fit with an iterative reconvolution routine (Figure 3.5a, black curve) using a solvent signal as an instrument response function. The residuals (signal – model) are plotted in Figure 3.5b (red points) and fit using a linear-prediction singular value decomposition (LPSVD) routine (3.5b, black curve). Figure 3.5c shows similar data to Figure 3.4b, only with Cy5 in bulk water. The LPSVD data for Cy5–ZnCytc is shown in Table 3.1. Cy5 in bulk water has large amplitude components at 260 and 430 cm^{-1}, with damping times of 50 and 120 fs respectively. In the hydration layer of ZnCytc, the corresponding oscillatory components are at lower frequencies (215 and 365 cm^{-1}) and have significantly faster damping times (40 and 65 fs). This is consistent with the picture of the hydration layer being significantly more viscous than bulk water.

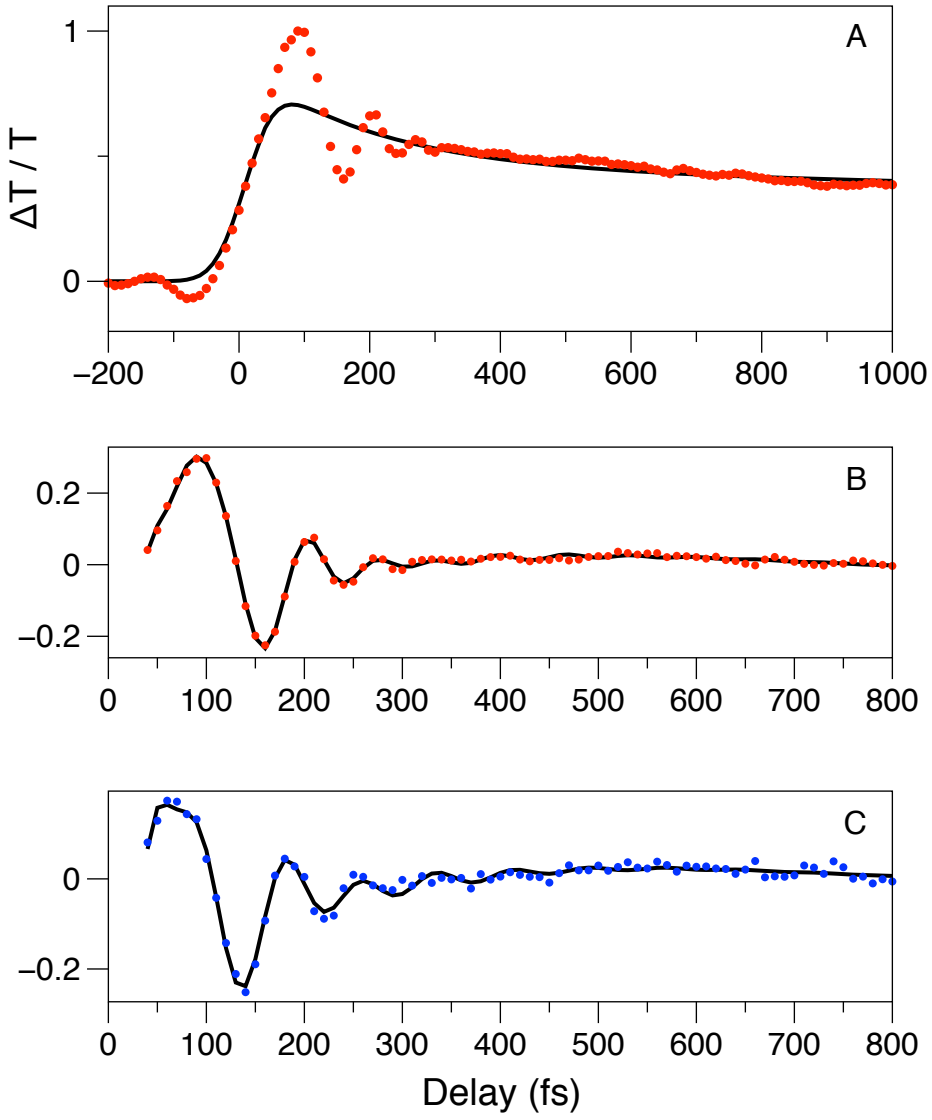

Figure 3.5. 665-nm-pump–720-nm-probe transient of Cy5–ZnCytc (red dots) modeled with an iterative reconvolution function (black line) consisting to multiple decay components. The residuals (signal – model, blue dots), (b), are fit with a linear prediction–singular value decomposition (LPSVD) routine (black line in (b)). The residuals and LPSVD model for Cy5 in water are shown in (c). The LPSVD data for Cy5–ZnCytc are presented in Table 3.1.

Table 3.1: Damped cosinusoids and exponentials determined by LPSVD analysis of the pump-probe 720 nm transient of cyanine-5 in the hydration shell of ZnCytc.

Amplitude	Damping Time (fs)	Phase (°)	Frequency (cm^{-1})
0.01	745 fs	157	35
0.73	40 fs	-184	213
0.24	65 fs	-89	366
0.02	145 fs	-29	505

3.3.4 Three-pulse Photon Echo Peak Shift Signals. Similar to Cy5 in water, the 3PEPS traces for Cy5–ZnCytc at each measured population time T were fit to a Gaussian and their peak-shifts relative to $\tau = 0$ are plotted in Figure 3.6. The ultrafast data is modeled as a sum of a Gaussian and an exponential by

$$M(t) = A_1 e^{-(t/\tau_1)^2} + A_2 e^{-(t/\tau_2)} + A_0 \tag{3.2}$$

where t is the population time, τ_n is an exponential timescale, and A_n is the component amplitude. The 3PEPS data were fit using Equation 2 for Cy5–ZnCytc and Cy5 in bulk water and the parameters are shown in Table 3.2.

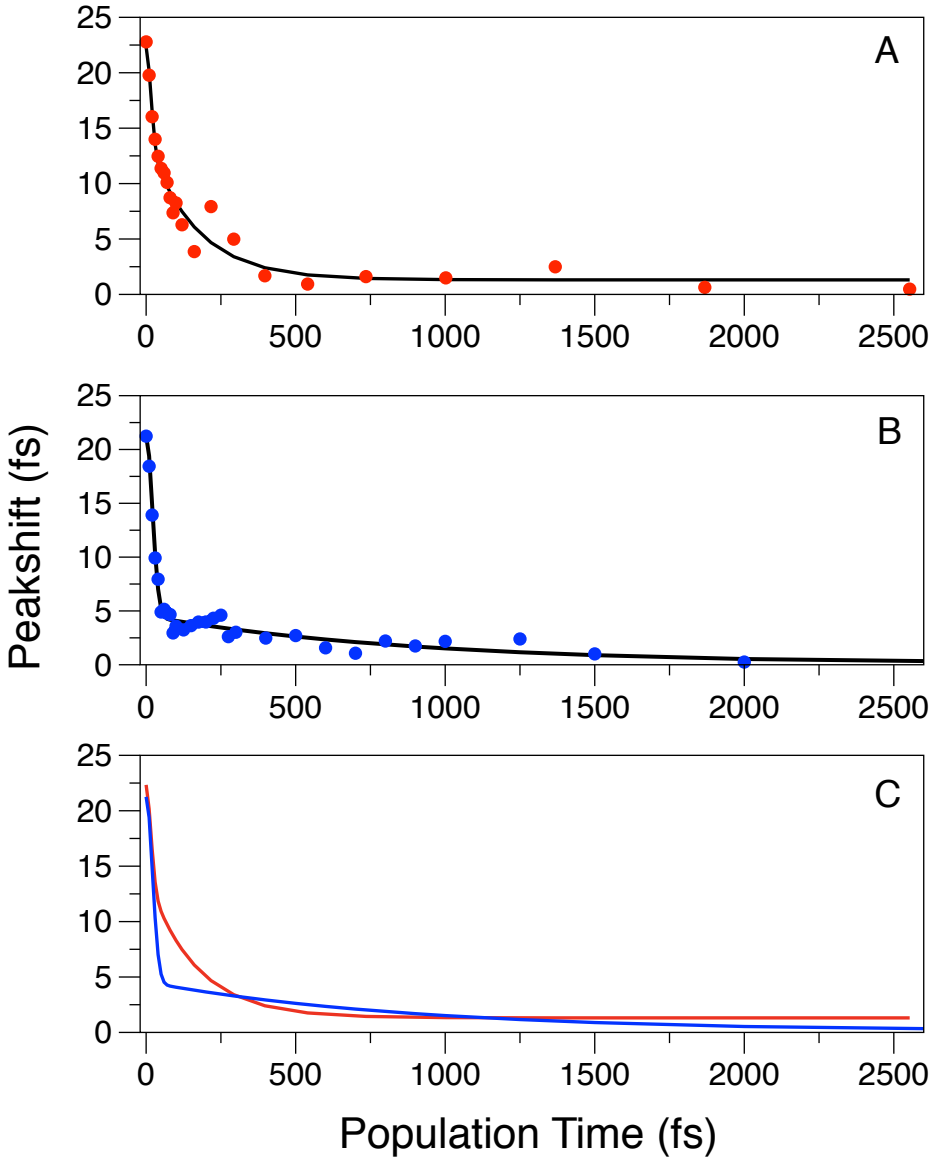

Figure 3.6. 3PEPS data for (a) Cy5–ZnCytc (red dots) and (b) Cy5 in water (blue dots) with their associated models (black lines) optimized via least-squares from Equation 3.2. The models are replotted in (c) (red: Cy5–ZnCytc, blue: Cy5 in water) to accentuate the differences in the $M(t)$ timescales. The optimized model parameters for the above systems are presented in Table 3.2.

Table 3.2: Model parameters of the 3PEPS data from Cy5ZnCytc fit to the $M(t)$ function

	A_1	τ_1	A_2	τ_2	A_0
Cy5 Water	0.78	21 fs	0.22	890 fs	0 fs
Cy5–ZnCytc	0.38	16 fs	0.62	160 fs	1.25 fs

Both systems have a very fast phonon induced component ($\tau \approx 20$ fs), but the fraction of $M(t)$, associated with this phonon induced component is about half as large in the hydration shell, with the other half decaying with an exponential timescale of 160 fs. This renders the average response over the < 300 fs timescale to be significantly slower in the hydration shell. Further, there is evidence for static inhomogeneity in the hydration shell-response from a longer lived offset of ~1.25 fs that does not decay on the measured timescale. This suggests that water in the hydration shell of ZnCytc has a more glass-like response than Cy5 in bulk water.

3.4 Discussion

Compared to Cy5 in bulk water, Cy5 in the hydration layer of ZnCytc exhibits significantly different nonpolar solvation dynamics as evidenced by the 3PEPS traces, as well as enhanced damping of coherence signatures observed in the pump–probe transients of the stimulated emission region. Taken together, this leads to the conclusion that the hydration shell is likely more viscous, but also organized differently than water in the bulk.

The vibrational coherence signatures in the pump–probe signals of the pure stimulated emission (SE) region of Cy5 in the hydration layer exhibit significantly

lower torsional mode frequencies compared to in bulk water. This can be attributed to an increase in solvent friction (viscosity) and is consistent with slowed polar solvation dynamics in studies of chromophores near the surface of proteins.[64,117,118] The significantly faster damping timescales for torsional motion in the hydration layer compared to bulk water can similarly be attributed to increase in viscosity. This faster damping could also be accounted for by a decreased barrier height to torsional deactivation in the hydration layer in accordance with Olivucci's two state two mode theory.[1] A decreased barrier height could be expected near a protein due to the interruption of the tetrahedral hydrogen-bond network that is thought to occur near surfaces[135]. This perhaps more chain-like hydrogen bond organization could be expected to have less of a hampering effect on torsional movement of the relatively bulky end-groups of the Cy5 molecule than a purely isotropic medium.

The nonpolar solvation dynamics of the early-time Gaussian, so-called "phonon induced" response component of $M(t)$ is much larger in bulk water than in the hydration shell of ZnCytc; $M(t)$ decays to a much lower value much faster in bulk water (see Figure 3.6c, Table 3.2). Interestingly, the exponential, diffusive response in the hydration shell has a faster decay than the smaller diffusive component in bulk water (160 vs. 890 fs), and $M(t)$ in the hydration layer terminates with an offset. This larger offset suggests either that there is a very slow diffusive component compared to the timescale of the 3PEPS measurement, or that there is static inhomogeneity; a disorder component that does not average out over time. Our data does not allow distinguishing between the two possibilities, but the

simplest explanation would be the slow diffusive component. A reasonable suggestion for the origin of the relatively fast exponential component-response is that this component is a bimodal extension of the phonon-induced component and the diffusive component decays on a timescale much greater than 2.5 ps. It is possible that this long-timescale component could arise from coupling of water motions with protein motions, where the water molecules are driven by the protein motions, which can be orders of magnitude slower than water motions.,[136-143]

Previous solvation studies on linear aliphatic alcohols of varying lengths showed that the extremely fast component decreased in amplitude relative to the diffusive component as the chain length (and viscosity) increased.[59] There was also a lengthening of intermediate-and long-timescale dynamics with increasing chain length. Extending this picture to our system would lead to the prediction of smaller and slower relative components corresponding to the 16-and 160-fs dynamic timescales and a larger offset on our experimental timescale if the viscosity of the hydration layer were to be increased. Previous studies on dynamics of chromophores within proteins by the Beck lab[144] and Fleming lab[145], on the other hand, show an increase in the fast, Gaussian component compared to the chromophore in the bulk. This leads to the conclusion that the hydration layer water is not protein like, except for the fact that proteins have long-lived inhomogeneity and slow diffusive components.

Previous studies by Matyushov *et al.*[146] suggest that the hydration shell is likely to be organized by two effects: the interface between the protein and the hydration shell breaks the long-range hydrogen bonding network of bulk water, and the

presence of charges on the protein surface tends to polarize the water molecules. These water molecules are oriented by the electrostatic interactions between the charges and the water dipoles. Due to this effect, there is likely to be a layer of water molecules that are pointing more or less in the same direction, which makes it impossible for the hydration layer waters to form four hydrogen bonds in an ice-like pattern. Instead, the waters make more pairwise or three-way interactions, making the average number of hydrogen bonds smaller. This idea is supported by 2D IR experiments where a reduced number of hydrogen bonds are thought to exist near interfaces.[135] The relative abundance of positive surface charges in the ZnCytc protein lead to the suggestion that a relatively large amount of water molecules would likely exist in this more linear hydrogen bonding configuration.

In this light, an alternate/additional suggestion for the origin of the faster exponential component in the hydration layer compared to bulk water can be proposed involving hydrogen bonding. In this picture, the reorientational (hydrogen bond switching) dynamics of a two-or three-way hydrogen bonded water molecule in the hydration shell should be faster than in the bulk, where reorientational motion involves breaking or switching of almost four bonds per molecule. We suggest that the differing dynamics of Cy5 in the hydration shell of ZnCytc are accounted for by an increase in effective viscosity compared to bulk water and the existence of an anisotropic structure of the water molecules, perhaps arranged in short linear, hydrogen-bonded chains.

CHAPTER 4

Excited-State Torsional Dynamics and Nonradiative Decay Intermediates from the S_2 State of β-Carotene

4.0 Summary

The electric-field resolved femtosecond transient-grating signal from β-carotene in benzonitrile at room temperature was acquired with optical heterodyne detection after resonant preparation of the S_2 ($1B_u^+$) state with 40 fs pulses at 520 nm. The absorption and dispersion components of the third-order signal exhibit distinct time profiles owing to nonradiative population of a series of dark states prior to recovery of the original ground state. The absorption component decays initially on an ultrafast (15 fs) timescale as contributions from stimulated-emission and excited-state absorption pathways shift rapidly to the red and blue, respectively, and fade away. This response is consistent with an initial displacement from the Franck–Condon structure along resonance Raman-active carbon–carbon bond-stretching and compression coordinates followed by symmetry breaking torsional motions that promote crossing of a barrier on the S_2 -state potential surface. Relaxation along torsional coordinates subsequently contributes a 140-fs decay component that reports decay of the S_2 state to the S_1 ($2A_g^-$) state, which exhibits a strong excited-state absorption signal. This intermediate time regime would be associated with mixing of the S_2 and S_1 states and the formation of an intramolecular charge-transfer character as the S_2-state twisted minimum is

approached. Comparison of the recovery timescales of the absorption and dispersion components indicates that nonradiative decay of the S_1 state initially yields a conformationally displaced ground-state (10 ps) prior to full recovery of the original ground state (12 ps). These results prompt the suggestion that the efficiency of carotenoid-to-chlorophyll energy transfer in photosynthetic light-harvesting proteins depends on steric and electrostatic control of the minimum-energy path on the carotenoid's S_2 -state potential surface along bond-alternation and torsional coordinates.

4.1 Introduction

Carotenoids are essential components in the photosynthetic light-harvesting and reaction-center proteins of photosynthetic organisms owing to their involvement in photoprotection mechanisms and in light harvesting. [2,3,6,9] They serve as strong antenna chromophores in the mid-visible, where the terrestrial solar spectrum is the most intense, through strong, electric-dipole-allowed transitions from the ground state, S_0 ($1A_g^-$), to the S_2 ($1B_u^+$) excited state (Figure 4.1).[9,147] Because the lifetime of the S_2 state is very short, typically less than 250 fs, the formally dark S_1 ($2A_g^-$) state plays a crucial role in excitation energy transfer (EET) from carotenoids to chlorophylls. The rate of EET by the Förster mechanism from the S_1 state is apparently enhanced in light-harvesting proteins by placing the carotenoid nearly in van der Waals contact with an adjacent chlorophyll so that the Coulomb coupling between them is optimized.[45,148]

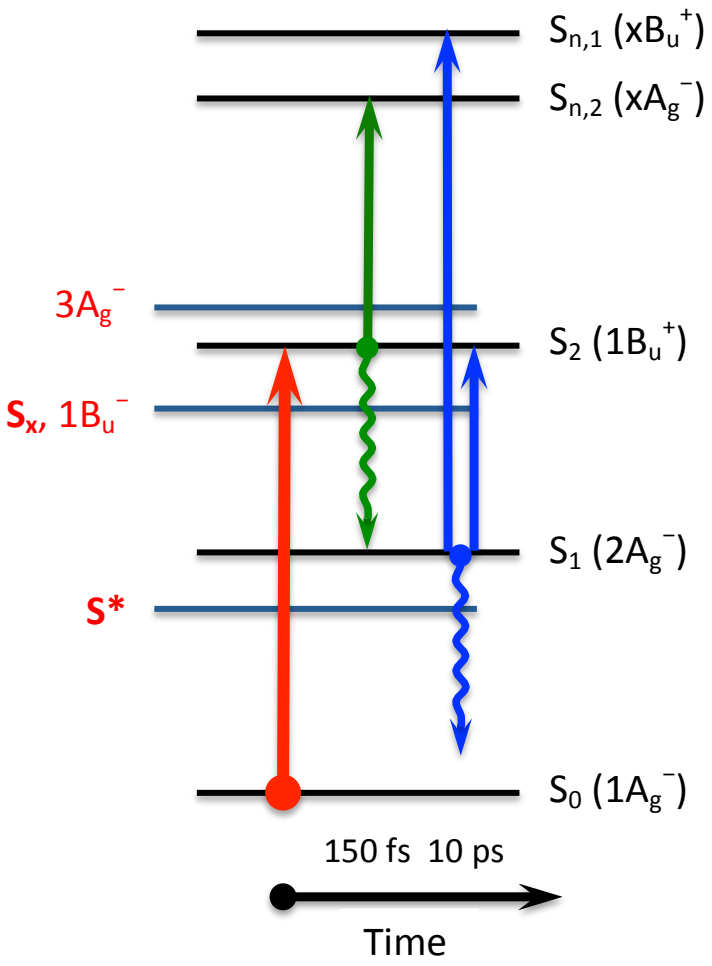

Figure 4.1. Electronic energy levels of carotenoids and transitions that contribute to nonlinear optical signals following optical preparation of the S_2 state, after Polívka and Sundström.[9] The one-photon transitions of most carotenoids effectively follow the selection rules for molecules belonging to the C_{2h} point group; transitions between states of the same symmetry (g→g, u→u) and pseudoparity (+→+, −→−) are electric-dipole forbidden.[10,11] The first strongly allowed optical transition is $S_0 \rightarrow S_2$. Weak fluorescence is observed from the formally dark S_1 state,[12,13] which shows that the S_1 state is rapidly accessed via internal conversion. Dark states suggested by previous work are marked by blue lines and red labels. Nonradiative decay transitions that deactivate the S_2 state are indicated with wavy arrows; excited-state absorption transitions that contribute to pump–probe and transient-grating signals are shown as solid arrows. The timescale increases from left to right in the diagram.

The rate of EET would be further enhanced in a light-harvesting protein by binding carotenoids in sites that favor an assumption of a twisted conformation because the bright S_2 and dark S_1 excited states would mix and develop

intramolecular charge-transfer character as a conical intersection is approached along torsional coordinates.[21,55,149-152] Twisted conformations may be involved in the nonradiative decay pathways initiated from the S_2 state that populate the S_x ($1B_u^-$) and S^* dark states in carotenoids, which have been the subject of controversy.[9] The involvement of the S_x state as a bridging intermediate is strongly suggested by deviation of the $S_2 \rightarrow S_1$ internal conversion rates of carotenoids of varying lengths from the energy gap law[12,27,37] and by detection of an excited-state absorption band prior to the formation of the S_1 state.[22,28,30,153] Observation of an off-diagonal cross-peak in 2D electronic stimulated photon-echo experiments supports the suggestion that the S_x state mediates energy transfer from the carotenoid S_2 state to the bacteriochlorophyll Q_x state in purple bacterial light-harvesting proteins.[24,25] The S^* state, which is marked by formation of a blue shoulder on the $S_1 \rightarrow S_n$ ESA transition in the transient absorption spectrum, has been assigned to the vibrationally excited S_0 state, as generated by nonradiative decay from the S_1 state[39] or by stimulated Raman scattering with resonant S_2 -state excitation.[23] An alternative suggestion is that S^* arises from a discrete electronic state lying below the S_1 state energy that has a twisted conformation.[40-42]

A spectroscopic approach for the detection and characterization of the dark states that contribute to the nonradiative decay of carotenoids is suggested by the work of Fleming and coworkers, who used femtosecond transient-grating spectroscopy with optical heterodyne detection to study nonradiative decay mechanisms involving excited-state torsional dynamics in triphenylmethane (TPM) dyes.[54,154] Optical heterodyne detection permits a full characterization of the

electric field of the third-order nonlinear optical signal in terms of two components in quadrature, the absorption and dispersion components. The resonant solute and nonresonant solvent signals can be distinguished more readily in optical heterodyne experiments than in experiments with homodyne detection, which detects the sum of the squares of the absorption and dispersion components.[108,155] The transient-grating signals from TPM dyes were shown to exhibit strikingly different kinetic profiles and pump-wavelength-dependent decay timescales owing to the formation of intermediate states prior to recovery of the original ground state.[54,154]

In this contribution, we have followed a similar approach to characterize the nonradiative decay dynamics from the S_2 state of β-carotene (Figure 4.2) at room temperature. Optical heterodyne detection was performed with Fourier-transform, spectral interferometric methods[156] using a passively phase-stabilized photon-echo/transient-grating spectrometer. By detecting the absorption and dispersion components of the transient-grating signal separately, we observe directly the dynamics on the S_2 -state potential surface that initiates nonradiative decay to the S_1 and S_0 states. The results show that after optical preparation of the S_2 state and an initial displacement along resonance Raman-active carbon–carbon bond-stretching and compression coordinates, β-carotene undergoes a rapid structural evolution away from the Franck–Condon geometry along torsional motions that promote crossing of an activation-energy barrier leading to a twisted or pyramidalized minimum.

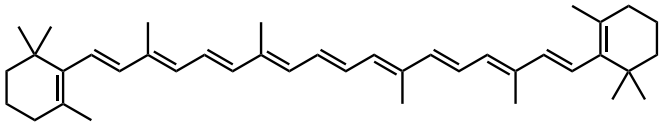

Figure 4.2. Structure of β-carotene.

4.2 Experimental

4.2.1 Sample Preparation. β-carotene samples were obtained from Sigma-Aldrich (catalog no. C9750) and purified by high-performance liquid chromatography (HPLC) using a Waters 600E/600S multisolvent delivery system equipped with a 2996 photodiode array detector as described previously.[157] The column was a Waters Atlantis Prep T3 OBD 5 μm column (19 x 100 mm). Acetonitrile was delivered isocratically with a 7.0 mL/min flow rate. Samples collected from the HPLC were dried under nitrogen gas and stored at -20°C until further use.

4.2.2 Linear Spectroscopy. Prior to use in transient-grating experiments, linear absorption spectra were acquired with freshly prepared solutions of β-carotene in methanol with a Hitachi U-4001 spectrophotometer.

4.2.3 Nonlinear Spectroscopy. Femtosecond transient-grating signals were acquired at room temperature (295 K) using optical heterodyne detection with a passively phase-stabilized photon-echo spectrometer and Fourier-transform spectral interferometry. The experiments were performed with 35-40-fs, 520-nm excitation pulses obtained from an optical parametric amplifier (OPA, Coherent OPA 9400), which was pumped by a 250-kHz amplified Ti:sapphire laser (Coherent Mira-Seed oscillator and RegA 9050 regenerative amplifier).

The design of the photon-echo spectrometer follows aspects of the designs discussed by Moran and Scherer[108] and Brixner *et al.*[109] A transmission diffractive optic (285 gr/mm) was employed to prepare pump and probe pulse pairs required for the stimulated photon-echo or transient-grating experiment. The pulse program was controlled using a time-of-flight delay controlled by a Nanomover actuator (Melles Griot) for the pump–probe population delay T; a second Nanomover actuator controlled the lateral translation of wedge-shaped prisms in the pump beams to control the coherence delay τ, which was set to zero for transient-grating experiments. 20-cm focal-length mirrors were used to collimate the four pulses emerging from the diffractive optic and then to focus them onto the sample in the forward boxcars configuration (see Figure 2.7).

Transient-grating measurements were made with β-carotene/methanol samples held at room temperature in a 1-mm cuvette with an optical density of ~0.3 at the laser wavelength of 520 nm. The third-order signal, as overlapped with the local oscillator beam in the $-\mathbf{k}_1+\mathbf{k}_2+\mathbf{k}_3$ phase-matched direction, was tightly spatially filtered after the sample using a series of iris diaphragms and then was collimated and focused into a spectrograph (Spex 270m, 1200 gr/mm grating) by a pair of spherical lenses. The spectral interferogram from the third-order signal and local oscillator was detected using a back-illuminated, liquid nitrogen-cooled CCD detector (Princeton Instruments VersArray 1300B, 700 × 1300 pixels, 100-ms integration time/spectrum). Scattered light was removed using the beam-shuttering protocol outlined by Brixner *et al.* [109] The spectrometer was controlled by *LabVIEW* (National Instruments) programs.

4.3 Results

4.3.1 Linear Spectra. Figure 4.3 shows the linear absorption spectrum at 22 °C for β-carotene in benzonitrile solvent. For the transient-grating experiments discussed here, the spectrum of the OPA's signal output was tuned to overlap with the onset of the S_0 $(1A_g^-) \rightarrow S_2$ $(1B_u^+)$ absorption spectrum. This tuning selects the 0–0 vibronic transition of the lowest energy, ground-state conformers.[36] The laser spectrum has a full-width at half maximum (FWHM) intensity of ~8 nm. It spans the 505-542 nm probe region from baseline to baseline.

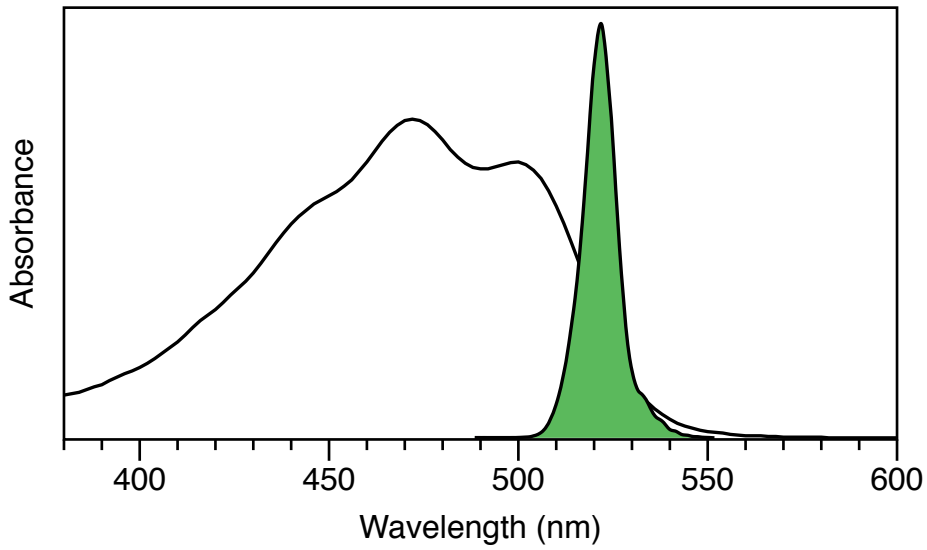

Figure 4.3. Room-temperature absorption spectrum of β-carotene in benzonitrile solvent. Superimposed is the output spectrum of the 40 fs OPA signal beam (519-nm center wavelength), as tuned for the heterodyne transient-grating experiments.

4.3.2 Transient-grating Spectra. Transient-grating signals from β-carotene in benzonitrile were acquired with optical heterodyne detection by Fourier-transform spectral interferometry following the approach described by Jonas and coworkers[156] and the methods implemented by Brixner *et al.*[109] The detection,

processing and interpretation of third-order nonlinear optical signals was previously outlined by Moran, Scherer, and coworkers,[108,155] and the following summary adopts their notation.

In the transient-grating experiment, two pump pulses arrive synchronously (with coherence time $\tau = 0$) at the sample position along wavevectors $\mathbf{k}_1$ and $\mathbf{k}_2$. After a population (or waiting) time T, the probe pulse arrives along wavevector $\mathbf{k}_3$. The sample then emits a signal (frequency ω_t, with emission time $t > 0$ with respect to the probe pulse) in the $\mathbf{k}_s = -\mathbf{k}_1 + \mathbf{k}_2 + \mathbf{k}_3$ direction. When optical heterodyne detection is employed, a weak local oscillator (LO) pulse arrives at the sample prior to the probe pulse along the $\mathbf{k}_s$ wavevector so as to interfere with the third-order signal; in our experiment the LO and probe pulses are spaced by ~800 fs (See Figure 4.4; photon-echo pule program). A transient-grating transient is acquired by scanning the population time T to carry the probe pulse from negative to positive delays with respect to the pump pulses. The data-acquisition and data-processing cycles described by Brixner *et al.*[109] were employed to acquire a spectral interferogram that carries the third-order signal and lacks background scattering by alternately shuttering beams 1 and 3.

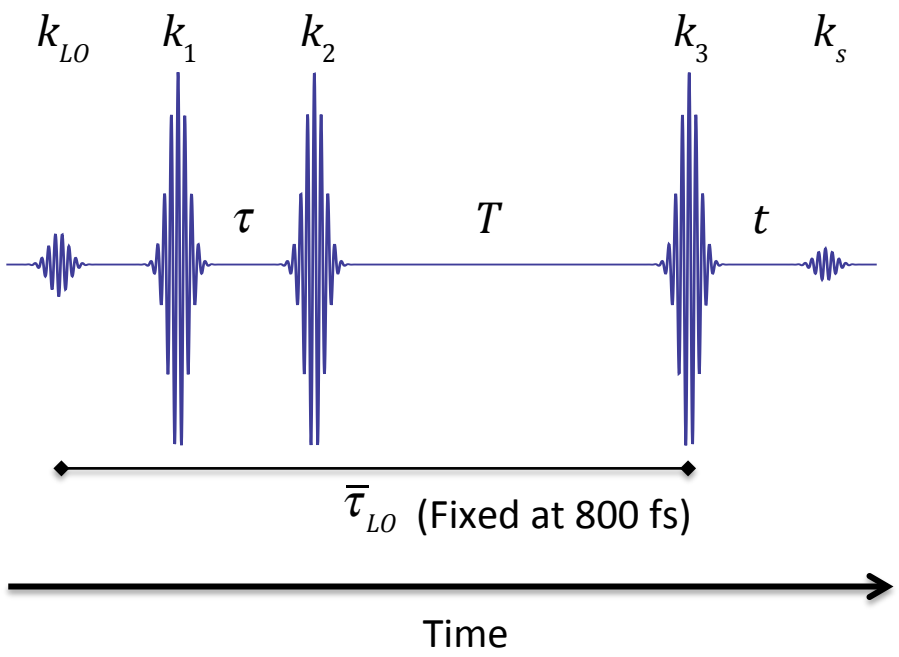

Figure 4.4. Example of a photon echo pulse program for a heterodyne experiment. The coherence time τ is scanned using wedged prisms, the population time T is scanned using a retroreflector in an optical delay line (ODL), and t is the emission time, which depends upon the pulse ordering and value of τ for a given detection vector. The local oscillator is the first pulse to arrive at the sample position, but is sufficiently weak to have negligible interactions. The delay between the local oscillator (LO) and pulse 3 remains fixed ($\overline{\tau}_{LO}$) and determines the fringe spacing of the heterodyned signal spectrum (see Figure 4.5). For three-pulse photon echo peak-shift (3PEPS) and 2D experiments, τ is scanned from a negative value (pulse along k_2 arrives before pulse along k_1) to a positive value (τ is typically scanned from –120 to 120 fs). These experiments also require the population time T between the temporal second and third pulses to remain constant; this is accomplished by moving the ODL when appropriate. For transient-grating experiments, τ is fixed at $\tau = 0$ fs and the population time T is scanned.

The third-order signal field, $E_s^{(3)}(t,T,\tau)$, is the sum of the fields from the nonresonant solvent and resonant solute and is related to their third-order polarizations $P^{(3)}(t,T,\tau)$ by

$$E_s^{(3)}(t,T,\tau) = \frac{i2\pi l\omega_t}{n(\omega_t)c}\left(P^{(3)}_{\text{solvent}}(t,T,\tau) + P^{(3)}_{\text{solute}}(t,T,\tau) \right) \qquad (4.1)$$

where l is the length of the sample cell, $n(\omega_t)$ is the refractive index, c is the speed of light, and T and τ are the interpulse delays that specify the three-pulse program. $P^{(3)}(t,T,\tau)$ is determined by the three successive actions of the electric fields $E_i(\boldsymbol{k}_i,\tau)$ from the three pulses that define a bleaching, stimulated-emission, or excited-state absorption pathway, as discussed in detail elsewhere.[108,158] Optical heterodyne detection obtains the spectral interferogram $I_{\mathrm{tot}}(\omega_t,T,\tau,\overline{\tau}_{LO})$ as [108]

$$I_{\mathrm{tot}}(\omega_t,T,\tau,\overline{\tau}_{LO})=\left|\int_{-\infty}^{\infty}\mathrm{d}t\left(E_S^{(3)}(t,T,\tau)+E_{\mathrm{LO}}(t-\overline{\tau}_{LO})\exp(\mathrm{i}\omega_t t)\right)\right|^2 \tag{4.2}$$

where $E_{\mathrm{LO}}(t-\overline{\tau}_{LO})$ is the electric field of the local oscillator and $\overline{\tau}_{LO}$ is the time-delay between the peaks of the local oscillator and probe pulses. Fourier-transform methods[109,156] isolate the third-order signal as a complex cross term,

$$\begin{aligned} &I_{\mathrm{het}}(\omega_t,T,\tau,\overline{\tau}_{LO};\varphi_{\mathrm{LO}}(\omega_t))= \\ &I_s(\omega_t,T,\tau)I_{\mathrm{LO}}(\omega_t)\exp\left[\mathrm{i}(\varphi_s(\omega_t)-\varphi_{\mathrm{LO}}(\omega_t)-\omega_t\overline{\tau}_{LO})\right] \end{aligned} \tag{4.3}$$

where $I_s(\omega_t,T,\tau)$ is the signal intensity, $I_{\mathrm{LO}}(\omega_t)$ is the intensity of the local oscillator, and $\varphi_s(\omega_t)$ and $\varphi_{\mathrm{LO}}(\omega_t)$ are the phases of the signal and local oscillator, respectively. In the following results, the phase $\varphi_{\mathrm{LO}}(\omega_t)$ was determined experimentally either by performing a heterodyne transient-grating experiment with neat solvent[108] or by comparing the transient-grating spectrum to the pump–probe transmission spectrum from a resonant sample.[109,159] The $I_{\mathrm{LO}}(\omega_t)$ term is obtained from a separately acquired spectrum of the local oscillator, $\left|I_{\mathrm{LO}}(\omega_t)\right|^2$, which allows the signal field to be isolated as

$$E_S^{(3)}\left(\omega_t,T,\tau\right)=I_S\left(\omega_t,T,\tau\right)\exp\left[-\mathrm{i}\varphi_S\left(\omega_t\right)\right] \tag{4.4}$$

The real and imaginary parts of $E_S^{(3)}\left(\omega_t,T,\tau\right)$ obtain the absorption and dispersion components, respectively. The modulus squared or power spectrum,

$$\left|E_S^{(3)}\left(\omega_t,T,\tau\right)\right|^2 \equiv \mathrm{Re}\left[E_S^{(3)}\left(\omega_t,T,\tau\right)\right]^2+\mathrm{Im}\left[E_S^{(3)}\left(\omega_t,T,\tau\right)\right]^2 \tag{4.5}$$

is proportional to the homodyne signal collected by a square-law detector along the $\mathbf{k}_S$ wavevector in the absence of an LO field. Figure 4.5 illustrates this data processing routine.

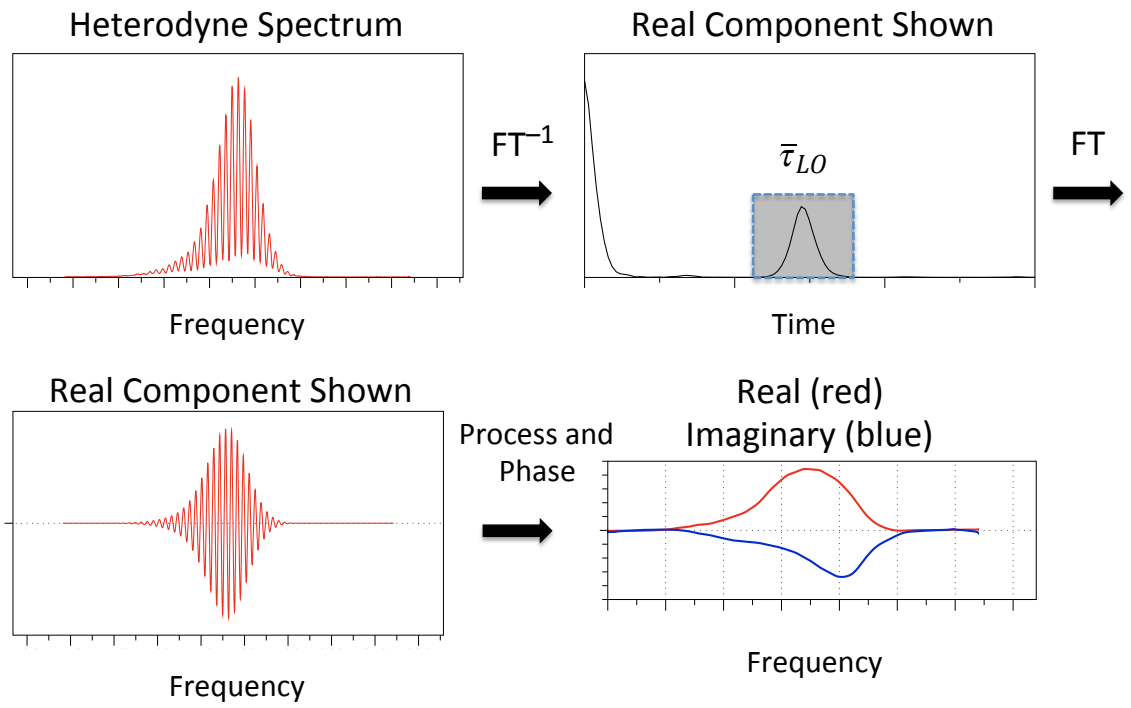

Figure 4.5. Diagram illustrating Fourier transform spectral interferometry (FTSI) on a heterodyned spectrum of rhodamine 6G at a population time of 50 fs. The signal beam detected along the $-\mathbf{k}_1+\mathbf{k}_2+\mathbf{k}_3$ phase-matching direction is a heterodyned spectrum. Fourier filtering (performing an FT^{-1}, windowing the oscillatory component around $\bar{\tau}_{LO}$ (b), and performing an FT back to the frequency domain) recovers the complex cross term (c, Equation 4.3) which contains components from the signal and local oscillator (LO). The signal spectra (d, Equation 4.4) are obtained by using the measured value of $\bar{\tau}_{LO}$, determining the phase of the local oscillator (φ_{LO}) using a nonresonant sample, and dividing out the intensity profile of the LO ($I_{\mathrm{LO}}(\omega_t)$) using the square root of its measured spectrum.

4.3.3 Transient-grating Signals. Figures 4.6 and 4.7 show the population time T profiles of the transient-grating signal from β-carotene in benzonitrile with integration over the emission frequency axis spanned by the laser spectrum,

$$E_S^{(3)}(T) \equiv \int \mathrm{d}\omega_t E_S^{(3)}(\omega_t, T, \tau = 0) \tag{4.6}$$

The phase for the local oscillator is chosen here so that the sign of the dispersion component, $\mathrm{Im}[E_S^{(3)}(T)]$, is negative for a nonresonant solvent. The dispersion from

neat solvent is negative over the laser's spectral bandwidth because it is proportional to $-n_{\text{solvent}}(\omega)$, with the negative sign determined by the Kramers–Kronig relation.[54,160] With this choice of phase, the absorption component, $\text{Re}[E_S^{(3)}(T)]$, is positive for photobleaching (PB) and stimulated-emission (SE) pathways, effectively relating an increase in the third-order signal intensity; excited-state absorption (ESA) pathways contribute a negatively signed signal.

The absorption component (Figure 4.7a) exhibits an instrument-limited rise dominated by PB and SE pathways followed by an ultrafast, multicomponent decay ending in a negatively signed signal with ESA pathways dominant. In contrast, the dispersion component's (Figure 4.7b) profile is single-signed and monotonic increasing, so the dispersion is dominated by ESA pathways; its rise appears to be delayed for about 40 fs compared to that for the absorption component. Both components decay to the baseline on the ~10-ps timescale (see Figures 4.8a and 4.8b). The recovery timescale is consistent with the lifetime of the S_1 ($2A_g^-$) state measured previously in transient absorption experiments.[161]

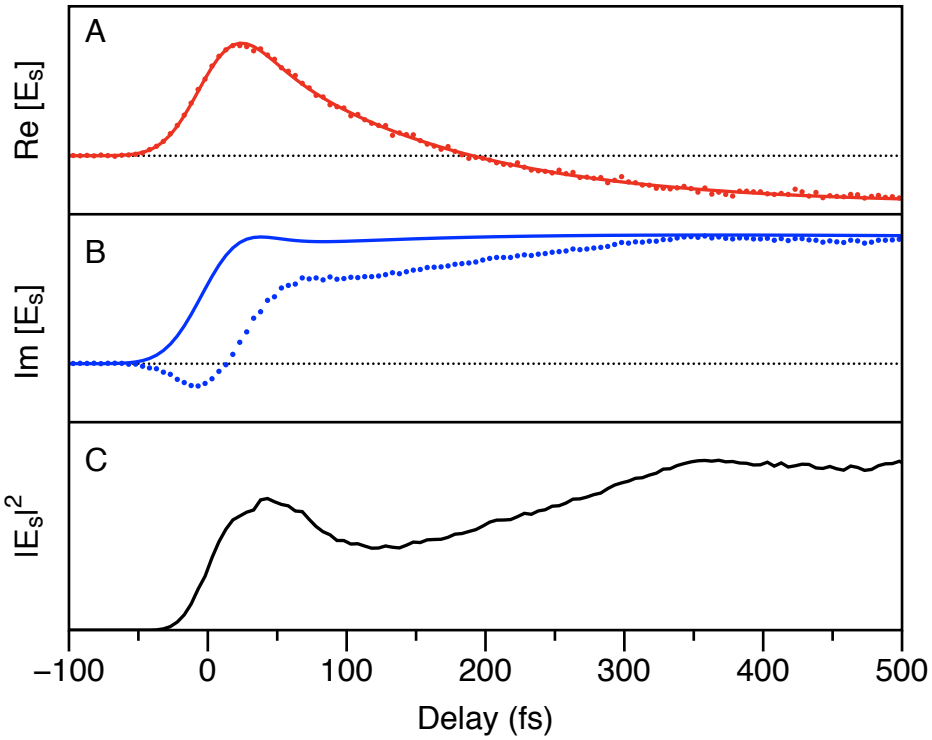

Figure 4.6. Spectrally-integrated transient-grating signals from β-carotene in benzonitrile at room temperature: (a) absorption component; (b) dispersion component; (c) the complex modulus. In (a) and (b) the data points are superimposed with kinetic models (solid line) described in the text that account for contributions from the benzonitrile solvent to the dispersion component. The complex modulus (c) was calculated directly from the sum of the squares of the data points in (a) and (b). Figure 4.7 shows the same signals on an expanded delay scale (12 ps).

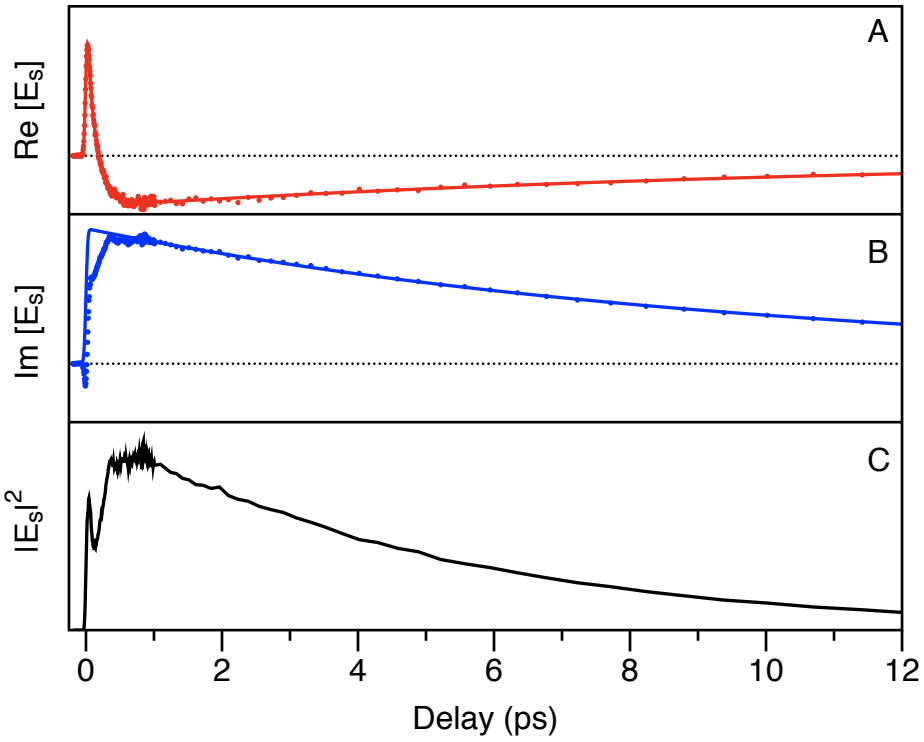

Figure 4.7. Spectrally-integrated transient-grating signals from β-carotene in benzonitrile at room temperature: (a) absorption component; (b) dispersion component; (c) the complex modulus. Additional details are as described in Figure 4.6, which shows the same signals over the <500-fs delay scale.

The profile of the modulus, $\left|E_S^{(3)}(T)\right|^2$, conceals most of the early time dynamics because the absorption and dispersion time profiles are combined (see Figures 4.6c and 4.7c). As calculated directly as the sum of the squares of the two components (Equation 4.5), the modulus exhibits a single-signed profile that resembles the homodyne transient-grating signals observed previously by Christensson *et al.*,[32] but without the large spike near the zero of time that they reported. The spike in the solvent signal in the early-time homodyne transient-grating signal comes from an interference cross term in the squared sum of the components of the solvent signal.[154]

The solvent contribution to the transient-grating signals can be determined in heterodyne experiments[154,162] using the signal from neat solvent (Figure 4.8) and a solute concentration series (Figure 4.9). The very weak absorption component of the transient-grating signal from neat benzonitrile (Figure 4.8a) arises from self-phase modulation; it is not significant at delays $T > 75$ fs. In contrast, the dispersion component (Figure 4.8b) is intense because benzonitrile is highly polarizable; it exhibits a large, negative peak near time zero followed by a slower decay that is complete at about 800 fs arising from a strong nuclear (vibrational, largely overdamped) response.[162] At low β-carotene concentrations, the solvent makes a dominant contribution to the modulus signal at zero time (Figure 4.9c). At higher β-carotene concentrations, the solvent's contribution to the signal near the zero of time is increasingly suppressed by the inner filter effect.[154] The solvent peak in Figures 4.8b and 4.8c occurs at an earlier time and is sharper in shape than the peak in Figure 4.9a, which arises primarily from the initial rise and decay of the β-carotene's solute contribution to the absorption component. (Note that the modulus transients shown in Figures 4.6c and 4.7c are the same as that shown in Figure 4.9a.)

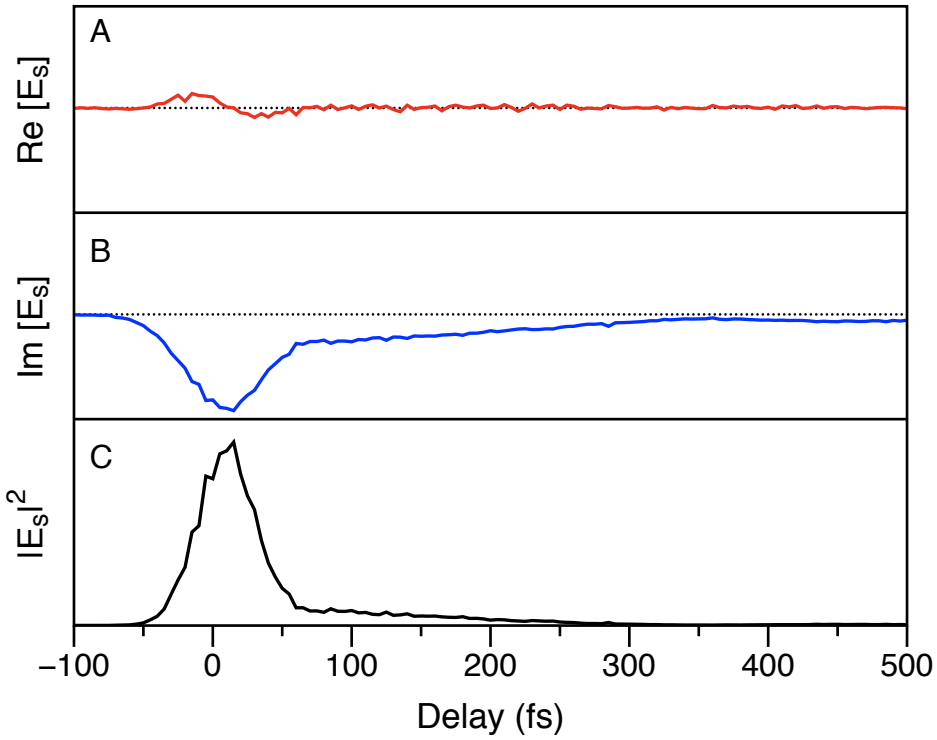

Figure 4.8. Spectrally-integrated transient-grating signal from neat benzonitrile at room temperature under the same measurement conditions used for β-carotene in Figures 4.6 and 4.7: (a) absorption component; (b) dispersion component; (c) complex modulus.

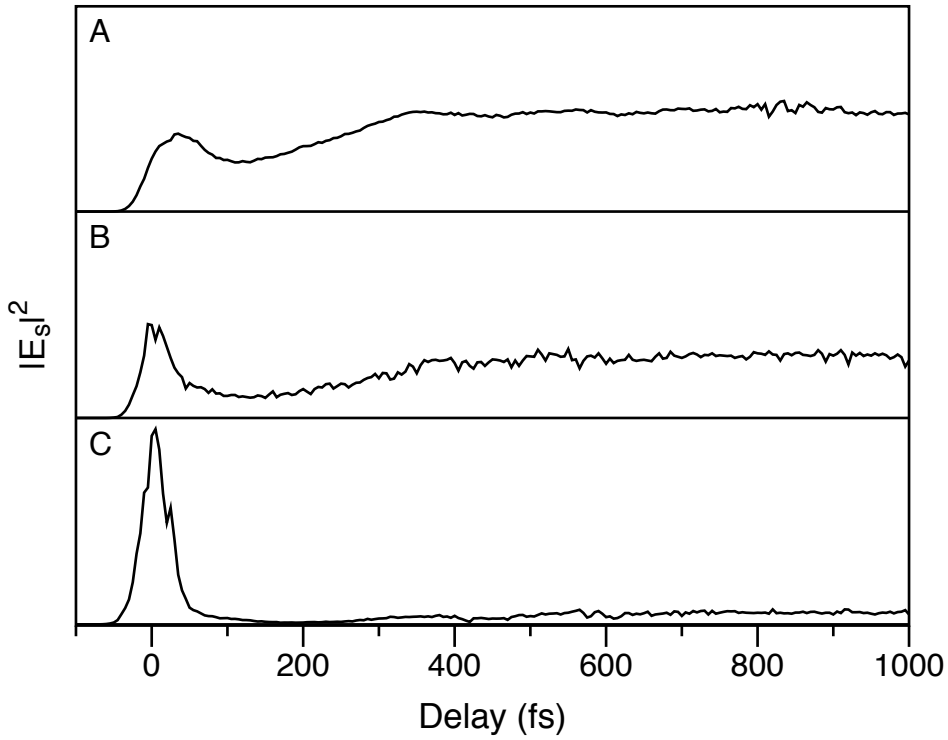

Figure 4.9. Complex modulus of the heterodyne transient-grating signals from β-carotene in benzonitrile at three solute optical densities: (a) A = 0.26, as in Figures 4.6 and 4.7; (b) A = 0.13; and (c) A = 0.07.

4.3.4 Modeling of the β-carotene Transient-grating Signal. In Figures 4.6 and 4.7, the absorption component of the transient-grating signal from β-carotene is shown superimposed with a model obtained from convolution of a system-response function with a Gaussian-shaped instrument-response function. The instrument-response function was estimated from the dispersion component of the transient-grating signal from neat methanol. The system-response function requires a sum of three exponentials to describe adequately the absorption component's time profile. After nonlinear least-squares optimization using iterative reconvolution, the optimized system-response function contains two decay components with time

constants of 16 fs and 142 fs and a rising component with a 9.8 ps time constant (see Table 4.1).

The simplest kinetic model consistent with this response consists of a linear sequence of four states:

$$S_2 \xrightarrow{k_1} I \xrightarrow{k_2} S_1 \xrightarrow{k_3} S_0 \tag{4.7}$$

the initially populated S_2 state, an intermediate state, I, the S_1 state, and the ground state, S_0 . By simultaneously solving the four differential equations from the kinetic scheme in Equation 4.7 and applying appropriate boundary conditions, $S_2(t=0)=1$, the time dependence of the populations in each state are:

$$S_2(t) = e^{-k_1 t} \tag{4.8}$$

$$I(t) = -\frac{k_1\left(e^{-k_1 t} - e^{-k_2 t}\right)}{k_1 - k_2} \tag{4.9}$$

$$S_1(t) = \frac{K(t) k_1 k_2 e^{-t(k_1+k_2+k_3)}}{(k_1-k_2)(k_1-k_3)(k_2-k_3)} \tag{4.10}$$

$$K(t) = (k_1-k_2)e^{t(k_1+k_2)} + (k_3-k_1)e^{t(k_1+k_3)} + (k_2-k_3)e^{t(k_2+k_3)}$$

The absorption component of the transient-grating signal, $\mathrm{Re}\left[E_S^{(3)}(T)\right]$, can then be modeled as a function of the population time T as the products of transition-dipole strengths and populations as

$$\mathrm{Re}\left[E_S^{(3)}(T)\right] = \varepsilon_{A,S_2} S_2(T) + \varepsilon_{A,I} I(T) + \varepsilon_{A,S_1} S_1(T) \tag{4.11}$$

where $\varepsilon_{A,i}$ represents the net (PB+SE−ESA) transition-dipole strength of the i^{th} state (see Table 4.1).

The time profiles for the populations S_i as a function of the population time T are plotted in Figure 4.10. The initially populated S_2 state decays very rapidly (14 fs) to yield the intermediate I. The 142 fs time constant for the formation of the S_1 state results in a peak population of the intermediate I on the ~50-fs timescale. Assuming a constant PB contribution because all of the states in Equation 4.7 share the same ground state, S_0, the decay of the S_2 state to form the intermediate I is associated with a significant decrease in SE or an increase in ESA, or a combination. The negative transition-dipole strength of the S_1 state reflects a dominant $S_1 \rightarrow S_n$ ESA component; the SE component would be expected to be negligible owing to the extremely weak dipole strength for transitions to the S_0 state.

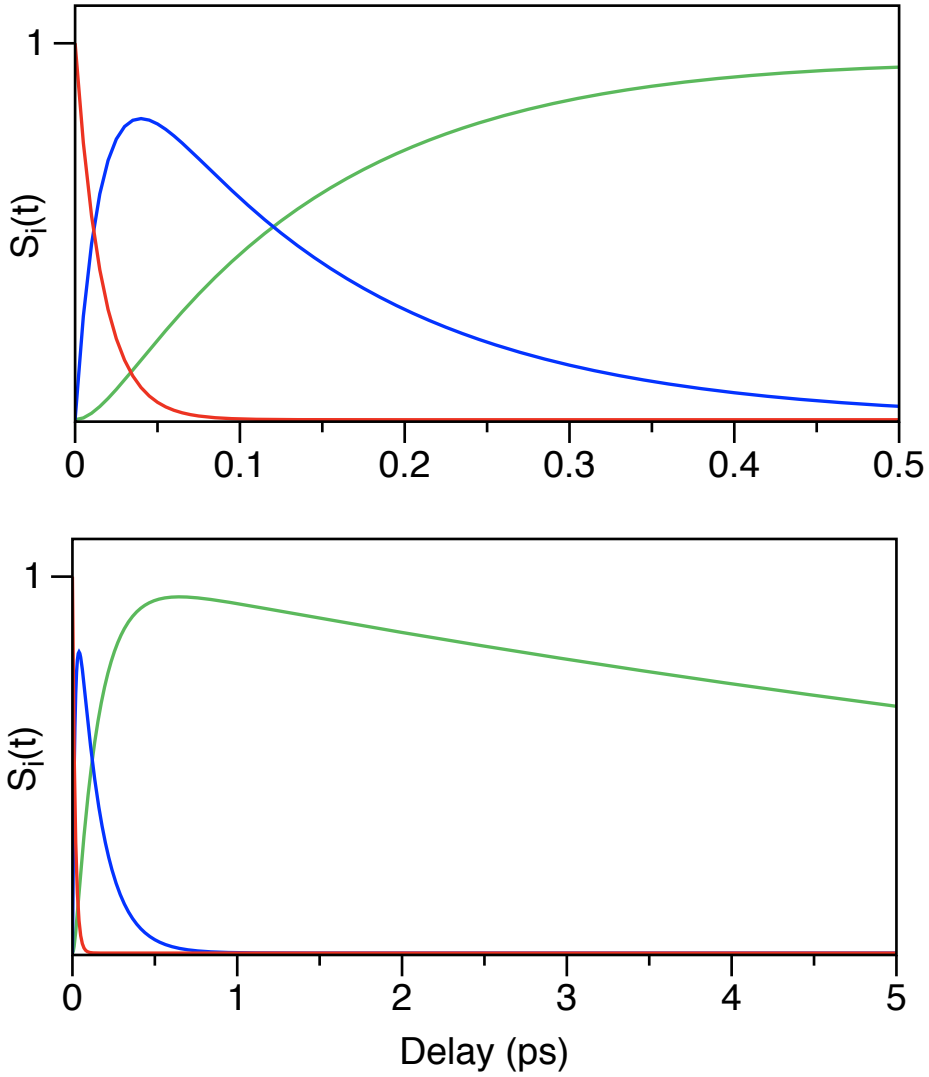

Figure 4.10. Time evolution of the populations S_i determined for a kinetic model consisting of a linear pathway of states (Equation 4.7) and models for the absorption and dispersion components of the β-carotene transient-grating signal in benzonitrile (Figures 4.6 and 4.7). The model parameters are listed in Table 4.1.

Table 4.1: Net transition-dipole strengths[a] at 520 nm contributing to the transient-grating signal for states and intermediates in the nonradiative decay of β-carotene in benzonitrile

State	τ [b]	$\varepsilon_{A,i}$	$\varepsilon_{D,i}$
S_2	16 fs	1	0.94
I	142 fs	0.54	0.51
S_1	9.8 ps	—	0.60
	11.5 ps	−0.22	—

a. See Equations 4.7, 4.11, 4.12 and the text. Positive $\varepsilon_{A,i}$ report $\mathrm{PB}+\mathrm{SE}>\mathrm{ESA}$; positive $\varepsilon_{D,i}$ report $\mathrm{ESA}>\mathrm{PB}+\mathrm{SE}$.

b. $\tau_i = 1/k_i$, see Equation 4.7.

The dispersion component from β-carotene, $\mathrm{Im}\left[E_S^{(3)}(T)\right]$, is shown in Figures 4.6 and 4.7 superimposed on a model that accounts for the contribution of the benzonitrile solvent. This model was constructed from a system-response function derived from the populations for the four states (Equations 4.8–4.10) weighted by transition-dipole strengths for each state, $\varepsilon_{\mathrm{D},i}$,

$$\mathrm{Im}\left[E_S^{(3)}(T)\right] = \varepsilon_{\mathrm{D},S_2}\mathrm{S}_2(t) + \varepsilon_{\mathrm{D,I}}\mathrm{I}(t) + \varepsilon_{\mathrm{D},S_1}\mathrm{S}_1(t) \tag{4.12}$$

as convoluted with the same Gaussian instrument response function used for the absorption component. Figure 4.11 compares the resulting model's time profile for the β-carotene dispersion component with that from neat benzonitrile. The dispersion transition-dipole strengths in Equation 4.12 were optimized so the residual (signal – model) shown in Figure 4.11b matched the shape of the dispersion signal of neat benzonitrile (Figure 4.11c). The model (solid line in Figure 4.11a) accordingly provides only an estimate for the dispersion component near time zero. At delays $T > 800$ fs, the dispersion component from β-carotene is modeled directly

because the contribution from the benzonitrile solvent is negligible. The positively signed dipole strengths for the S_2, I, and S_1 states for the dispersion component from β-carotene (Table 4.1) correspond to net ESA signal pathways; the strength of the ESA in the dispersion component decreases as S_1 accumulates. In contrast, the decay of the S_2 state to form the intermediate I is associated with decreasing SE or increasing ESA in the absorption component.

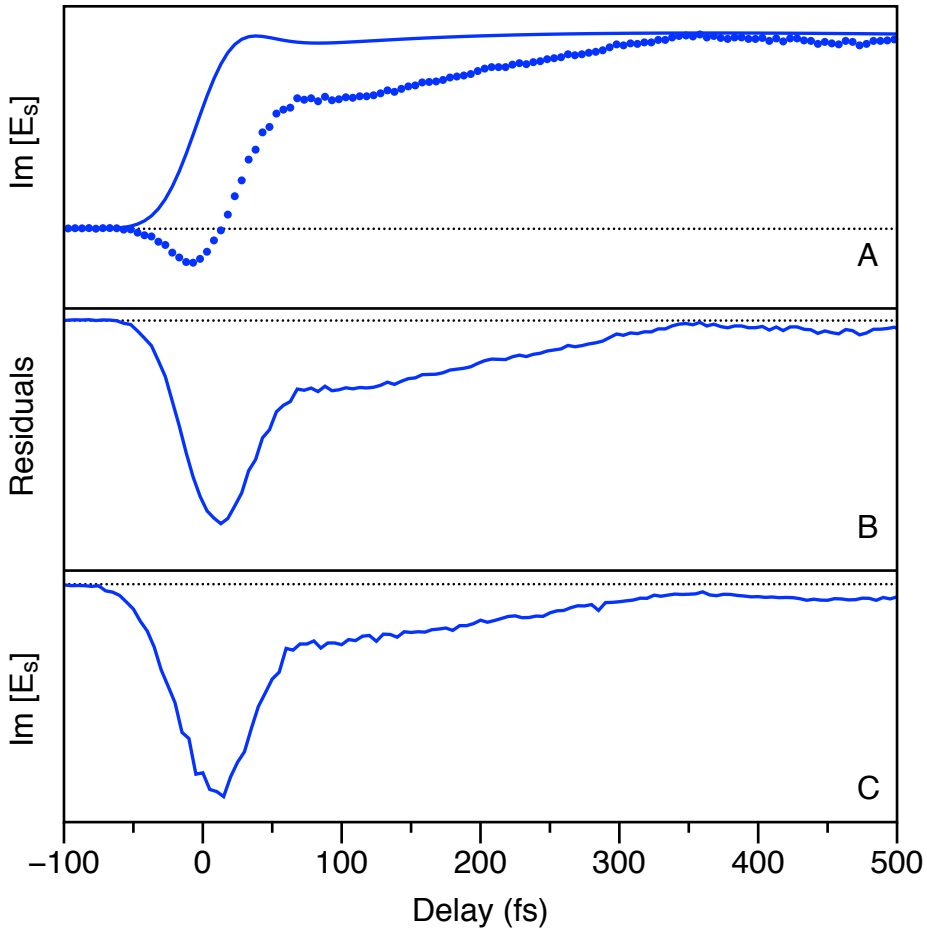

Figure 4.11. Comparison of the early-time dispersion components of the heterodyne transient-grating signals from β-carotene in benzonitrile and neat benzonitrile: (a) β-carotene dispersion component overlapped with an optimized kinetic model (solid line), as discussed in the text and Equations 4.7–4.12; (b) residual (signal – model); (c) dispersion component of the transient-grating signal from neat benzonitrile under the same measurement conditions.

The absorption and dispersion components of the β-carotene transient-grating signal describe the nonradiative decay of the S_1 state in terms of a single-exponential recovery with a ~10 ps time constant (see Figure 4.7). The observed time constants in the two components are significantly different; the absorption component decays with a 11.5 ps time constant, whereas the dispersion component exhibits a 9.8 ps time constant. These differences in relaxation timescale are consistent with the initial production of a hot (vibrationally excited or conformationally displaced) S_0 -state product from S_1 . These ground-state molecules would be expected to exhibit a photoinduced absorption spectrum that shifts to the blue and narrows as they relax (by vibrational cooling or conformational relaxation) on the picosecond timescale.[163]

Observations of photoinduced absorption from hot ground-state populations in carotenoids are made difficult by the overlapping SE and ESA signals to the red of the $S_0 \rightarrow S_2$ absorption spectrum.[9] In the heterodyne transient-grating studies of nonradiative decay in the torsionally active TPM dyes crystal violet and malachite green by Fleming and coworkers,[54,164] however, the dispersion component exhibits a shortened recovery lifetime compared to that of the absorption component when the laser is tuned to the red limit of the absorption spectrum. The timescales for the two components merge as the laser is tuned towards the center of the spectrum. Because the dispersion component has a broad wing (owing to the Kramers-Kronig relationship) on the red side of the absorption lineshape, the dispersion component is relatively insensitive to the blue shifting of the hot ground-state population's photoinduced absorption spectrum as relaxation occurs. Thus, the dispersion

component is primarily sensitive to the $S_1 \rightarrow S_0$ decay kinetics. The absorption component additionally senses the recovery of the initial vibrational distribution in the ground state. Thus, in β-carotene, the 9.8-ps dispersion recovery provides an estimate for the $S_1 \rightarrow S_0$ nonradiative decay timescale; the lengthening of the absorption recovery to 11.5 ps indicates cooling of the resulting hot ground state population on the ~2 ps timescale.

4.3.5 Wavelength-resolved Transient-grating Signals. Despite the limited spectral range afforded by the 40-fs, 520 nm pulses, the spectral information that is available in the transient-grating signal from β-carotene provides some important clues as to what is happening as population passes through the sequence of kinetic states (Equation 4.7) that recover the ground state. Figure 4.12 shows a contour representation of the wavelength-dispersed, absorption component of the transient-grating signal, as obtained directly from spectral interferometry; Figure 4.13 isolates several time-resolved spectra as slices of the delay *T*–wavelength–intensity surface.

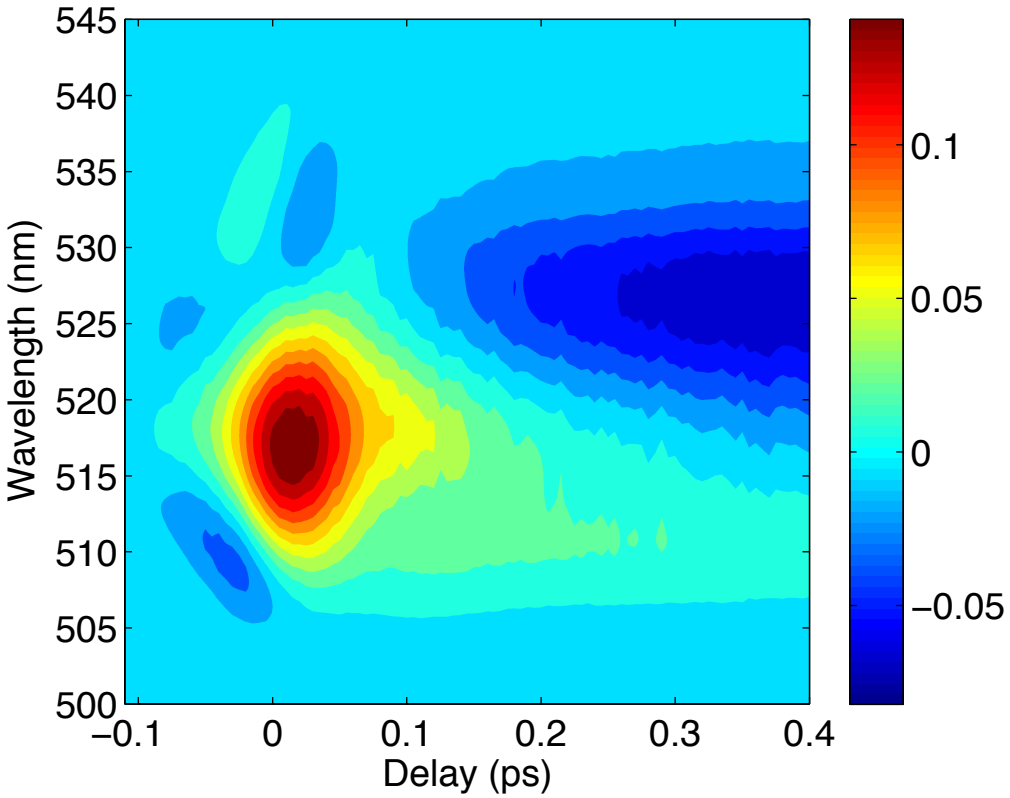

Figure 4.12. Contour representation (intensity as a function of probe pulse wavelength and delay *T*) of the absorption component of the transient-grating signal from β-carotene in benzonitrile.

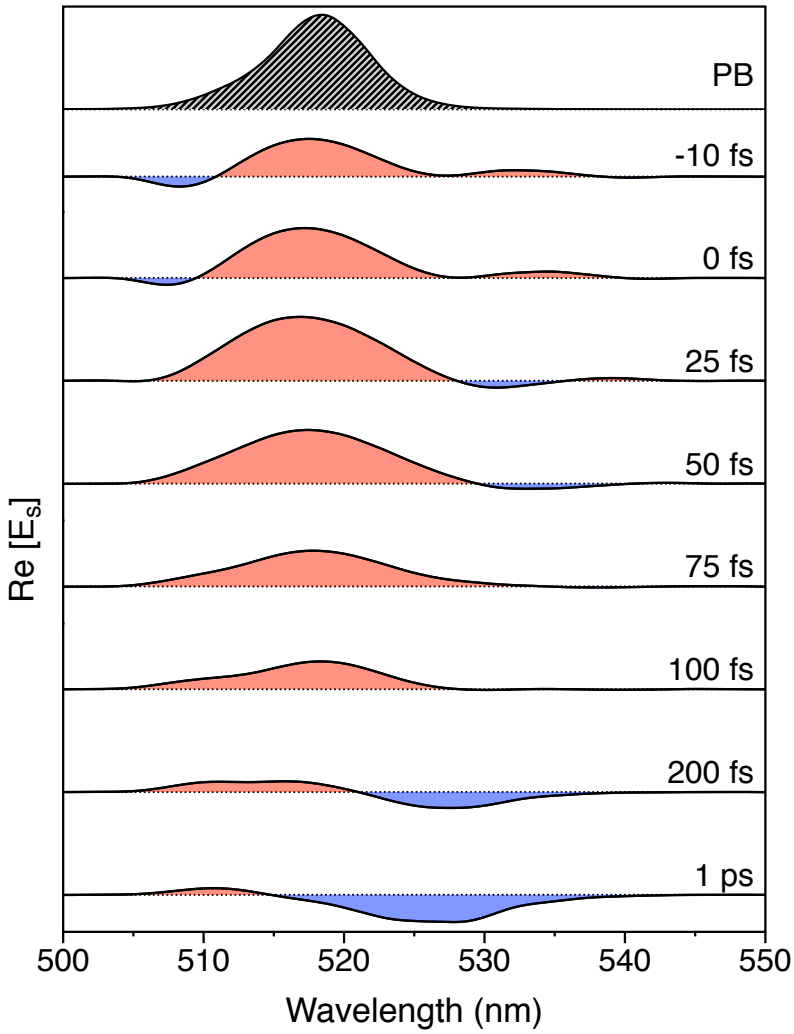

Figure 4.13. Time-resolved transient-grating absorption component spectra from β-carotene in benzonitrile at selected pump–probe delay times *T*. The top panel (PB) shows the instantaneous photobleaching spectrum, which was estimated as the product of the laser spectrum and the absorption spectrum of β-carotene (see Figure 4.3).

At delays $T < 200$ fs, the time-resolved spectra evolve during the kinetic timescales associated with the S_2 state and the intermediate I. With the assumption that the PB spectrum scales with the integral of the instrument response and that recovery of the ground state is insignificant, the spectral changes indicate that the SE contribution to the signal over the laser bandwidth is very short lived. Further,

as the sequence of states proceeds from the S_2 state to the S_1 state, the character of the ESA spectrum changes twice and overall tends to shift to the blue.

At early delays T (–10 and 0 fs) near the peak of the instrument-response function, the time-resolved spectra shown in Figure 4.13 include contributions from PB and SE lineshapes overlapped with a broad underlying ESA band arising from $S_2 \rightarrow S_{n,2}$ transitions.[32,165] The net PB + SE region is consistent in breadth and tuning with the instantaneous PB spectrum (Figure 4.13, top panel), as estimated from the product of the laser and linear absorption spectrum (Figure 4.3), rather than being consistent with the linear spectrum itself. This observation suggests that the ground-state absorption spectrum is at least inhomogeneously broadened and possibly heterogeneous owing to the presence of ground-state conformers.[36] The SE lineshape appears to be overlapped with a region of ESA just to the red of the instantaneous PB spectrum.

As the delay T increases subsequently, the SE signal shifts and eventually vanishes, and the initially present ESA signal is replaced by two distinct types of ESA signals. During the delay regime associated with the decay of the S_2 state and the rise of the intermediate I, $T \leq 25$ fs, the SE and the initial ESA signal are sharply attenuated as their spectra shift to the red and blue, respectively. The $T = 25$ fs and $T = 50$ fs spectra, the latter corresponding to the maximal population for the intermediate, include a new ESA region near 530 nm, to the red of the instantaneous PB peak, that broadens significantly and extends to the blue in the $T = 75$ fs and $T = 100$ fs spectra so that it spans and increasingly cancels the PB lineshape.

Finally, at longer delays, $T > 200$ fs, a distinct and more intense net ESA feature appears in the 520–535-nm range and shifts somewhat to the blue as the S_1 state is populated. This ESA band reaches a maximum intensity at $T = 1$ ps (see Figure 4.7a) and at this point largely extinguishes the PB peak.

4.4 Discussion

The experiments and results described in this contribution show that transient-grating spectroscopy with optical heterodyne detection obtains an improved description of the initial nonradiative decay dynamics of the S_2 state of β-carotene. The use of spectral interferometry in the detection scheme permits a clean isolation of the nonlinear optical signal from scattering and other background contributions that have previously hampered the interpretation of transient-grating signals at short pump–probe delay times.[32,54] The results provide additional support for the conclusion that a kinetic intermediate is produced on an ultrafast timescale (14 fs) after the resonant formation of the S_1 state (142 fs). These timescales are nearly in quantitative agreement with those determined previously by Cerullo *et al*. using transient-absorption spectroscopy.[30] The time-resolved transient-grating spectra, however, provide some new insight into the nature of the structural dynamics that occur during the radiationless decay pathway in terms of spectral dynamics and intensity changes in the SE and ESA parts of the signal. Further, a comparison of the absorption and dispersion components of the transient-grating signal provides information on the nature of the ensemble that returns to the ground state. The overall picture suggested by these results is that β-carotene undergoes an excited-

state structural evolution that likely involves relaxation towards a twisted conformation in the S_2 state. The dynamics involve crossing an activation-energy barrier that divides the minimum-energy path on the S_2-state potential-energy surface along bond-alternation and torsional coordinates. These motions are significant because they are likely to induce an intramolecular charge-transfer character.

The short timescale apparently associated with the formation of the kinetic intermediate state after resonant preparation of the S_2 state places significant limitations on the type of structural changes that are possible starting from the Franck–Condon (FC) geometry, prepared vertically from the equilibrium ground-state geometry. Koyama,[153,166] Cerullo,[30,37] and their coworkers assign the intermediate observed in β-carotene and other carotenoids to the S_x ($1B_u^-$) state, which was expected by Tavan and Schulten[149] below the S_2 state (Figure 4.1). The conclusion that the intermediate is the product of a nonradiative change of electronic state comes from the observation of a distinct ESA spectrum from that of the S_2 state, which would arise from probe-driven transitions to a different higher lying S_2 state because of a change in selection rules. In the case of the assignment to the S_x ($1B_u^-$) state, the suggestion is made that the intermediate evolves from a covalent state (+ pseudoparity) to an ionic state (− pseudoparity) with significant double excitation character.

The initial structural displacement indicated by resonance Raman spectroscopy for β- carotene and for most carotenoids is along the totally symmetric normal coordinates associated with C–C and C=C bond stretching coordinates. These are

the modes that appear in the ground-state vibrational coherence in homodyne transient-grating signals observed with very short pulses.[167-169] Because the formal bond order of the carbon–carbon bonds in the conjugated polyene backbone in carotenoids shifts from that of the ground state owing to the π (HOMO)→π* (LUMO) character of the $S_0 \rightarrow S_2$ excitation, these motions contribute to changes in bond-alternation character.[56,151]

Dynamics along the bond-alternation coordinates is implicated in short polyenes in the ultrafast changes in dipole strength that accompany transitions with adjacent dark states. As one important example, simulations by Levine and Martínez[152] describe how *trans*-2-butadiene undergoes a prompt displacement on the 10-fs timescale that results in a partitioning of the population prepared initially in the 1^1B_u state into the dark 2^1A_g state lying at somewhat lower energy. Torsional motions are subsequently activated that eventually lead to a twisted minimum-energy structure at a conical intersection (CI).

A similar sequence of events is obtained from the analysis by Olivucci, Robb, and coworkers[1,170-174] of the dynamics that lead to isomerization in cyanines and in protonated Schiff bases (PSBs). The potential-energy surfaces of long cyanines and PSBs differ from those of short cyanines and polyenes owing to the nature of the forces that act on the FC structure and the height of the barrier between the planar and twisted regions of the surface. As the conjugated length of the polyene increases, the height of the barrier increases; for ethylene, butadiene, and the cyanine 1144-C, the path from the FC structure to a CI at the 90° twisted geometry is considered barrierless.[83] Further, the shape of the potential energy surface changes

with the length of the conjugated region; with short polyenes, a monotonic descent to lower energy from the FC structure occurs along coupled bond-alternation and torsional coordinates. With longer conjugation lengths, the Franck-Condon structure is actually at a local minimum with respect to the torsional coordinates. The initial motions from the FC region are steeply along bond-alternation coordinates; the potential-energy gradient accelerates the system towards a planar minimum, where only a few vibrational periods occur before the torsional motions are launched. The torsions promote the crossing of the potential energy barrier that separates the planar minimum from a twisted region that exhibits a minimum at a CI. The fluorescence of cyanines and PSBs are largely quenched by crossing through the CI to recover the ground state, either with isomerization or by returning to the original minimum.

The present transient-grating results suggest that a similar picture (Figure 4.14) applies to the photophysics of β-carotene after resonant preparation of the S_2 state. The minimum-energy path on the β-carotene S_2 -state potential energy surface begins with displacements along the resonance-Raman active bond-alternation coordinates, as mentioned above. The clear signature of torsional motions[95,103] that lead from the planar (*trans*) minimum over the barrier towards a S_2 -state twisted minimum is detected in the time-resolved transient-grating spectra on the <25-fs timescale: the SE and ESA signals shift to the red and blue, respectively, in the spectra observed near the maximum of the instrument-response function. The SE shifts to the red because the energy gap between the S_2 -state and S_0 -state surfaces narrows as the torsional barrier is crossed especially because of the steepness of the

S_0 state surface towards its 90° torsional maximum. The ESA shifts to the blue after the barrier is crossed because the torsional side of the barrier is associated with an increase in the energy gap from S_2 to S_n; the barrier height and slope of the S_n surface is smaller than in the S_2 state owing to its increased π^* character. The SE and ESA contributions to the signal fade away very rapidly as the torsional motions begin owing to a breaking of symmetry.[103] In this picture, then, the intermediate I actually arises from the changes in the spectra of the SE and ESA signals due to the torsional motions. The 15-fs timescale would be the real time delay required to move from the FC structure along bond-alternation coordinates to the planar minimum and then to redistribute these motions along torsional coordinates so that the barrier is crossed.

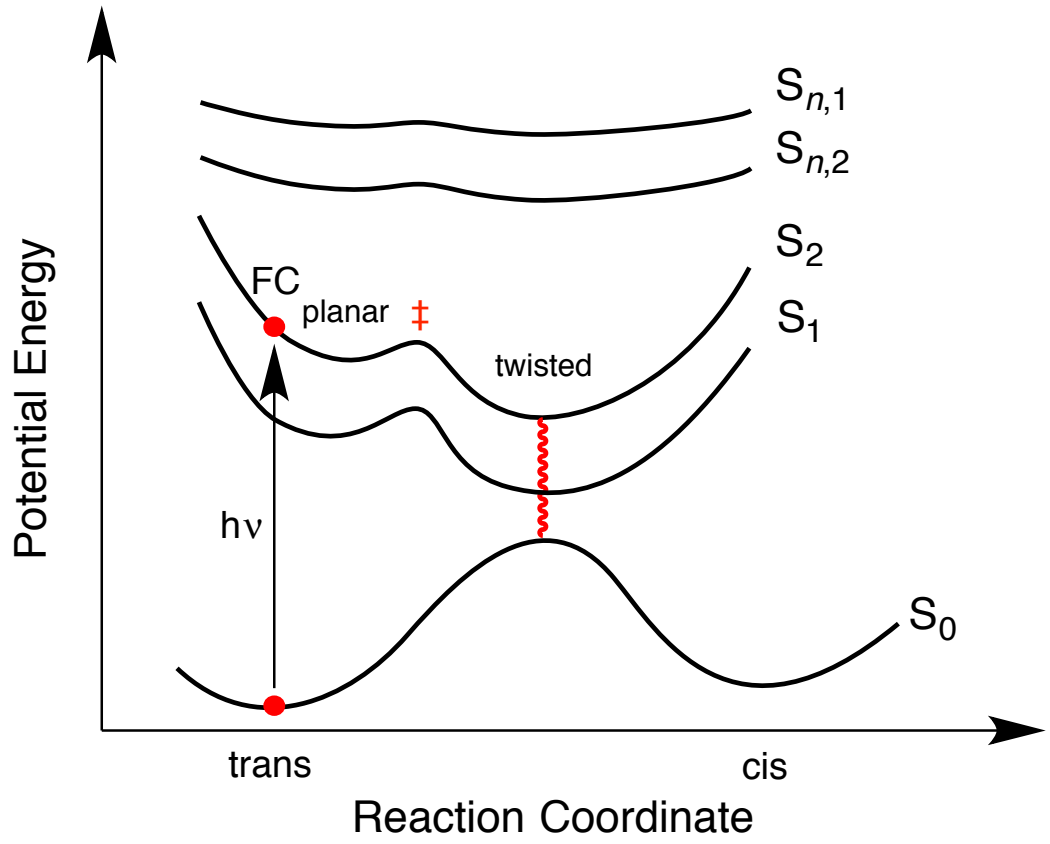

Figure 4.14. Potential-energy scheme for radiationless decay of β-carotene after optical preparation of the S_2 state involving sequential displacements along bond-alternation and torsional coordinates. The transition state (‡) marks the position along the reaction coordinate that divides the potential-energy curves between the planar region associated with the Franck–Condon (FC) structure and that along torsional coordinates leading to a twisted minimum-energy structure.

The second phase of the dynamics suggested in Figure 4.14 is associated with descent along torsional coordinates towards a twisted S_2 -state minimum. These dynamics are reported by the second phase of ESA spectral dynamics detected in the time-resolved transient-grating spectra. SE transitions during this second part of the response would be expected to the red of the laser's spectral bandwidth because the energy gap to the S_0 state continues to narrow as the system advances along the torsional coordinates. The onset of the distinct ESA lineshape to the red of the instantaneous PB spectrum (Figure 4.13, 25 fs and 50 fs spectra) marks the onset of

dipole strength to a different higher lying singlet state S_n that evidently accompanies the assumption of a twisted structure. The broadening of this ESA spectrum to the blue over the 50–100-fs timescale reports the spreading of the probability distribution near twisted minimum. Thus, the lifetime of the kinetic intermediate detected in the integrated transient-grating transients corresponds to the approach to the twisted minimum on the S_2 -state potential surface. The dynamics on this timescale are effectively associated with cooling of the system after it passes the transition-state barrier owing to relaxation along torsional coordinates. Note that apparent lifetime of the S_2 state of β-carotene obtained from Kerr-gate fluorescence transients[27,175] is consistent with the timescale of the intermediate detected in the present work, so the twisted conformation has significant dipole strength.

The motion along the second phase of response would be expected to be diffusive in character and strongly controlled by friction due to polar solvation dynamics. The impact of solvation is anticipated owing to the likelihood that an intramolecular charge-transfer (ICT) character is induced as the twisting proceeds. The ICT character arises in shorter polyenes owing to the proximity of ionic states at lower energy than covalent ("transoid") states in twisted polyenes and PSBs[55,150,152] and results in a distortion along out-of-plane coordinates from the twisted minimum towards a pyramidalized structure. In longer polyenes and carotenoids the formation of ICT character and a pyramidalized carbon atom might favor production of a local discontinuity or "kink" in the conjugated polyene backbone rather than a fully twisted conformation. The presence of an

intramolecular charge, as in the cyanines or PSBs, would enhance the formation of ICT character and lower the barrier between the planar and twisted regions of the potential-energy surface. Interaction of polar solvents with the induced ICT character near the twisted minimum damps the torsional motions in PSBs; simulations by Hynes and coworkers show that solvent friction increases the rate of radiationless decay from the region near the CI increases owing to suppression of trajectories on the excited-state surface that avoid surface crossing events.[56] This finding suggests strongly that the lifetime of the twisted S_2 -state structure in carotenoids would be shortened by an increase in the polarity of the surroundings.

In the context of the picture suggested in Figure 4.14, ground-state recovery would occur from near the twisted minimum of the S_1 state after it relaxes vibrationally. The strong ESA spectrum observed from the S_1 state exhibits a shift to the blue on the 500 fs timescale; this is consistent with the blue shifting of the ESA signal detected in previous two-color homodyne transient-grating studies.[176] The distinct timescales we observed in the recovery of the absorption and dispersion components of the integrated transient-grating signal then suggest that a hot S_0 -state ensemble would be initially formed upon nonradiative decay from the S_1 state. We assign the ~2 ps difference between the 10-ps recovery of the dispersion component and the 12-ps recovery of the absorption component to the relaxation along torsional coordinates to the original ground state.

These ideas raise a number of intriguing questions about how a light-harvesting protein might enhance its carotenoid–to-chlorophyll energy-transfer yield by favoring the assumption of a twisted conformation in the carotenoid's binding site.

The formation of ICT character and the mixing of the S_2 and S_1 states would be favored by twisting the carotenoid's conjugated polyene backbone.

A number of questions are raised by these experiments that require additional work, preferably with laser pulses with broader spectra. The observation of relatively narrow spectral features in the time-resolved transient-grating spectra suggests that the current results describe only the excited-state dynamics of the lowest-energy conformers of β-carotene in the ground-state ensemble.[36] This suggests the need to characterize the wavelength-dependent dynamics of this system, which might be most efficiently carried out in 2D experiments with broadband spectra.

CHAPTER 5

Excited-State Torsional Dynamics and Nonradiative Decay Intermediates from the S_2 State of Peridinin in Solution and in the Peridinin–Chlorophyll *a* Protein

5.0 Summary

The electric-field resolved femtosecond transient-grating spectroscopy presented in this work adds insight to the structural nature of this ICT state by comparing the transient-grating absorption spectra and kinetic profiles of peridinin in methanol and peridinin in the PCP protein. The integrated transient-grating kinetics for both systems suggest that an intermediate is formed following $S_0 \rightarrow S_2$ excitation on a ~30 fs timescale. The spectral signatures of this intermediate state that form on this ultrafast timescale for peridinin in methanol, however, appear to be present at all times for the case of peridinin in PCP. In addition, the decay profiles of the absorption and dispersion transient-grating signals suggest that decay of the S_1 in peridinin in methanol forms a displaced ground state relative to the absorbing state, while the decay of the S_1 state in the case of PCP forms the initial ground state. This is consistent with the picture of packing forces within the PCP protein distorting the planar geometry and constraining conformational dynamics of the peridinin chromophores. These observations lead to the suggestion that the nature of this intermediate in methanol is likely twisted or bent in character and that this conformationally displaced intermediate likely decays to a similarly

displaced S_1/ICT state consistent with the two-state two-mode theory by Olivucci.[1] We conclude that this distorted character of peridinin enforced by the protein binding sites of PCP may lead to an enhancement of the intramolecular charge-transfer character in the S_1 state, enabling more efficient energy transfer to Chl *a*.

5.1 Introduction

Carotenoids have diverse functions in photosynthetic systems including photoprotection and light harvesting,[3,6,9] but typically play a minor role in the latter due in large part to their symmetry properties and complex excited-state dynamics. Carotenoids absorb well in the mid-visible where the solar spectrum is the most intense, [147] but excitation energy transfer (EET) between carotenoids and chlorophylls (Chls) in many photosynthetic light harvesting proteins is inefficient owing to the short lifetime of the first resonant excited S_2 ($1\,B_u^+$) state, and the formally weak transition-dipole strength of the subsequent, non-radiatively-populated, dark S_1 ($2\,A_g^-$) state. In response to these shortcomings, light harvesting structures have evolved to minimize the distance between carotenoids and Chls and have evoked symmetry breaking via twisted and/or bent conformations within the photosynthetic apparatus.[8,9] The peridinin–chlorophyll *a* protein (PCP) from the dinoflaggelate *Amphidinium cartarae* (Figure 5.1) has unusually high carotenoid to Chl EET yields (> 90%) due, in part, to its use of peridinin as the sole carotenoid.

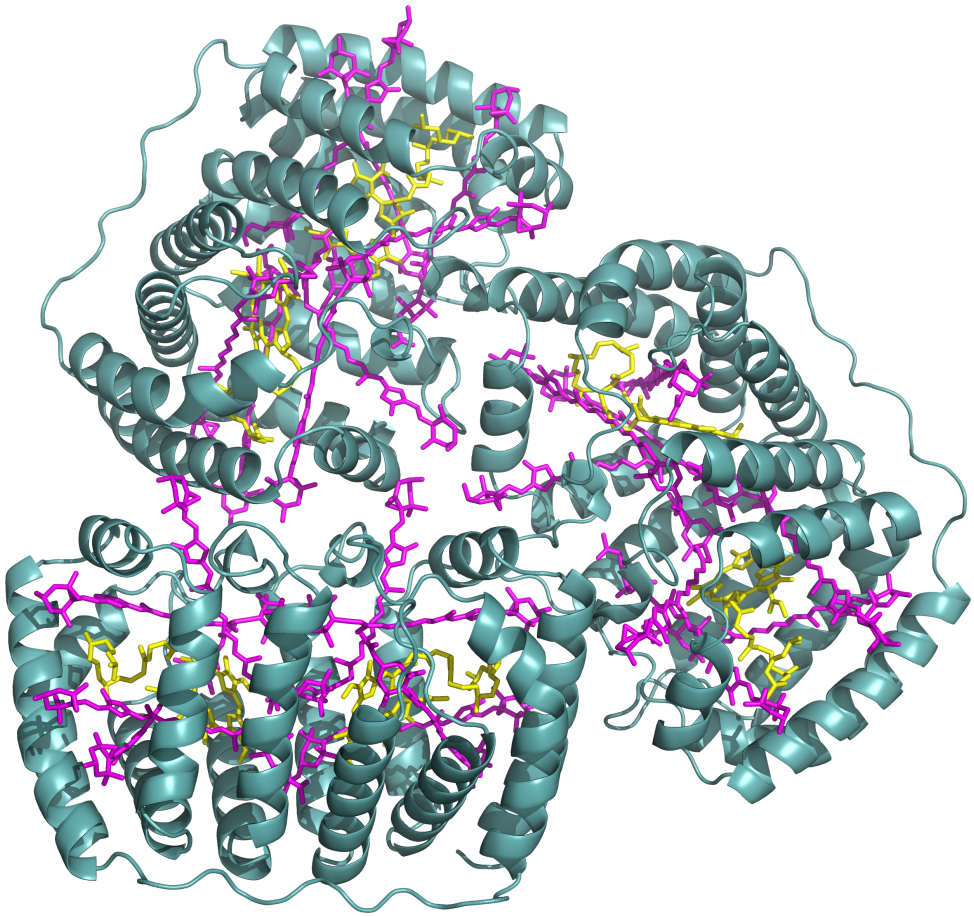

Figure 5.1. Structure of the trimeric peridinin–chlorophyll *a* protein (PCP) from *Amphidinium carterae* (1PPR.pdb) determined by Hofmann *et al*.[44]

Because the carotenoid S_2 state lies above that of the Q_x excited state of Chl or bacteriochlorophyll (BChl), $S_2 \rightarrow Q_x$ energy transfer via the Förster resonant dipole–dipole mechanism[177,178] is energetically favored. This pathway competes with $S_2 \rightarrow S_1$ nonradiative decay, however, so only a fraction of the total energy-transfer yield involves the S_2 state. The balance of energy transfer involves coupling of the carotenoid S_1 state to the Chl Q_y state. Given that there is very little dipole strength for the $S_1 \rightarrow S_0$ transition, one might expect that the yield of Förster energy transfer to the Chl Q_y state would be very small. This expectation prompts the suggestion of a Dexter-type, orbital-overlap, electron exchange-mediated energy-transfer

mechanism,[179] but calculations suggest that energy transfer by the dipole–dipole mechanism can still be more favorable in light-harvesting proteins[45,148,180]. As one example to compare with PCP, Fleming and coworkers[148] showed that 85% of the energy-transfer yield between a carotenoid, rhodopin glucoside, and BChl *a* in the B800–B820 system from *Rhodopseudomonas acidophila* occurs in ~90 fs via the S_2-state channel; only 15% of the yield goes through the S_1-state channel using the dipole-dipole mechanism despite the short distance to the BChl *a* acceptor. The total energy-transfer yield is only 70%. The S_1 state of rhodopin glucoside in this system has a relatively low dipole strength and a short lifetime, so energy transfer competes unfavorably with nonradiative decay of the S_1 state.[148] The peridinin–chlorophyll *a* protein (PCP), which serves as the peripheral light harvesting complex in the photosynthetic membranes of dinoflagellates, [181] however, has evolved specific structural adaptations such that the peridinin carotenoid acts as the primary light harvesting unit, efficiently transferring excitation to Chl *a* for subsequent long-range energy transfer to reaction centers. These adaptations include very tight packing of the peridinin carotenoids around the Chl *a* pigments to increase Förster energy transfer rates, and structural adaptations to the carotenoid itself to include an allene group and lactone ring in conjugation with the extended π-electron system of the polyene backbone (See Figure 5.2). These structures are thought to contribute to the intramolecular charge-transfer (ICT) character that leads to significantly enhanced energy-transfer coupling to Chl *a*.

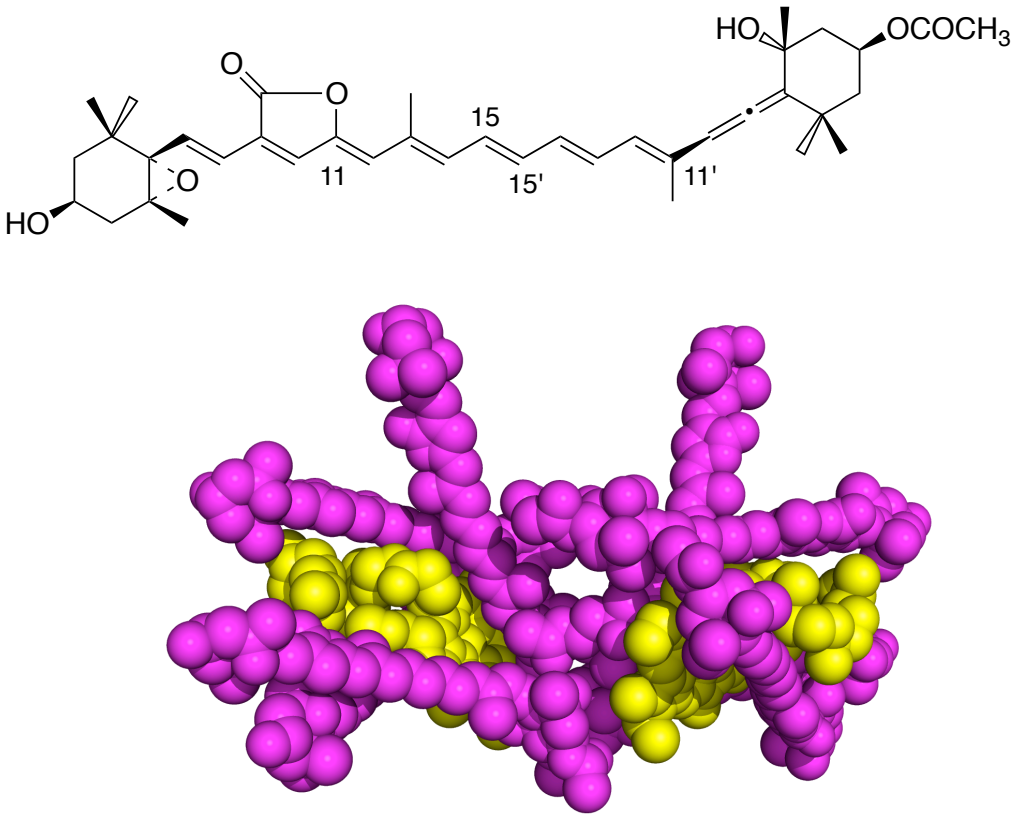

Figure 5.2. Structure of the peridinin carotenoid (top) and the arrangement of peridinin (magenta) and chlorophyll *a* (yellow) pigments in a single subunit of the peridinin–chlorophyll *a* protein (bottom).

Energy transfer from peridinin to Chl *a* in PCP occurs rapidly through two parallel channels: from the S_2 state to the Chl a Q_x state on the ~200-fs timescale and from the S_1 state to the Chl a Qy state in ~2.5 ps.[52] More than two-thirds of the energy transfer uses the S_1 state channel. The total quantum efficiency for energy transfer is 90 ± 5% allowing peridinin to efficiently utilize the green gap 460-570-nm region between the Chl *a* Soret and Q bands. As shown by Frank and coworkers, the lifetime of the lowest excited singlet state of peridinin is strongly dependent on the solvent environment.[182,183] The lifetime ranges from 7 ps in the highly polar solvent, trifluoroethanol, to 172 ps in two nonpolar solvents, cyclohexane and

benzene. The dynamics were found to be directly correlated with solvent polarity. The wavelengths of emission maxima, the quantum yields of fluorescence, and the transient absorption spectra were also affected by the solvent environment. This behavior is highly unusual for carotenoids; in general, the spectral properties and lifetimes of the S_1 state of carotenoids are independent of the solvent environment.

The solvent sensitivity of peridinin has been attributed by Frank and coworkers to the presence of an ICT state,[182,183] and this idea has been supported by both theoretical computations[184] and experiments on numerous other carbonyl-containing carotenoids and polyenals.[52,185-193] Owing to the ICT character, the energy transfer pathways in PCP are made much more sensitive to the reaction field arising from the polarity and polarizability of the surrounding protein and chromophore medium.[194-196] Despite these studies, how the ICT character develops in the S_1 state is not understood.

5.2 Experimental

5.2.1 Sample Preparation. The peridinin carotenoid was isolated from the marine alga, *Amphidinium carterae* (CCMP121), which were grown in the laboratory of Harry Franck using marine f/2-Si media.[197] The culture was incubated in a growth chamber illuminated with two 60 W incandescent light bulbs programmed for a diurnal light/dark cycle of 12 hours each. Cells were harvested during the logarithmic growth phase and collected by centrifugation at 4000 × g in a Sorvall RC-5B centrifuge. Packed cells were stored at −20°C until needed for the extraction of the pigments.

The algal cells were disrupted by adding 1 mL of acetone to an equal volume of thawed cells and gently shaking. Nine mL of a 1:1 mixture (v/v) of hexane (Fisher Scientific) and methyl *tert*-butyl ether (Fisher Scientific) were then added. The sample was transferred to 1.5 mL eppendorf tubes and centrifuged for 2 min at 13,600 × g using a bench-top microcentrifuge (Fisher Scientific, model no. 235C). The pigmented hyperphase of each tube was collected, combined, and dried under a gentle stream of nitrogen gas. The sample was then redissolved in 10 mL acetonitrile (Fisher Scientific) and small aliquots (~2 mL) were filtered through a Waters Sep-Pak 12cc C18 cartridge (catalog no. WAT036915) to remove the majority of chlorophyll. Samples were then concentrated down to ~2 mL by evaporation using a gentle stream of nitrogen gas and stored in acetonitrile at −20°C until further use.

Prior to use in the spectroscopic experiments, peridinin was purified by high-performance liquid chromatography (HPLC) using a Waters 600E/600S multisolvent delivery system equipped with a 2996 photodiode array detector as described previously.[157] The column was a Waters Atlantis Prep T3 OBD 5 μm column (19 x 100 mm). Acetonitrile was delivered isocratically at a flow rate of 7.0 mL/min. Samples collected from the HPLC were dried under nitrogen gas and stored at -20°C until further use.

Peridinin-chlorophyll protein (PCP) was isolated as previously described[198] from an *Amphidinium carterae* culture provided by Dr. Roger Hiller.

5.2.2 Linear Spectroscopy. Absorption spectra were acquired with a Hitachi U-4001 spectrophotometer (2 nm bandpass). Continuous wave absorption spectra of

peridinin in methanol and PCP in trcine buffer (50 mM tricine, 20 mM KCl pH = 7.5) superimposed with the excitation laser spectrum are shown in Figure 5.3.

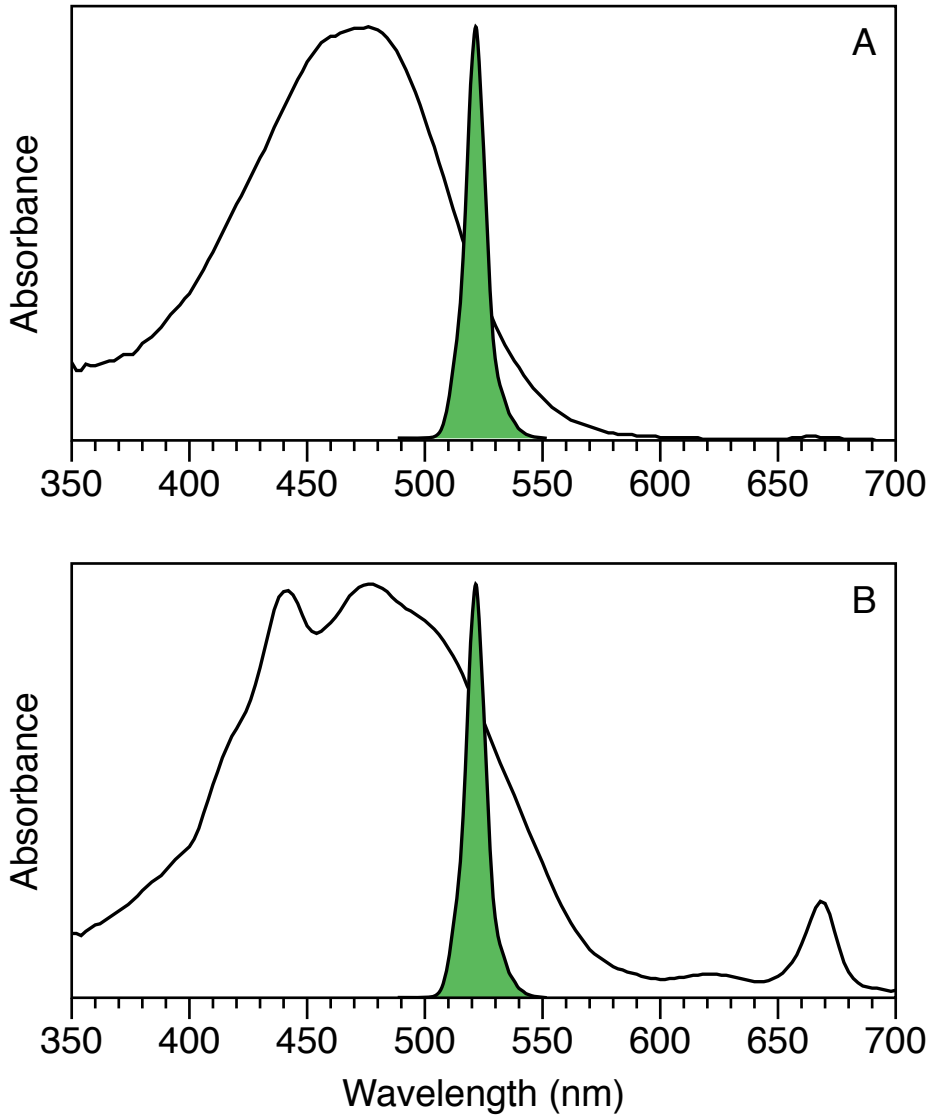

Figure 5.3. Room-temperature absorption spectra of (a) peridinin in methanol and (b) PCP in tricine/KCl buffer. Superimposed is the output spectrum of the 40 fs OPA signal beam (519-nm center wavelength), as tuned for the heterodyne transient-grating experiments.

5.2.3 Nonlinear Spectroscopy. The photon-echo instrumentation and methods are identical to was is reported in **Section 4.2.3** of this dissertation.

5.3 Results

5.3.1 Linear Spectra. Figure 5.3 shows the linear absorption spectrum at 22 °C for peridinin in methanol and PCP in tricine buffer (50 mM tricine, 20 mM KCl, pH = 7.5) respectively. For the transient-grating experiments discussed here, the spectrum of the OPA's signal output was tuned to overlap with the onset of the S_0 ($1A_g^-$)→S_2 ($1B_u^+$) absorption spectrum. The laser spectrum has a full-width at half maximum (FWHM) intensity of ~8 nm, and its intensity spans a 505-542 nm probe region from baseline to baseline.

5.3.2 Peridinin in Methanol Transient-grating Signals. The absorption and dispersion components of the integrated transient-grating signal of peridinin in methanol (Figure 5.4) are similar in character to that of our previous work on β-carotene in benzonitrile (**Section 4.3.3**). The peridinin absorption signal exhibits an instrument response-limited rise followed by an ultrafast, multi-exponential decay with timescales of 31 and 615 fs, where the signal is dominated by ESA by 50 fs. The ESA builds in intensity to maximum near 1.2 ps where the signal decays to baseline on a 11 ps timescale. In contrast, β-carotene exhibited faster initial decay timescales of 15 and 140 fs and a slower rise due to the ESA component with a timescale of 9.8 ps.

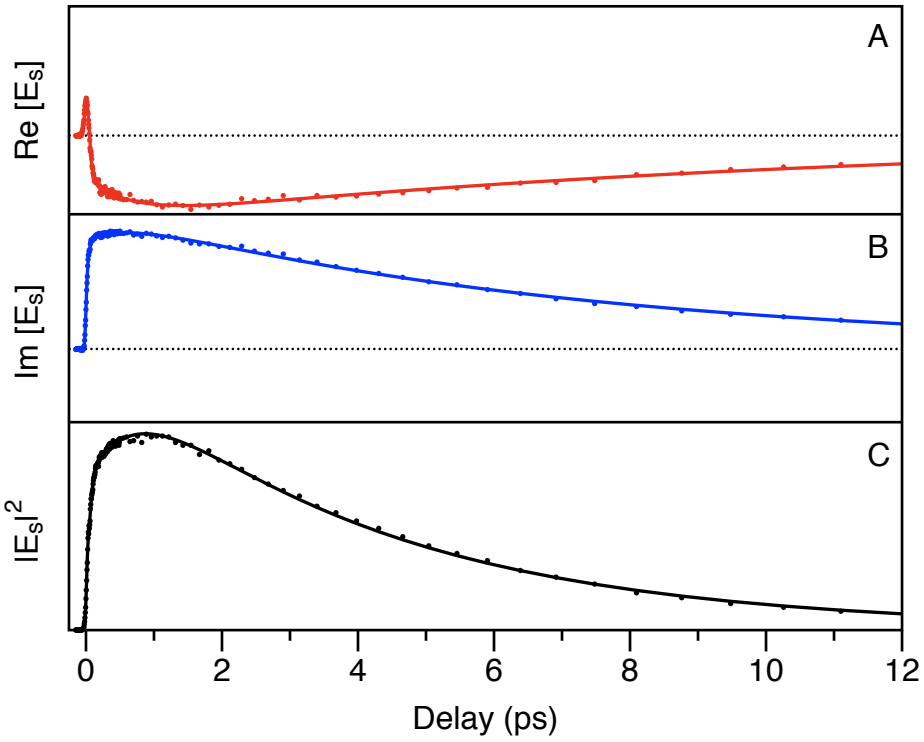

Figure 5.4. Spectrally-integrated transient-grating signals from peridinin in methanol at room temperature: (a) absorption component; (b) dispersion component; (c) the complex modulus. In (a) and (b) the data points are superimposed with kinetic models (solid line). The complex modulus (c) was calculated directly from the sum of the squares of the data points in (a) and (b).

The dispersion component signal of peridinin in methanol (Figure 5.4b) exhibits an instrument response-limited rise that appears to be delayed by about 30 fs with respect to the absorption component signal. This is followed by a multi-exponential rise with timescales corresponding to the decay of the absorption component signal, reaching a maximum near 800 fs. The subsequent decay of the dispersion component signal to baseline occurs on the 7 ps timescale, which is shorter than the corresponding decay of the absorption component signal. This is similar to the result obtained from our earlier work with β-carotene, where the difference in the longest decay timescales of the absorption and dispersion component were

attributed to vibrational cooling on the ground-state potential in accordance with observations made by Xu and Fleming using heterodyne transient-grating spectroscopy on crystal violet and malachite green.[54]

Figure 5.4c shows the modulus signal, which is the sum of the squared absorption and dispersion signals which detect only the amplitude of the electric field and is analogous to the homodyne signal as measured with a conventional square-law detector. The modulus squared signal shows an instrument response-limited rise followed by a multi-exponential rise to a maximum near 800 fs and a subsequent decay to baseline. This signal shows a smooth, monotonic rise as the population time approaches 1 ps in contrast to our previous work on β-carotene in benzonitrile, which exhibited a peak near time zero due to the relatively strong nonresonant contribution form benzonitrile.

5.3.3 Peridinin–chlorophyll *a* Protein Transient-grating Signals. The absorption component of the PCP signal (Figure 5.5a) shows similar kinetic behavior to peridinin in methanol, but with additional complexity due to population transfer from peridinin to chlorophyll *a* in the PCP protein. The peridinin in PCP absorption component signal exhibits an instrument response-limited rise followed by a multi-exponential decay similar to that of peridinin in methanol. The first two decay components are perhaps slightly faster in peridinin in PCP than peridinin in methanol (27 vs. 31 fs and 565 vs. 615 fs), while the rise to baseline due to decay of the ESA component is markedly slower in PCP than peridinin in methanol (16 vs 11 ps). This 16 ps decay of the ESA of the absorption signal of peridinin in PCP is consistent with the previously measured S_1 lifetime of peridinin in PCP.[52]

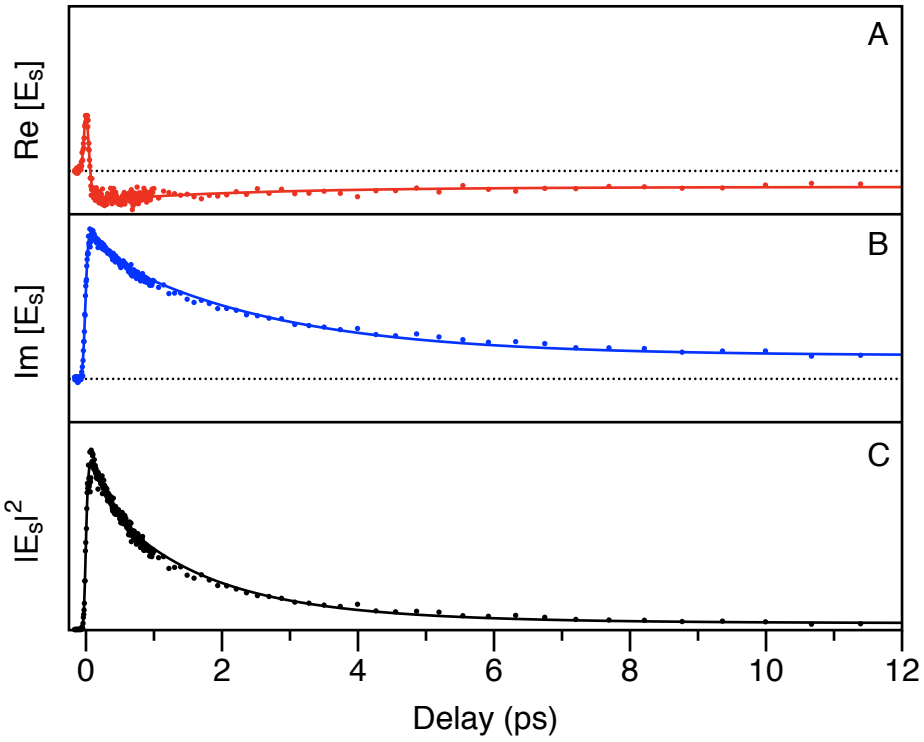

Figure 5.5. Spectrally-integrated transient-grating signals from the peridinin–chlorophyll *a* protein in a tricine/KCl buffer at room temperature: (a) absorption component; (b) dispersion component; (c) the complex modulus. In (a) and (b) the data points are superimposed with kinetic models (solid line). The complex modulus (c) was calculated directly from the sum of the squares of the data points in (a) and (b).

The dispersion signal (Figure 5.5b) shows an instrument response-limited rise coinciding with the rise of the absorption signal, whereas in peridinin in methanol there was a delayed rise relative to the absorption signal. The rise of the peridinin in PCP signal reaches its maximum near the peak of the integrated instrument response function, where the peridinin in methanol signal rises to a peak near 800 fs because of the loss of excited-state population due to energy transfer to chlorophyll *a*. Interestingly, the longest-timescale decay component in the dispersion signal (16 ps) is the same as in the absorption signal. This suggests that vibrational cooling is not occurring on the peridinin ground state potential, unlike

β-carotene and peridinin in solution. The modulus squared signal has a similar shape to the dispersion signal, but decays more quickly with larger amplitudes at early time, again due to the energy-transfer pathways open to peridinin in PCP.

5.3.4 Solvent Contributions to Transient-grating Signals. In our previous transient-grating study of β-carotene in benzonitrile, the early-time dispersion data was contaminated with a large, negative-pointing solvent signal, while the absorption signal timescales remained unaffected. This large birefringent contribution apparent in the dispersion signal can be attributed to the relatively large electronic hyperpolarizability of benzonitrile.[154] The measured signal intensities of neat methanol and water in our experiments were approximately five times less that of benzonitrile. While using similar optical densities of peridinin in methanol and PCP in tricine buffer in these experiments compared to our previous work on β-carotene, this reduction of the solvent signal strength produced dispersion signals with no apparent negative-pointing solvent contribution. As a result of this inner filter effect,[154] the dispersion signals of peridinin in methanol and PCP in tricine buffer are modeled directly.

5.3.5 Modeling of the Peridinin in Methanol Transient-grating Signal. In Figures 5.4 and 5.5, the integrated transient-grating signals of peridinin in methanol are shown superimposed with a model obtained from the convolution of a system response function and a Gaussian-shaped instrument response function. The instrument response function was obtained by measuring a transient-grating signal from neat methanol. The simplest response function consistent with the decay profile of the absorption component consists of the sum of three exponentials. After

nonlinear least-squares optimization using iterative reconvoltion, the optimized system response function consists of two decay components with timescales of 31 and 615 fs, and a rising component with a 7 ps time constant (see Table 5.1).

Similar to β-carotene, the simplest kinetic model consistent with this response is a linear sequence of four states:

$$S_2 \xrightarrow{k_1} I \xrightarrow{k_2} S_1 \xrightarrow{k_3} S_0 \tag{5.1}$$

the initially populated S_2 state, an intermediate state (I), the S_1 state, and the ground state, S_0. The absorption and dispersion signals of peridinin in methanol are modeled similar to that of β-carotene shown in **Section 4.3.4** of this dissertation. The time-evolution for the S_i states as a function of the population time *T* are plotted in Figure 5.6 (solid lines). As seen from the absorption signal, the initially populated S_2 state rapidly decays with a time-constant of 31 fs to the intermediate state, I. The I state decays into the S_1 state with a time constant of 615 fs. The decay of S_1 state occurs on the 11 ps timescale for the absorption component signal. The time constants for the S_2 and I states are the same for the dispersion component as the absorption component, while time constant for the decay of the S_1 state in the dispersion component signal is markedly faster at 7 ps. The state lifetimes and transition-dipole strengths for the absorption and dispersion components of the integrated transient-grating signals are shown in Table 5.1.

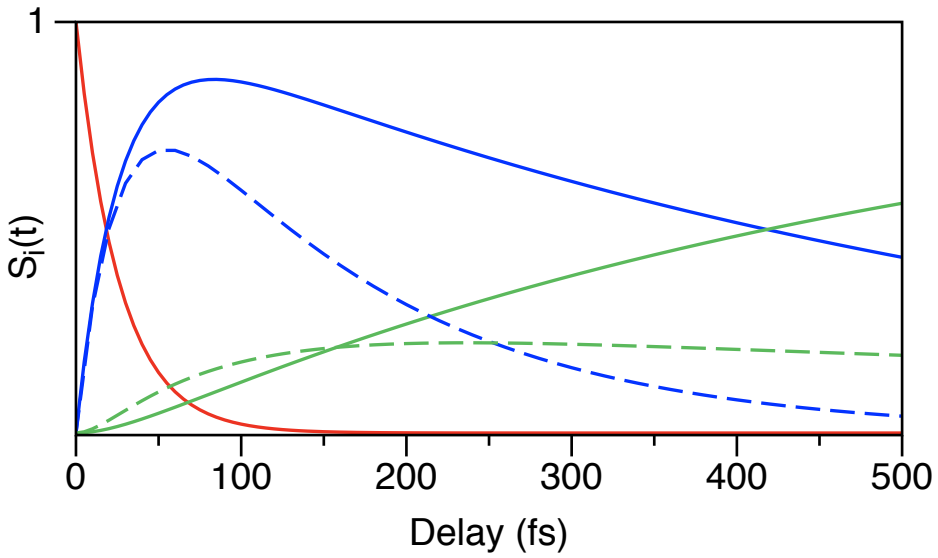

Figure 5.6. Time evolution of the populations S_i for the S_2 state (red), the I state (blue), and the S_1 state (green) as determined from kinetic modeling of integrated transient-grating absorption signals of peridinin in methanol (solid lines) and the peridinin–chlorophyll *a* protein (PCP) in solution (dashed lines). The peridinin state-populations arise from the linear kinetic model in Equation 5.1 (see $S_i(t)$ functions in Equations 4.8–4.10) using the timescales for each state as shown in Table 5.1. The PCP state-populations arise from the branched kinetic model in Equation 5.2 using the timescales in Table 5.2. The initial population of the S2 state is set to one ($S_2(0)=1$) and all other initial populations are set to zero for peridinin and PCP. Note: the S_2 state kinetics (red) for peridinin and PCP are indistinguishable.

Table 5.1: Net transition-dipole strengths[a] at 520 nm contributing to the transient-grating signal for states and intermediates in the nonradiative decay of peridinin in methanol

State	τ [b]	$\varepsilon_{A,i}$	$\varepsilon_{D,i}$
S_2	31 fs	1	0.28
I	615 fs	–0.21	0.54
S_1	7.0 ps	—	0.62
	11 ps	–0.41	—

a. See Equations 4.7, 4.11, 4.12 and the text (**Section 4.3.4**). Positive $\varepsilon_{A,i}$ report PB + SE > ESA ; positive $\varepsilon_{D,i}$ report ESA > PB + SE .

b. $\tau_i = 1/k_i$, see Equation 5.1.

5.3.6 Modeling of the Peridinin–chlorophyll *a* Transient-grating Signal. Similar to peridinin, PCP is modeled as the convolution of an instrument response function and a system response function. The optimized system response function for the absorption component consists of two decay components with timescales of 27 and 564 fs and a rising component on the 16 ps timescale. The kinetics of the PCP system are modeled similar to peridinin as:

$$S_2 \xrightarrow{k_1} I \xrightarrow{k_2} S_1 \xrightarrow{k_3} S_0 \tag{5.2a}$$

$$I \xrightarrow{k_x} Q_x \tag{5.2b}$$

$$S_1 \xrightarrow{k_y} Q_y \tag{5.2c}$$

but with the additional branching deactivation pathways due to energy transfer from the I and S_1 states of peridinin to the Q_x and Q_y states of Chl *a* (Equations 5.2b and 5.2c) respectively. Energy transfer from the S_2 state was ignored in our model due to its extremely short lifetime (< 30 fs). The timescales used in our model corresponding to k_3, k_x, and k_y were obtained from literature values for the decay of the S_1 state of peridinin in PCP (16 ps)[52], and the energy transfer rates of peridinin to the Q_x (200 fs) and Q_y (3 ps) of Chl *a* in PCP respectively.[52] By solving the simultaneous differential rate equations corresponding to Equation 5.2 using the same boundary conditions as peridinin, the populations for the S_i states were obtained and the results are plotted in Figure 5.6 (functions not shown). Similar to peridinin, the absorption and dispersion component signals from PCP are modeled

by Equations 4.11 and 4.12 respectively, only with the population functions obtained as stated above. The kinetic models for the PCP transient-grating signals are shown as dotted lines in Figure 5.6. The absorption and dispersion component signals are modeled well using the global timescales of 27 fs for the ultrafast decay of the S_2 state, 564 fs for the decay of the I state, and 16 ps for the decay of the S_1 state (see Table 5.2). It should be noted that in the case of peridinin in PCP, the long-time data can be modeled with a common decay component of 16 ps for the absorption and dispersion components, whereas with peridinin in methanol, two timescales of 11 and 7 ps are needed to model the absorption and dispersion components.

Table 5.2: Net transition-dipole strengths[a] at 520 nm contributing to the transient-grating signal for states and intermediates in the nonradiative decay of the PCP protein in solution.

State	τ[b]	$\varepsilon_{A,i}$	$\varepsilon_{D,i}$
S_2	27 fs	1	0.35
I[c]	564 fs	–0.04	0.54
S_1[d]	16 ps	–0.20	1.56

a. See Equations 4.7, 4.11, 4.12 and the text (**Section 4.3.4**). Positive $\varepsilon_{A,i}$ report $\mathrm{PB+SE > ESA}$; positive $\varepsilon_{D,i}$ report $\mathrm{ESA > PB+SE}$.
b. $\tau_i = 1/k_i$, see Equation 5.1.
c. I is quenched by Q_x with a timescale of 200 fs.[52]
d. S_1 is quenched by Q_y with a timescale of 3 ps.[52]

5.3.7 Wavelength-resolved Transient-grating Signals of Peridinin in Methanol. Figure 5.7a shows a contour representation of the early-time transient-grating absorption spectra from peridinin in methanol. The contour map shows an instrument response-limited rise of a $\mathrm{PB+SE}$ feature near the peak of the excitation

spectrum (519 nm) as the S_2 state is populated, which rapidly broadens and decays to baseline before 200 fs. An ESA feature begins to form near the zero of time, centered near 525 nm as the I state is populated from the S_2 state, and increases in intensity beyond the time-window shown in Figure 5.7.

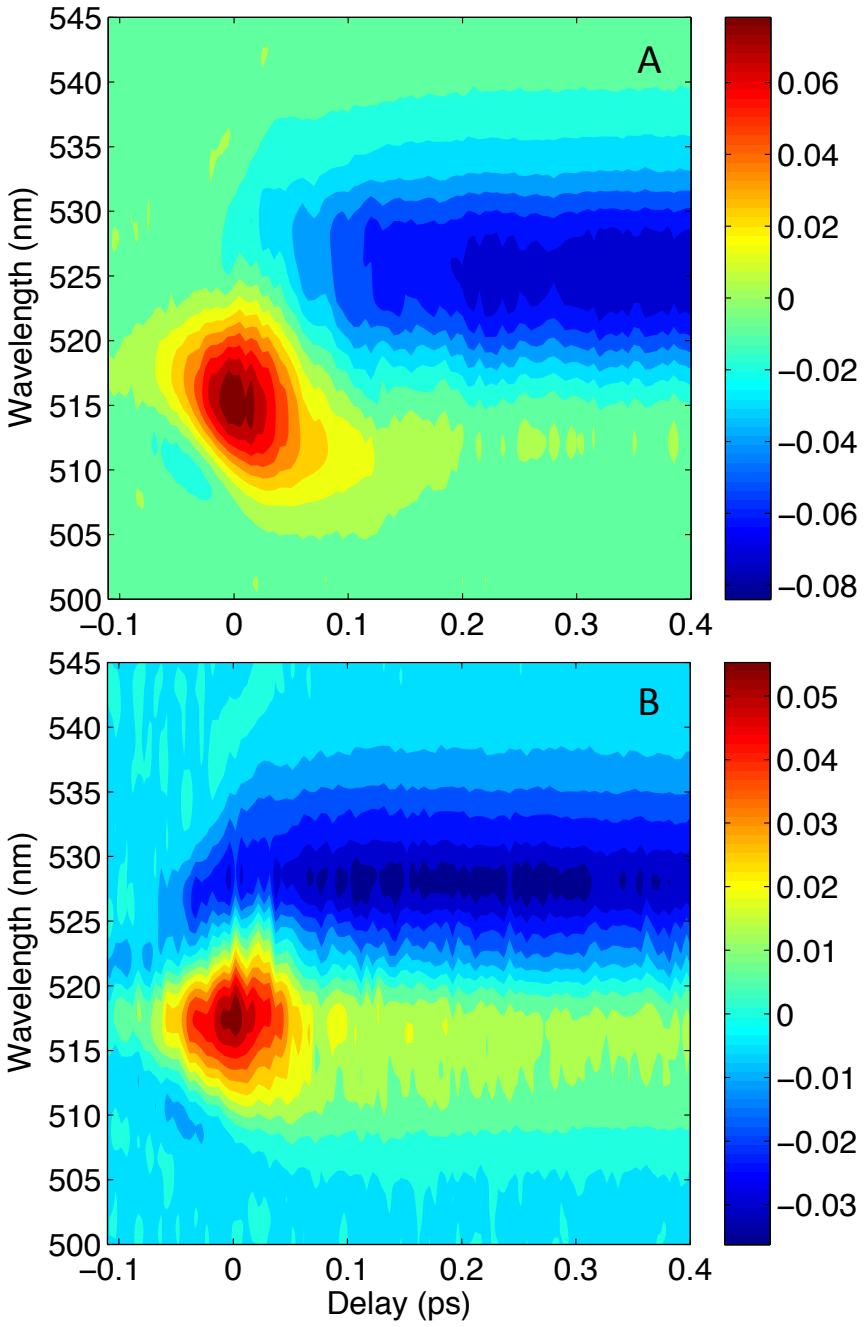

Figure 5.7. Contour representation (intensity as a function of probe pulse wavelength and delay *T*) of the absorption component of the transient-grating signal from (a) peridinin in methanol and (b) the peridinin–chlorophyll *a* protein in solution. The figures contain 15 linearly spaced contours between the minimum and maximum intensity values of the respective data sets.

Figure 5.8 shows transient spectra of the same data shown in contour map (Figure 5.7a). The top panel in Figure 5.8 shows the photobleaching spectrum (PB), which was calculated as the product of the excitation spectrum and the linear peridinin absorption spectrum. Similar to the contour representation, the early-time spectra (Figure 5.8, –10 fs) show a narrow PB peak near 515 nm with low amplitude ESA-dominated regions to the blue and red of the PB feature. The ESA feature to the blue is nearly gone by 0 fs as the I state population begins to dominate. The ESA feature to the red grows in intensity to dominate the entire measured spectrum by 200 fs. The spectral dynamics are complete by approximately 1 ps, where subsequent spectra merely decay in intensity due to non-radiative decay of the S_1 state.

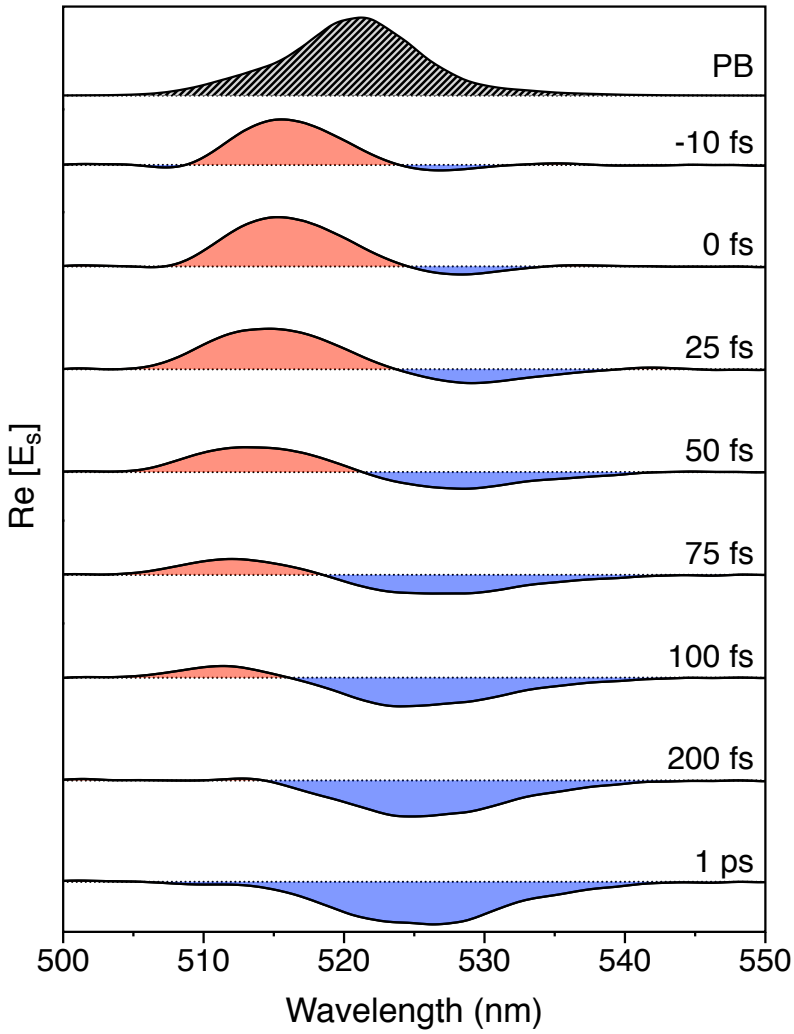

Figure 5.8. Time-resolved transient-grating absorption component spectra from peridinin in methanol at selected population times *T*. The top panel (PB) shows the instantaneous photobleaching spectrum, which was estimated as the product of the laser spectrum and the absorption spectrum of peridinin in methanol (see Figure 5.3a). These spectra come from the same data in the contour plot shown in Figure 5.7a.

5.3.8 Wavelength-resolved Transient-grating Signals of the Peridinin–chlorophyll *a* Protein. Figure 5.7b shows a contour representation of the early-time PCP transient-grating absorption spectra. The early-time (<0 fs) data show a rising PB+SE component centered near 516 nm coinciding with the appearance of a negative ESA signal centered near 527 nm. Most of the initial PB+SE feature near

517 nm decays by 75 fs, leaving about 20% of the amplitude to decay on the ~16 ps timescale. The ESA feature continues to build to a maximum intensity near 500 fs and decays with the time-constant of the S_1 state. Figure 5.9 shows the transient-grating spectra of the same data shown in the contour map (Figure 5.7b). The early-time transient-grating spectra (Figure 5.9, –10 fs) show a narrow PB+SE feature centered near 517 nm with a very weak ESA feature to the blue, and a stronger ESA feature to the red. The PB+SE feature broadens and decays monotonically, while the ESA feature builds to a maximum near 600 fs, and decays on the timescale of the S_1 state lifetime.

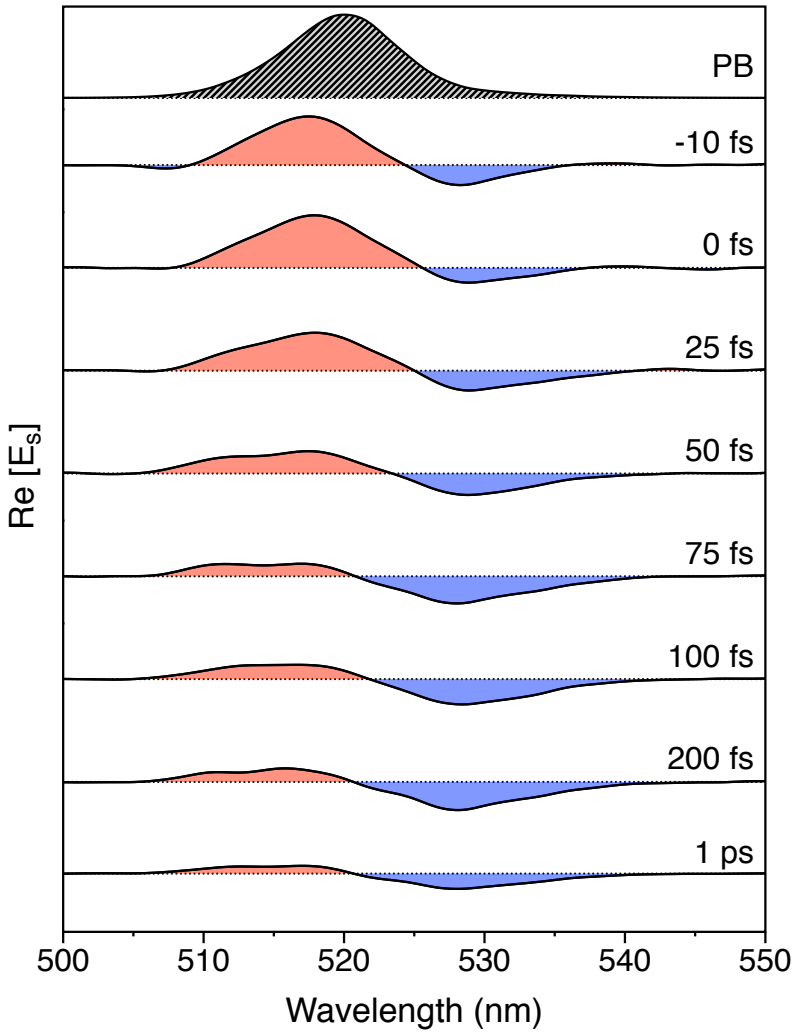

Figure 5.9. Time-resolved transient-grating absorption component spectra from peridinin–chlorophyll a protein (PCP) in solution at selected population times *T*. The top panel (PB) shows the instantaneous photobleaching spectrum, which was estimated as the product of the laser spectrum and the absorption spectrum of PCP (see Figure 5.3b). These spectra come from the same data in the contour plot shown in Figure 5.7b.

5.4 Discussion

In this contribution, the integrated heterodyne transient-grating signals of peridinin in methanol and peridinin in the peridinin–chlorophyll *a* protein reveal divergent kinetics of their associated absorption and dispersion signals and starkly different time-evolution of the transient-grating absorption spectra. Even

considering the limited excitation laser bandwidth, the transient-grating spectra provide insight toward a structural assignment of the ICT state. In addition, our modulus squared ("homodyne") transient-grating signals lack the large, zero-time spike and the associated large amplitude decay that is present in previous four-wave-mixing signals from peridinin in solution and in PCP,[51] and further, the separation of the absorption and dispersion signals allow observation of the ultrafast dynamics apparent in the absorption signal of peridinin that is obscured during the relatively slow rise of the modulus squared signal.

The integrated transient-grating signals provide a kinetic outline for the timescales of the nonradiative decay pathways occurring in peridinin in methanol and PCP. The integrated transient-grating absorption-component signal of peridinin in methanol exhibits an instrument response-limited rise as the PB + SE -dominated S_2 state is populated followed by a subsequent multi-exponential decay into a ESA-dominated time-region. The decays with time-constants of 31 and 615 fs (see Table 5.1) correspond to the simultaneous loss of stimulated emission as nonradiative decay transfers population away from the strongly dipole allowed S_2 state and a dramatic gain in ESA as the $I \rightarrow S_n$ and $S_1 \rightarrow S_n$ pathways are driven by the excitation spectrum. This can be understood best considering, again, the two-state, two-mode picture developed by Olivucci.[1] The ultrafast departure of the system from the Franck–Condon geometry initially along Raman-active bond-alternation coordinates and subsequent activation of torsional modes account for the loss of stimulated emission corresponding to the ~30 fs decay timescale. Similar to the β-carotene study in the previous chapter, the kinetic I state can be understood

in this context as existing near the "planar minimum" state on the S_2 state potential near the transition state where the molecule becomes torsionally active(see Figure 4.14). Pyramidalization of a carbon atom during the first ultrafast kinetic event ($\tau \approx 30$ fs) leading to the I state could act to lower the transition-state barrier,[55,150,152] increasing the rate to the S_1 state. Crossing of this barrier occurs on ~600 fs timescale leads to population of the torsionally displaced, S_1 state via a conical intersection (CI). This conformational change is likely to enhance the ICT character observed in the S_1 state.

Similar integrated transient-grating dynamics for the absorption component signal of peridinin in PCP are observed with perhaps indistinguishable S_2 lifetimes (31 fs for peridinin, 27 fs in PCP) and only a modestly faster decay timescale corresponding to the I state in PCP compared to peridinin in methanol (565 vs 615 fs). The amplitude of the ESA is larger in the case of peridinin in methanol than in PCP due the loss in I and S_1 state population due to energy transfer to Chl *a* in PCP and the difference in dipole strength of the associated transitions (see Tables 5.1 and 5.2). In both cases, the decay of the ESA signal to baseline occurs as population in the S_1 state decays to the ground state.

The dispersion component-signal for peridinin (Figure 5.4b) exhibits an instrument response-limited rise, but is delayed by ~30 fs. In the dispersion channel, the rising signal corresponds to ESA transitions, likely arising via transitions from the I and S_1 states as above, but the longer timescale decay in the dispersion signal occurs on a different timescale than in the absorption signal. The decay of the S_1 state exhibits differing kinetics in the absorption and dispersion

signal of peridinin in methanol, suggesting that population redistribution occurs in the S_0 state, similar to Cho and Fleming's work on the torsionally active molecules crystal violet and malachite green,[54] and our previous work on β-carotene. In the case of β-carotene, the vibrational cooling was attributed to relaxation from a conformationally twisted S_1 state to a displaced S_0^* state. Conversely, in the case of peridinin in PCP, the rise of the absorption and dispersion component signals occur synchronously and both signals are modeled globally, with the long-time signal decaying on the same timescale (16 ps). This global timescale observed in PCP suggests that decay from the S_1 state populates the initial ground state which is likely due to the protein matrix enforcing a more static conformation of peridinin than the conformations accessible in solution.

Using the kinetic picture outlined above, some transient-grating spectral features within the limited bandwidth of our instrument can be identified for each state. For peridinin in methanol, the early-time transient-grating absorption spectra (Figures 5.7a and 5.8, $T \leq 0$ fs), corresponding to the initially pumped S_2 state, exhibit a strong PB+SE signal centered around the laser spectrum at 519 nm with a weak ESA-dominated component to the blue side of this feature. The PB+SE component begins to broaden, the weak ESA feature to the blue subsides, and a strong ESA feature to the red begins to form as the I state is populated from the S_2 state on a ~30 fs timescale. The signal from the intermediate state dominates contributions from the earlier S_2 and subsequent S_1 state at around 75 fs (see Figure 5.8). The 75 fs transient-grating spectrum in Figure 5.8 shows a significantly smaller PB+SE component that becomes dominated by the ESA feature to the blue.

The broad ESA feature corresponding to the $S_1 \rightarrow S_n$ continues to grow as all of the population is transferred to the S_1 state, where the ESA dominates all other signal intensity by about 200 fs. The shape of the transient-grating spectra remains relatively constant after approximately 1 ps, as the signal decays to baseline due to nonradiative decay of population to the S_0 state.

The transient-grating absorption spectra for peridinin in PCP, shown in Figures 5.7b and 5.9 show similar spectral features, but with differing time-evolutions. Similar to peridinin in methanol, the early-time transient-grating absorption spectra ($T \leq 0$) corresponding to the initial S_2 state have a PB+SE feature peaked around the excitation spectrum at 519 nm and a weak ESA feature to the blue. Peridinin in PCP, however, has an ESA feature to the red of the PB+SE feature at all times that does not occur with peridinin in solution until the I state becomes sufficiently populated. This can be easily observed by comparing the $T < 0$ fs spectral contour maps for peridinin in methanol and in PCP (Figure 5.7). The initial S_2 state for peridinin in PCP looks spectrally very similar to the I state for peridinin in methanol, and although there are changes in the signal intensity for the PB+SE and ESA components, the shape of the spectrum remains similar throughout the entire measured timescale. The PCP transient-grating spectra suggest that a state which looks like the I state of peridinin in methanol, is prepared by the protein matrix. A comparison of the structure of peridinin in PCP to the planar structure suggests that the nature of this state is likely twisted. Further, the positive PB+SE feature that is present in the initially prepared S_2 state persists through the timescale of the experiment, never being completely dominated by the red ESA

feature. This supports the idea that the S_1/ICT state could be mixed with the S_2 state to borrow dipole strength, which would increase $S_1 \rightarrow Q_y$ energy transfer and implicates twisting as the mechanism for this state mixing. Finally, the identity of the kinetic I state is unlikely to $1B_u^-$ state, but rather a twisted structure on the S_2 state potential, in accordance with the two-state, two-mode theory by Olivucci.[1]

LITERATURE CITED

LITERATURE CITED

(1) Sanchez-Galvez, A.; Hunt, P.; Robb, M. A.; Olivucci, M.; Vreven, T.; Schlegel, H. B. Ultrafast radiationless deactivation of organic dyes: evidence for a two-state two-mode pathway in polymethine cyanines. *J. Am. Chem. Soc.* **2000**, *122*, 2911-2924. DOI: 10.1021/ja993985x

(2) Sundström, V. Photosynthetic light harvesting, charge separation, and photoprotection: the primary steps. In *Photobiology: The Science of Life and Light*; Second Edition ed.; Björn, L. O., Ed.; Springer: New York, 2007, p 289-319.

(3) Polívka, T.; Sundström, V. Ultrafast dynamics of carotenoids excited states—from solution to natural and artificial systems. *Chem. Rev.* **2004**, *104*, 2021-2071. DOI: 10.1021/cr020674n.

(4) Liu, Z. F.; Yan, H. C.; Wang, K. B.; Kuang, T. Y.; Zhang, J. P.; Gui, L. L.; An, X. M.; Chang, W. R. Crystal structure of spinach major light-harvesting complex at 2.72 Å resolution. *Nature* **2004**, *428*, 287-292.

(5) Standfuss, J.; Terwisscha van Scheltinga, A. C.; Lamborghini, M.; Kühlbrandt, W. Mechanisms of photoprotection and nonphotochemical quenching in pea light-harvesting complex at 2.5 Å resolution. *EMBO J.* **2005**, *24*, 919-928. DOI: 10.1038/sj.emboj.7600585.

(6) Frank, H. A.; Brudvig, G. W. Redox functions of carotenoids in photosynthesis. *Biochemistry* **2004**, *43*, 8607-8615. DOI: 10.1021/bi0492096.

(7) Willcox, J. K.; Ash, S. L.; Catignani, G. L. Antioxidants and Prevention of Chronic Disease. *Crit. Rev. Food Sci. Nutrit.* **2004**, *44*, 275-295. DOI: 10.1080/10408690490468489.

(8) Polívka, T.; Frank, H. A. Molecular factors controlling photosynthetic light harvesting by carotenoids. *Acc. Chem. Res.* **2010**, *2010*, 1125-1134. DOI: 10.1021/ar100030m.

(9) Polívka, T.; Sundström, V. Dark excited states of carotenoids: consensus and controversy. *Chem. Phys. Lett.* **2009**, *477*, 1–11. DOI: 10.1016/j.cplett.2009.06.011.

(10) Birge, R. R. Two photon spectroscopy of protein-bound chromophores. *Acc. Chem. Res.* **1986**, *19*, 138-146.

(11) Christensen, R. L. The electronic states of carotenoids. In *The Photochemistry of Carotenoids*; Frank, H. A., Young, A. J., Britton, G., Cogdell, R. J., Eds.; Kluwer Academic Publishers: Dordrecht, 1999; Vol. 8, p 137-159.

(12) Frank, H. A.; Desamero, R. Z. B.; Chynwat, V.; Gebhard, R.; van der Hoef, I.; Jansen, F. J.; Lugtenburg, J.; Gosztola, D.; Wasielewski, M. R. Spectroscopic properties of spheroidene analogs having different extents of π-electron conjugation. *J. Phys. Chem. A* **1997**, *101*, 149-157. DOI: 10.1021/jp962373l.

(13) Frank, H. A.; Josue, J. S.; Bautista, J. A.; van der Hoef, I.; Jansen, F. J.; Lugtenburg, J.; Wiederrecht, G.; Christensen, R. L. Spectroscopic and photochemical properties of open-chain carotenoids. *J. Phys. Chem. B* **2002**, *106*, 2083-2092.

(14) Frank, H. A.; Das, S. K.; Bautista, J. A.; Bruce, D.; Crimi, M.; Croce, R.; Bassi, R. Photochemical behavior of xanthophylls in the recombinant photosystem II antenna complex, CP26. *Biochemistry* **2001**, *40*, 1220-1225. DOI: 10.1021/bi001160q.

(15) Polívka, T.; Zigmantas, D.; Sundström, V.; Formaggio, E.; Cinque, G.; Bassi, R. Carotenoid S_1 state in a recombinant light-harvesting complex of photosystem II. *Biochemistry* **2001**, *41*, 439-450. DOI: 10.1021/bi011589x.

(16) Richter, M.; Goss, R.; Wagner, B.; Holzwarth, A. R. Characterization of the fast and slow reversible components of non-photochemical quenching in isolated pea thylakoids by picosecond time-resolved chlorophyll fluorescence analysis. *Biochemistry* **1999**, *38*, 12718-12726. DOI: 10.1021/bi983009a.

(17) Frank, H. A.; Cua, A.; Chynwat, V.; Young, A.; Gosztola, D.; Wasielewski, M. R. Photophysics of the carotenoids associated with the xanthophyll cycle in photosynthesis. *Photosyn. Res.* **1994**, *41*, 389-395.

(18) Holt, N. E.; Zigmantas, D.; Valkunas, L.; Li, X.-P.; Niyogi, K. K.; Fleming, G. R. Carotenoid cation formation and the regulation of photosynthetic light harvesting. *Science* **2005**, *307*, 433-436. DOI: 10.1126/science.1105833.

(19) Ma, Y.-Z.; Holt, N. E.; Li, X.-P.; Niyogi, K. K.; Fleming, G. R. Evidence for direct carotenoid involvement in the regulation of photosynthetic light harvesting. *Proc. Natl. Acad. Sci. U.S.A* **2003**, *100*, 4377-4382. DOI: 10.1073/pnas.0736959100.

(20) Crofts, A. R.; Yerkes, C. T. A molecular mechanism for qE-quenching. *FEBS Lett.* **1994**, *352*, 265-270. DOI: 10.1016/0014-5793(94)00976-7.

(21) Tavan, P.; Schulten, K. Electronic excitations in finite and infinite polyenes. *Phys. Rev. B* **1987**, *36*, 4337-4358. DOI: 10.1103/PhysRevB.36.4337.

(22) Koyama, Y.; Rondonuwu, F. S.; Fujii, R.; Watanabe, Y. Light-harvesting function of carotenoids in photo-synthesis: The roles of the newly found $1^1B_u^-$ state. *Biopolymers* **2004**, *74*, 2-18.

(23) Wohlleben, W.; Buckup, T.; Hashimoto, H.; Cogdell, R. J.; Herek, J. L.; Motzkus, M. Pump–deplete–probe spectroscopy and the puzzle of carotenoid dark states. *J. Phys. Chem. B* **2004**, *108*, 3320-3325. DOI: 10.1021/jp036145k.

(24) Ostroumov, E. E.; Mulvaney, R. M.; Cogdell, R. J.; Scholes, G. D. Broadband 2D electronic spectroscopy reveals a carotenoid dark state in purple bacteria. *Science* **2013**, *340*, 52-56. DOI: 10.1126/science.1230106.

(25) Ostroumov, E. E.; Mulvaney, R. M.; Anna, J. M.; Cogdell, R. J.; Scholes, G. D. Energy transfer pathways in light-harvesting complexes of purple bacteria as revealed by global kinetic analysis of two-dimensional transient spectra. *J. Phys. Chem. B* **2013**, *117*, 11349-11362. DOI: 10.1021/jp403028x.

(26) Gradinaru, C. C.; Kennis, J. T. M.; Papagiannakis, E.; van Stokkum, I. H. M.; Cogdell, R. J.; Fleming, G. R.; Niederman, R. A.; van Grondelle, R. An unusual pathway of excitation energy deactivation in carotenoids: singlet-to-triplet conversion on an ultrafast timescale in a photosynthetic antenna. *Proc. Natl. Acad. Sci. U.S.A.* **2001**, *98*, 2364-2369. DOI: 10.1073/pnas.051501298.

(27) Kosumi, D.; Yanagi, K.; Fujii, R.; Hashimoto, H.; Yoshizawa, M. Conjugation length dependence of relaxation kinetics in β-carotene homologs probed by femtosecond Kerr-gate fluorescence spectroscopy. *Chem. Phys. Lett.* **2006**, *425*, 66-70. DOI: 10.1016/j.cplett.2006.05.023.

(28) Zhang, J. P.; Inaba, T.; Watanabe, Y.; Koyama, Y. Excited-state dynamics among the $1B_u^+$, $1B_u^-$ and $2A_g^-$ states of *all-trans*-neurosporene as revealed by near-infrared time-resolved absorption spectroscopy. *Chem. Phys. Lett.* **2000**, *332*, 351-358.

(29) Fujii, R.; Fujino, T.; Inaba, T.; Nagae, H.; Koyama, Y. Internal conversion of $1B_u^+$ -> $1B_u^-$ -> $2A_g^-$ and fluorescence from the $1B_u^-$ state in all-*trans*-neurosporene as probed by up-conversion spectroscopy. *Chem. Phys. Lett.* **2004**, *384*, 9-15.

(30) Cerullo, G.; Polli, D.; Lanzani, G.; De Silvestri, S.; Hashimoto, H.; Cogdell, R. J. Photosynthetic light harvesting by carotenoids: Detection of an intermediate excited state. *Science* **2002**, *298*, 2395-2398. DOI: 10.1126/science.1074685.

(31) McCamant, D. W.; Kukura, P.; Mathies, R. A. Femtosecond time-resolved stimulated Raman spectroscopy: application to the ultrafast internal conversion in β-carotene. *J. Phys. Chem. A.* **2003**, *107*, 8208-8214.

(32) Christensson, N.; Polívka, T.; Yartsev, A.; Pullerits, T. Photon echo spectroscopy reveals structure-dynamics relationships in carotenoids. *Phys. Rev. B* **2009**, *79*, 245118. DOI: 10.1103/PhysRevB.79.245118.

(33) Ostroumov, E. E.; Muller, M. G.; Reus, M.; Holzwarth, A. R. On the nature of the "dark S*" excited state of β-carotene. *J. Phys. Chem. A* **2011**, *115*, 3698-3712. DOI: 10.1021/jp105385c.

(34) Fujii, R.; Onaka, K.; Kuki, M.; Koyama, Y.; Watanabe, Y. The $2A_g^-$ energies of all-*trans*-neurosporene and spheroidene as determined by fluorescence spectroscopy. *Chem. Phys. Lett.* **1998**, *288*, 847-853.

(35) Fujii, R.; Ishikawa, T.; Koyama, Y.; Taguchi, M.; Isobe, Y.; Nagae, H.; Watanabe, Y. Fluorescence spectroscopy of all-*trans*-anhydrorhodovibrin and spirilloxanthin: Detection of the $1B_u^-$ fluorescence. *J. Phys. Chem. A* **2001**, *105*, 5348-5355.

(36) Lukeš, V.; Christensson, N.; Milota, F.; Kauffmann, H. F.; Hauer, J. Electronic ground state conformers of β-carotene and their role in ultrafast spectroscopy. *Chem. Phys. Lett.* **2011**, *506*, 122-127. DOI: 10.1016/j.cplett.2011.02.060.

(37) Polli, D.; Cerullo, G.; Lanzani, G.; De Silvestri, S.; Yanagi, K.; Hashimoto, H.; Cogdell, R. Conjugation length dependence of internal conversion in carotenoids: role of the intermediate state. *Phys. Rev. Lett.* **2004**, *93*. DOI: 10.1103/PhysRevLett.93.163002.

(38) Fujii, R.; Inaba, T.; Watanabe, Y.; Koyama, Y.; Zhang, J. P. Two different pathways of internal conversion in carotenoids depending on the length of the conjugated chain. *Chem. Phys. Lett.* **2003**, *369*, 165-172.

(39) Andersson, P. O.; Gillbro, T. Photophysics and dynamics of the lowest excited singlet state in long substituted polyenes with implications to the very long-chain limit. *J. Chem. Phys.* **1995**, *103*, 2509-2519. DOI: 10.1063/1.469672.

(40) Niedzwiedzki, D.; Koscielecki, J. F.; Cong, H.; Sullivan, J. O.; Gibson, G. N.; Birge, R. R.; Frank, H. A. Ultrafast dynamics and excited state spectra of open-chain carotenoids at room and low temperatures. *J. Phys. Chem. B* **2007**, *111*, 5984-5998.

(41) Cong, H.; Niedzwiedzki, D. M.; Gibson, G. N.; Frank, H. A. Ultrafast time-resolved spectroscopy of xanthophylls at low temperature. *J. Phys. Chem. B* **2008**, *112*, 3558-3567.

(42) Niedzwiedzki, D. M.; Sullivan, J. O.; Polívka, T.; Birge, R. R.; Frank, H. A. Femtosecond time-resolved transient absorption spectroscopy of xanthophylls. *J. Phys. Chem. B* **2006**, *110*, 22872-22885. DOI: 10.1021/jp0622738.

(43) Papagiannakis, E.; Kennis, J. T. M.; van Stokkum, I. H. M.; Cogdell, R. J.; van Grondelle, R. An alternative carotenoid-to-bacteriochlorophyll energy transfer pathway in photosynthetic light harvesting. *Proc. Natl. Acad. Sci. U.S.A.* **2002**, *99*, 6017-6022. DOI: 10.1073/pnas.092626599.

(44) Hofmann, E.; Wrench, P. M.; Sharples, F. P.; Hiller, R. G.; Welte, W.; Diederichs, K. Structural basis of light harvesting by carotenoids: peridinin-chlorophyll-protein from *Amphidinium carterae*. *Science* **1996**, *272*, 1788–1791. DOI: 10.1126/science.272.5269.1788.

(45) Damjanović, A.; Ritz, T.; Schulten, K. Excitation transfer in the peridinin-chlorophyll-protein of *Amphidinium carterae*. *Biophys. J.* **2000**, *79*, 1695–1705. DOI: 10.1016/S0006-3495(00)76422-8.

(46) Shima, S.; Ilagan, R. P.; Gillespie, N.; Sommer, B. J.; Hiller, R. G.; Sharples, F. P.; Frank, H. A.; Birge, R. R. Two-photon and fluorescence spectroscopy and the effect of environment on the photochemical properties of peridinin in solution and in the peridinin-chlorophyll-protein from *Amphidinium carterae*. *J. Phys. Chem. A* **2003**, *107*, 8052-8066. DOI: 10.1021/jp022648z.

(47) Schulte, T.; Niedwiedzki, D. M.; Birge, R. R.; Hiller, R. G.; Polívka, T.; Hofmann, E.; Frank, H. A. Identification of a single peridinin sensing Chl-*a* excitation in reconstituted PCP by crystallography and spectroscopy. *Proc. Natl. Acad. U.S.A.* **2009**, *106*, 20474-20769. DOI: 10.1073/pnas.0908938106.

(48) Collini, E.; Wong, C. Y.; Wilk, K. E.; Curmi, P. M. G.; Brumer, P.; Scholes, G. D. Coherently wired light-harvesting in photosynthetic marine algae at ambient temperature. *Nature* **2010**, *463*, 644. DOI: 10.1038/nature08811.

(49) Hossein-Nejad, H.; Curutchet, C.; Kubica, A.; Scholes, G. D. Delocalization-enhanced long-range energy transfer between cryptophyte algae PE545 antenna proteins. *J. Phys. Chem. B* **2010**, *115*, 5243. DOI: 10.1021/jp108397a.

(50) Brixner, T.; Stenger, J.; Vaswani, H. M.; Cho, M.; Blankenship, R. E.; Fleming, G. R. Two-dimensional spectroscopy of electronic couplings in photosynthesis. *Nature* **2005**, *434*, 625-628.

(51) Christensson, N.; Chábera, P.; Hiller, R. G.; Pullerits, T.; Polívka, T. Four-wave-mixing spectroscopy of peridinin in solution and in the peridinin–chlorophyll-*a* protein. *Chem. Phys.* **2010**, *373*, 15-22. DOI: 10.1016/j.chemphys.2009.12.011.

(52) Zigmantas, D.; Hiller, R. G.; Polívka, T.; Sundström, V. Carotenoid to chlorophyll energy transfer in the peridinin–chlorophyll-*a*–protein complex involves an intramolecular charge transfer state. *Proc. Natl. Acad. Sci. USA* **2002**, *99*, 16760-16765. DOI: 10.1073/pnas.262537599.

(53) Linden, P. A.; Zimmermann, J.; Brixner, T.; Holt, N. E.; Vaswani, H. M.; Hiller, R. G.; Fleming, G. R. Transient absorption study of peridinin and peridinin–chlorophyll *a*–protein after two-photon excitation. *J. Phys. Chem. B* **2004**, *108*, 10340-10345. DOI: 10.1021/jp031331b.

(54) Xu, Q.-H.; Ma, Y.-Z.; Fleming, G. R. Different real and imaginary components of the resonant third-order polarization revealed by optical heterodyne detected transient grating spectroscopic studies of crystal violet: model and experiment. *J. Phys. Chem. A* **2002**, *106*, 10755. DOI: 10.1021/jp014714n.

(55) Levine, B. G.; Martinez, T. J. Isomerization through conical intersections. *Annu. Rev. Phys. Chem.* **2007**, *58*, 613-634. DOI: 10.1146/annurev.physchem.57.032905.104612.

(56) Malhado, J. P.; Spezia, R.; Hynes, J. T. Dynamical friction effects on the photoisomerization of a model protonated Schiff base in solution. *J. Phys. Chem. A* **2011**, *115*, 3720-3735. DOI: 10.1021/jp106096m.

(57) Schoenlein, R. W.; Peteanu, L. A.; Mathies, R. A.; Shank, C. V. The first step in vision: femtosecond isomerization of rhodopsin. *Science* **1991**, *254*, 412-415. DOI: 10.1126/science.1925597.

(58) Wang, Q.; Schoenlein, R. W.; Peteanu, L. A.; Mathies, R. A.; Shank, C. V. Vibrationally coherent photochemistry in the femtosecond primary event of vision. *Science* **1994**, *266*, 422-424. DOI: 10.1126/science.7939680.

(59) Stratt, R. M.; Maroncelli, M. Nonreactive dynamics in solution: the emerging molecular view of solvation dynamics and vibrational relaxation. *J. Phys. Chem.* **1996**, *100*, 12981-12996. DOI: 10.1021/jp9608483.

(60) Fleming, G. R. *Chemical Applications of Ultrafast Spectroscopy*; Oxford University Press: New York, 1986.

(61) Barbara, P. F.; Walker, G. C.; Smith, T. P. Vibrational modes and the dynamic solvent effect in electron and proton transfer. *Science* **1992**, *256*, 975-981.

(62) Maroncelli, M. The dynamics of solvation in polar solvents. *J. Mol. Liq.* **1993**, *57*, 1-37. DOI: 10.1016/0167-7322(93)80045-W.

(63) Maroncelli, M.; MacInnis, J.; Fleming, G. R. Polar solvent dynamics and electron-transfer reactions. *Science* **1989**, *243*, 1674-1681. DOI: 10.1126/science.243.4899.1674.

(64) Joo, T.; Jia, Y.; Yu, J.-Y.; Lang, M. J.; Fleming, G. R. Third-order nonlinear time domain probes of solvation dynamics. *J. Chem. Phys.* **1996**, *104*, 6089-6108. DOI: 10.1063/1.471276.

(65) Cho, M.; Yu, J.-Y.; Joo, T.; Nagasawa, Y.; Passino, S. A.; Fleming, G. R. The integrated photon echo and solvation dynamics. *J. Phys. Chem.* **1996**, *100*, 11944-11953. DOI: 10.1021/jp9601983.

(66) Barthel, E. R.; Martini, I. B.; Schwartz, B. J. How does the solvent control electron transfer? Experimental and theoretical studies of the simplest charge transfer reaction. *J. Phys. Chem. B* **2001**, *105*, 12230-12241. DOI: 10.1021/jp011150e.

(67) Nilsson, L.; Halle, B. Molecular origin of time-dependent fluorescence shifts in proteins. *Proc. Natl. Acad. Sci. U.S.A.* **2005**, *102*, 13867-13872. DOI: 10.1073/pnas.0504181102.

(68) Stratt, R. M.; Cho, M. The short-time dynamics of solvation. *J. Chem. Phys.* **1994**, *100*, 6700-6708. DOI: 10.1063/1.467030.

(69) Stratt, R. M. The instantaneous normal modes of liquids. *Acc. Chem. Res.* **1995**, *28*, 201-207. DOI: 10.1021/ar00053a001.

(70) Jimenez, R.; Fleming, G. R.; Kumar, P. V.; Maroncelli, M. Femtosecond solvation dynamics of water. *Nature* **1994**, *369*, 471-473. DOI: 10.1038/369471a0.

(71) Berg, M. Viscoelastic continuum model of nonpolar solvation. 1. Implications for multiple time scales in liquid dynamics. *J. Phys. Chem. A* **1998**, *102*, 17-30. DOI: 10.1021/jp9722061.

(72) Patterson, G.; Davidson, M.; Manley, S.; Lippincott-Schwartz, J. Superresolution imaging using single-molecule localization. *Annu. Rev. Phys. Chem.* **2010**, *61*, 345-367. DOI: 10.1146/annurev.physchem.012809.103444.

(73) Flors, C. DNA and chromatin imaging with super-resolution fluorescence microscopy based on single-molecule localization. *Biopolymers* **2011**, *95*, 290-297. DOI: 10.1002/bip.21574.

(74) Hope-Roberts, M.; Wainwright, M.; Horobin, R. W. Real-time imaging of bacteria in living mice using a fluorescent dye. *Biotech. Histochem.* **2011**, *86*, 104-107. DOI: 10.3109/10520295.2010.498295.

(75) Köhn, F.; Hofkens, J.; Gronheid, R.; Van der Auweraer, M.; De Schryver, F. C. Parameters influencing the on- and off-times in the fluorescence intensity traces of single cyanine dye molecules. *J. Phys. Chem. A* **2002**, *106*, 4808-4814. DOI: 10.1021/jp012959u.

(76) Ma, X.; Hua, J.; Wu, W.; Jin, Y.; Meng, F.; Zhan, W.; Tian, H. A high-efficiency cyanine dye for dye-sensitized solar cells. *Tetrahedron* **2008**, *64*, 345-350. DOI: 10.1016/j.tet.2007.10.094.

(77) Funabiki, K.; Mase, H.; Hibino, A.; Tanaka, N.; Mizuhata, N.; Sakuragi, Y.; Nakashima, A.; Yoshida, T.; Kubota, Y.; Matsui, M. Synthesis of a novel heptamethine-cyanine dye for use in near-infrared active dye-sensitized solar cells with porous zinc oxide prepared at low temperature. *Energy Environ. Sci.* **2011**, *4*, 2186-2192. DOI: 10.1039/c1ee01141c.

(78) Pierce, R. A.; Berg, R. A. Triplet absorption spectra of cyanine dyes. *J. Chem. Phys.* **1969**, *51*, 1267-1267. DOI: 10.1063/1.1672144.

(79) Kasatani, K.; Kawasaki, M.; Sato, H. Short-wavelength fluorescence caused by sequential two-photon excitation of some cyanine dyes: effect of solvent viscosity on the quantum yields. *Chem. Phys.* **1984**, *83*, 461-469. DOI: 10.1016/0301-0104(84)85020-X.

(80) Tan, C.; Atas, E.; Müller, J. G.; Pinto, M. R.; Kleiman, V. D.; Schanze, K. S. Amplified quenching of a conjugated polyelectrolyte by cyanine dyes. *J. Am. Chem. Soc.* **2004**, *126*, 13685-13694. DOI: 10.1021/ja046856b.

(81) Peng, X.; Yang, Z.; Wang, J.; Fan, J.; He, Y.; Song, F.; Wang, B.; Sun, S.; Qu, J.; Qi, J.; Yan, M. Fluorescence ratiometry and fluorescence lifetime imaging: using a single molecular sensor for dual mode imaging of cellular viscosity. *J. Am. Chem. Soc.* **2011**, *133*, 6626-6635. DOI: 10.1021/ja1104014.

(82) Åberg, U.; Sundström, V. Photochemical isomerization in the absence of a potential barrier: origin of wavelength-dependent ground-state recovery kinetics. *Chem. Phys. Lett.* **1991**, *185*, 461-467. DOI: 10.1016/0009-2614(91)80243-Q.

(83) Yartsev, A.; Alvarez, J. L.; Åberg, U.; Sundström, V. Overdamped wavepacket motion along a barrierless potential energy surface in excited state isomerization. *Chem. Phys. Lett.* **1995**, *243*, 281-289. DOI: 10.1016/0009-2614(95)00858-2.

(84) Vogt, G.; Nuernberger, P.; Gerber, G.; Improta, R.; Santoro, F. Femtosecond study on the isomerization dynamics of NK88. II. Excited-state dynamics. *J. Chem. Phys.* **2006**, *125*, 044513. DOI: 10.1063/1.2210939.

(85) Dietzek, B.; Christensson, N.; Pascher, T.; Pullerits, T.; Yartsev, A. Ultrafast excited-state isomerization dynamics of 1,1‘-diethyl-2,2‘-cyanine studied by four-wave mixing spectroscopy. *J. Phys. Chem. B* **2007**, *111*, 5396-5404. DOI: 10.1021/jp0685277.

(86) Dietzek, B.; Brüggemann, B.; Persson, P.; Yartsev, A. On the excited-state multi-dimensionality in cyanines. *Chem. Phys. Lett.* **2008**, *455*, 13-19. DOI: 10.1016/j.cplett.2008.02.066.

(87) Weigel, A.; Pfaffe, M.; Sajadi, M.; Mahrwald, R.; Improta, R.; Barone, V.; Polli, D.; Cerullo, G.; Ernsting, N. P.; Santoro, F. Barrierless photoisomerisation of the "simplest cyanine": joining computational and femtosecond optical spectroscopies to trace the full reaction path. *Phys. Chem. Chem. Phys.* **2012**, *14*, 13350-13364. DOI: 10.1039/c2cp41522d.

(88) Adamson, B. D.; Coughlan, N. J. A.; da Silva, G.; Bieske, E. J. Photoisomerization action spectroscopy of the carbocyanine dye DTC^+ in the gas phase. *J. Phys. Chem. A* **2013**. DOI: 10.1021/jp405747q.

(89) Huang, Y.; Cheng, T.; Li, F.; Huang, C.-H.; Wang, S.; Huang, W.; Gong, Q. Photophysical studies on the mono- and dichromophoric hemicyanine dyes III.

Ultrafast fluorescence up-conversion in methanol: twisting intramolecular charge transfer and "two-state three-mode" model. *J. Phys. Chem. B* **2002**, *106*, 10041-10050. DOI: 10.1021/jp0208788.

(90) Laia, C. A. T.; Costa, S. l. M. B. Thermal isomerization of a symmetrical carbocyanine molecule: charge transfer aspects. *Chem. Phys. Lett.* **2002**, *354*, 435-442. DOI: 10.1016/S0009-2614(02)00157-4.

(91) Grabowski, Z. R.; Rotkiewicz, K.; Rettig, W. Structural changes accompanying intramolecular electron transfer: focus on twisted intramolecular charge-transfer states and structures. *Chem. Rev.* **2003**, *103*, 3899-4032. DOI: 10.1021/cr940745l.

(92) Tran, V.; Schwartz, B. J. Role of nonpolar forces in aqueous solvation: computer simulation study of solvation dynamics in water following changes in solute size, shape, and charge. *J. Phys. Chem. B* **1999**, *103*, 5570-5580. DOI: 10.1021/jp990993r.

(93) Du, Q.; Beglov, D.; Roux, B. Solvation free energy of polar and nonpolar molecules in water: an extended interaction site integral equation theory in three dimensions. *J. Phys. Chem. B* **2000**, *104*, 796-805. DOI: 10.1021/jp992712l.

(94) Aherne, D.; Tran, V.; Schwartz, B. J. Nonlinear, nonpolar solvation dynamics in water: the roles of electrostriction and solvent translation in the breakdown of linear response. *J. Phys. Chem. B* **2000**, *104*, 5382-5394. DOI: 10.1021/jp000326u.

(95) Åberg, U.; Åkesson, E.; Alvarez, J.-L.; Fedchenia, I.; Sundström, V. Femtosecond spectral evolution monitoring the bond-twisting event in barrierless isomerization in solution. *Chem. Phys.* **1994**, *183*, 269-288. DOI: 10.1016/0301-0104(94)00022-0.

(96) Xu, Q.-H.; Fleming, G. R. Isomerization dynamics of 1,1'-diethyl-4,4'-cyanine (1144C) studied by different third-order nonlinear spectroscopic measurements. *J. Phys. Chem. A* **2001**, *105*, 10187. DOI: 10.1021/jp011924r.

(97) Dietzek, B.; Yartsev, A.; Tarnovsky, A. N. Watching ultrafast barrierless excited-state isomerization of pseudocyanine in real time. *J. Phys. Chem. B* **2007**, *111*, 4520-4526. DOI: 10.1021/jp066471a.

(98) Wei, Z.; Nakamura, T.; Takeuchi, S.; Tahara, T. Tracking of the nuclear wavepacket motion in cyanine photoisomerization by ultrafast pump–dump–probe spectroscopy. *J. Am. Chem. Soc.* **2011**, *133*, 8205-8210. DOI: 10.1021/ja110716b.

(99) Dietzek, B.; Brüggemann, B.; Pascher, T.; Yartsev, A. Mechanisms of molecular response in the optimal control of photoisomerization. *Phys. Rev. Lett.* **2006**, *97*, 258301. DOI: 10.1103/PhysRevLett.97.258301.

(100) Dietzek, B.; Pascher, T.; Yartsev, A. Tracking ultrafast excited-state bond-twisting motion in solution close to the franck–condon point. *J. Phys. Chem. B* **2007**, *111*, 6034-6041. DOI: 10.1021/jp068652i.

(101) Hunt, P. A.; Robb, M. A. Systematic control of photochemistry: the dynamics of photoisomerization of a model cyanine dye. *J. Am. Chem. Soc.* **2005**, *127*, 5720-5726. DOI: 10.1021/ja045652s.

(102) Vogt, G.; Krampert, G.; Niklaus, P.; Nuernberger, P.; Gerber, G. Optimal control of photoisomerization. *Phys. Rev. Lett.* **2005**, *94*, 068305. DOI: 10.1103/PhysRevLett.94.068305.

(103) Mathies, R. A.; Brito Cruz, C. H.; Pollard, W. T.; Shank, C. V. Direct observation of the femtosecond excited-state *cis-trans* isomerization in bacteriorhodopsin. *Science* **1988**, *240*, 777-779. DOI: 10.1126/science.3363359.

(104) Bagchi, B.; Fleming, G. R.; Oxtoby, D. W. Theory of electronic relaxation in solution in the absence of an activation barrier. *J. Chem. Phys.* **1983**, *78*, 7375-7385. DOI: 10.1063/1.444729.

(105) Bertolino, C. A.; Ferrari, A. M.; Barolo, C.; Viscardi, G.; Caputo, G.; Coluccia, S. Solvent effect on indocyanine dyes: a computational approach. *Chem. Phys.* **2006**, *330*, 52-59. DOI: 10.1016/j.chemphys.2006.07.045.

(106) Cao, J.; Hu, C.; Liu, F.; Sun, W.; Fan, J.; Song, F.; Sun, S.; Peng, X. Mechanism and nature of the different viscosity sensitivities of hemicyanine dyes with various heterocycles. *Chem. Phys. Chem.* **2013**, *14*, 1601-1608. DOI: 10.1002/cphc.201300049.

(107) Yu, A.; Tolbert, C. A.; Farrow, D. A.; Jonas, D. M. Solvatochromism and solvation dynamics of structurally related cyanine dyes. *J. Phys. Chem. A* **2002**, *106*, 9407-9419. DOI: 10.1021/jp0205867.

(108) Moran, A. M.; Maddox, J. B.; Hong, J. W.; Kim, J.; Nome, R. A.; Bazan, G. C.; Mukamel, S.; Scherer, N. F. Optical coherence and theoretical study of the excitation dynamics of a highly symmetric cyclophane-linked oligophenylenevinylene dimer. *J. Chem. Phys.* **2006**, *124*, 194904. DOI: 10.1063/1.2196041.

(109) Brixner, T.; Mančal, T.; Stiopkin, I. V.; Fleming, G. R. Phase-stabilized two-dimensional electronic spectroscopy. *J. Chem. Phys.* **2004**, *121*, 4221. DOI: 10.1063/1.1776112.

(110) Frisch, M. J.; Trucks, G. W.; Schlegel, H. B.; Scuseria, G. E.; Robb, M. A.; Cheeseman, J. R.; Montgomery, J. A., Jr; Vreven, T.; Kudin, K. N.; Burant, J. C.; Millam, J. M.; Iyengar, S. S.; Tomasi, J.; Barone, V.; Mennucci, B.; Cossi, M.; Scalmani, G.; Rega, N.; Petersson, G. A.; Nakatsuji, H.; Hada, M.; Ehara, M.; Toyota, K.; Fukuda, R.; Hasegawa, J.; Ishida, M.; Nakajima, T.; Honda, Y.; Kitao, O.; Nakai, H.; Klene, M.; Li, X.; Knox, J. E.;

Hratchian, H. P.; Cross, J. B.; Bakken, V.; Adamo, C.; Jaramillo, J.; Gomperts, R.; Stratmann, R. E.; Yazyev, O.; Austin, A. J.; Cammi, R.; Pomelli, C.; Ochterski, J. W.; Ayala, P. Y.; Morokuma, K.; Voth, G. A.; Salvador, P.; Dannenberg, J. J.; Zakrzewski, V. G.; Dapprich, S.; Daniels, A. D.; Strain, M. C.; Farkas, O.; Malick, D. K.; Rabuck, A. D.; Raghavachari, K.; Foresman, J. B.; Ortiz, J. V.; Cui, Q.; Baboul, A. G.; Clifford, S.; Cioslowski, J.; Stefanov, B. B.; Liu, G.; Liashenko, A.; Piskorz, P.; Komaromi, I.; Martin, R. L.; Fox, D. J.; Keith, T.; Al-Laham, M. A.; Peng, C. Y.; Nanayakkara, A.; Challacombe, M.; Gill, P. M. W.; Johnson, B.; Chen, W.; Wong, M. W.; Gonzalez, C.; Pople, J. A. *Gaussian 03, Revision D.01*; Gaussian, Inc.: Wallingford, CT, 2004.

(111) Peteanu, L. A.; Schoenlein, R. W.; Wang, Q.; Mathies, R. A.; Shank, C. V. The first step in vision occurs in femtoseconds: complete blue and red spectral studies. *Proc. Natl. Acad. Sci. U.S.A.* **1993**, *90*, 11762-11766. DOI: 10.1073/pnas.90.24.11762.

(112) Barkhuijsen, H.; De Beer, R.; Bovée, W.; van Ormondt, D. Retrieval of frequencies, amplitudes, damping factors, and phases from time-domain signals using a linear least-squares procedure. *J. Magn. Reson.* **1985**, *61*, 465-481. DOI: 10.1016/0022-2364(85)90187-8.

(113) Joo, T.; Jia, Y.; Yu, J.-Y.; Jonas, D. M.; Fleming, G. R. Dynamics in isolated bacterial light-harvesting antenna (LH2) of *Rhodobacter sphaeroides* at room temperature. *J. Phys. Chem.* **1996**, *100*, 2399-2409.

(114) Alvarez, J.-L.; Yartsev, A.; Åkesson, E.; Sundström, V. Resolving the turnover of the temperature dependence of the reaction rate in barrierless isomerization. *J. Phys. Chem. B* **1998**, *102*, 7651-7658.

(115) Sauer, M.; Angerer, B.; Han, K. T.; Zander, C. Detection and identification of single dye labeled mononucleotide molecules released from an optical fiber in a microcapillary: first steps towards a new single molecule DNA sequencing technique. *Phys. Chem. Chem. Phys.* **1999**, *1*, 2471-2477. DOI: 10.1039/a901411j.

(116) Halle, B. Protein hydration dynamics in solution: a critical survey. *Philos. Trans. R. Soc. London Ser. B* **2004**, *359*, 1207-1224. DOI: 10.1098/rstb.2004.1499.

(117) Pal, S. K.; Peon, J.; Bagchi, B.; Zewail, A. H. Biological water: femtosecond dynamics of macromolecular hydration. *J. Phys. Chem. B* **2002**, *106*, 12376-12395. DOI: 10.1021/jp0213506.

(118) Pal, S. K.; Peon, J.; Zewail, A. H. Biological water at the protein surface: dynamical solvation probed directly with femtosecond resolution. *Proc. Natl. Acad. Sci. U.S.A.* **2002**, *99*, 1763-1768. DOI: 10.1073/pnas.042697899.

(119) Ebbinghaus, S.; Kim, S. J.; Heyden, M.; Yu, X.; Heugen, U.; Gruebele, M.; Leitner, D. M.; Havenith, M. An extended dynamical hydration shell around proteins. *Proc. Natl. Acad. Sci. U.S.A.* **2007**, *104*, 20749-20752. DOI: 10.1073/pnas.0709207104.

(120) Creighton, T. E. The protein folding problem. In *Mechanisms of Protein Folding*; Creighton, T. E., Ed.; Oxford University Press: Oxford, 1994, p 1-25.

(121) Frauenfelder, H.; Sligar, S. G.; Wolynes, P. G. The energy landscapes and motions of proteins. *Science* **1991**, *254*, 1598-1603. DOI: 10.1126/science.1749933.

(122) Frauenfelder, H.; Wolynes, P. G. Biomolecules: Where the physics of complexity and simplicity meet. *Physics Today* **1994**, *47*, 58-64.

(123) Ansari, A.; Berendzen, J.; Bowne, S. F.; Frauenfelder, H.; Iben, I. E.; Sauke, T. B.; Shyamsunder, E.; Young, R. D. Protein states and proteinquakes. *Proc. Natl. Acad. Sci. U.S.A.* **1985**, *82*, 5000-5004. DOI: 10.1073/pnas.82.15.5000.

(124) Halle, B.; Davidovic, M. Biomolecular hydration: from water dynamics to hydrodynamics. *Proc. Natl. Acad. Sci. U.S.A.* **2003**, *100*, 12135-12140.

(125) Qiu, W.; Zhang, L.; Okobia, O.; Yang, Y.; Wang, L.; Zhong, D.; Zewail, A. H. Ultrafast solvation dynamics of human serum albumin: correlations with conformational transitions and site-selected recognition. *J. Phys. Chem. B* **2006**, *110*, 10540-10549. DOI: 10.1021/jp055989w.

(126) Carter, E. A.; Hynes, J. T. Solvation dynamics for an ion pair in a polar solvent: time-dependent fluorescence and photochemical charge transfer. *J. Chem. Phys.* **1991**, *94*, 5961-5979. DOI: 10.1063/1.460431.

(127) Rosenthal, S. J.; Xie, X.; Du, M.; Fleming, G. R. Femtosecond solvation dynamics in acetonitrile: observation of the inertial contribution to the solvent response. *J. Chem. Phys.* **1991**, *95*, 4715-4718. DOI: 10.1063/1.461742.

(128) Bagchi, B. Water dynamics in the hydration layer around proteins and micelles. *Chem. Rev.* **2003**, *105*, 3197-3219. DOI: 10.1021/cr020661+.

(129) Friesen, A. D.; Matyushov, D. V. Surface polarity and nanoscale solvation. *J. Phys. Chem. Lett.* **2012**, *3*, 3685-3689. DOI: 10.1021/jz301672e.

(130) Vanderkooi, J. M.; Adar, F.; Erecińska, M. Metallocytochromes *c*: characterization of electronic absorption and emission spectra of Sn^{4+} and Zn^{2+} cytochromes *c*. *Eur. J. Biochem.* **1976**, *64*, 381-387. DOI: 10.1111/j.1432-1033.1976.tb10312.x.

(131) Elias, H.; Chou, M. H.; Winkler, J. R. Electron-transfer kinetics of Zn-substituted cytochrome *c* and its $Ru(NH_3)_5$(Histidine-33) derivative. *J. Am. Chem. Soc.* **1988**, *110*, 429-434. DOI: 10.1021/ja00210a019.

(132) Ye, S.; Shen, C.; Cotton, T. M.; Kostić, N. M. Characterization of zinc-substituted cytochrome *c* by circular dichroism and resonance Raman spectroscopic

methods. *J. Inorg. Biochem.* **1997**, *65*, 219-226. DOI: 10.1016/S0162-0134(97)00001-9.

(133) Guo, X.; Bandyopadhyay, P.; Schilling, B.; Young, M. M.; Fujii, N.; Aynechi, T.; Guy, R. K.; Kuntz, I. D.; Gibson, B. W. Partial acetylation of lysine residues improves intraprotein cross-linking. *Anal. Chem.* **2008**, *80*, 951-960. DOI: 10.1021/ac701636w.

(134) Longuet‐Higgins, H. C.; Pople, J. A. Electronic spectral shifts of nonpolar molecules in nonpolar solvents. *J. Chem. Phys.* **1957**, *27*, 192-194. DOI: 10.1063/1.1743666.

(135) Fayer, M. D.; Levinger, N. E. Analysis of water in confined geometries and at interfaces. *Annu. Rev. Anal. Chem.* **2010**, *3*, 89-107. DOI: 10.1146/annurev-anchem-070109-103410.

(136) Bashkin, J. S.; McLendon, G.; Mukamel, S.; Marohn, J. Influence of medium dynamics on solvation and charge separation reactions: comparison of a simple alcohol and a protein "solvent". *J. Phys. Chem.* **1990**, *94*, 4757-4761. DOI: 10.1021/j100375a001.

(137) Pierce, D. W.; Boxer, S. G. Dielectric relaxation in a protein matrix. *J. Phys. Chem.* **1992**, *96*, 5560-5566. DOI: 10.1021/j100192a069.

(138) Pal, S. K.; Mandal, D.; Sukul, D.; Sen, S.; Bhattacharyya, K. Solvation dynamics of DCM in human serum albumin. *J. Phys. Chem. B* **2001**, *105*, 1438-1441. DOI: 10.1021/jp002368o.

(139) Cohen, B. E.; McAnaney, T. B.; Park, E. S.; Jan, Y. N.; Boxer, S. G.; Jan, L. Y. Probing protein electrostatics with a synthetic fluorescent amino acid. *Science* **2002**, *296*, 1700-1703. DOI: 10.1126/science.1069346.

(140) Lampa-Pastirk, S.; Beck, W. F. Polar solvation dynamics in Zn(II)-substituted cytochrome *c*: diffusive sampling of the energy landscape in the hydrophobic core and solvent-contact layer. *J. Phys. Chem. B* **2004**, *108*, 16288-16294. DOI: 10.1021/jp0488113.

(141) Sahu, K.; Mondal, S. K.; Ghosh, S.; Roy, D.; Bhattacharyya, K. Temperature dependence of solvation dynamics and anisotropy decay in a protein: ANS in bovine serum albumin. *J. Chem. Phys.* **2006**, *124*, 124909. DOI: 10.1063/1.2178782.

(142) Toptygin, D.; Gronenborn, A. M.; Brand, L. Nanosecond relaxation dynamics of protein GB1 identified by the time-dependent red shift in the fluorescence of tryptophan and 5-fluorotryptophan. *J. Phys. Chem. B* **2006**, *110*, 26292-26302. DOI: 10.1021/jp064528n.

(143) Abbyad, P.; Shi, X.; Childs, W.; McAnaney, T. B.; Cohen, B. E.; Boxer, S. G. Measurement of solvation responses at multiple sites in a globular protein. *J. Phys. Chem. B* **2007**, *111*, 8269-8276. DOI: 10.1021/jp0709104.

(144) Riter, R. E.; Edington, M. D.; Beck, W. F. Protein-matrix solvation dynamics in the *α* subunit of *C*-phycocyanin. *J. Phys. Chem.* **1996**, *100*, 14198-14205. DOI: 10.1021/jp960453j.

(145) Jordanides, X. J.; Lang, M. J.; Song, X.; Fleming, G. R. Solvation dynamics in protein environments studied by photon echo spectroscopy. *J. Phys. Chem. B* **1999**, *103*, 7995-8005. DOI: 10.1021/jp9910993.

(146) Matyushov, D. V. Nanosecond Stokes shift dynamics, dynamical transition, and gigantic reorganization energy of hydrated heme proteins. *J. Phys. Chem. B* **2011**, *115*, 10715-10724. DOI: 10.1021/jp200409z.

(147) Frank, H. A.; Cogdell, R. J. Carotenoids in photosynthesis. *Photochem. Photobiol.* **1996**, *63*, 257-264. DOI: 10.1111/j.1751-1097.1996.tb03022.x.

(148) Kreuger, B. P.; Scholes, G. D.; Jimenez, R.; Fleming, G. R. Electronic excitation transfer from carotenoid to bacteriochlorophyll in the purple bacterium *Rhodopseudomonas acidophila*. *J. Phys. Chem. B* **1998**, *102*, 2284-2292.

(149) Tavan, P.; Schulten, K. The low-lying electronic excitations in long polyenes: A PPP-MRD-CI study. *J. Chem. Phys.* **1986**, *85*, 6602-6609. DOI: 10.1063/1.451442.

(150) Klessinger, M.; Michl, J. *Excited states and photochemistry of organic molecules*; VCH Publishers: New York, 1995.

(151) Levine, B. G.; Ko, C.; Quenneville, J.; MartÍnez, T. J. Conical intersections and double excitations in time-dependent density functional theory. *Mol. Phys.* **2006**, *104*, 1039-1051. DOI: 10.1080/00268970500417762.

(152) Levine, B. G.; Martínez, T. J. Ab initio multiple spawning dynamics of excited butadiene: role of charge transfer. *J. Phys. Chem. A* **2009**, *113*, 12815-12824. DOI: 10.1021/jp907111u

(153) Zhang, J.-P.; Inaba, T.; Watanabe, Y.; Koyama, Y. Sub-picosecond time-resolved absorption spectroscopy of all-*trans*-neurosporene in solution and bound to the LH2 complex from *Rhodobacter sphaeroides* G1C. *Chem. Phys. Lett.* **2000**, *331*, 154-162. DOI: 10.1016/S0009-2614(00)01165-9.

(154) Xu, Q.-H.; Ma, Y.-Z.; Stiopkin, I. V.; Fleming, G. R. Wavelength-dependent resonant homodyne and heterodyne transient grating spectroscopy with a diffractive optics method: solvent effect on the third-order signal. *J. Chem. Phys.* **2002**, *116*, 9333-9340. DOI: 10.1063/1.1473653.

(155) Moran, A. M.; Nome, R. A.; Scherer, N. F. Resolving the emission times of solute and solvent four-wave mixing signals by spectral interferometry. *J. Chem. Phys.* **2006**, *125*, 31101. DOI: 10.1063/1.2217940.

(156) Gallagher, S. M.; Albrecht, A. W.; Hybl, J. D.; Landin, B. L.; Rajaram, B.; Jonas, D. M. Heterodyne detection of the complete electric field of femtosecond four-wave mixing signals. *J. Opt. Soc. Am. B* **1998**, *15*, 2338-2345. DOI: 10.1364/JOSAB.15.002338.

(157) Enriquez, M. M.; Fuciman, M.; LaFountain, A. M.; Wagner, N. L.; Birge, R. R.; Frank, H. A. The intramolecular charge transfer state in carbonyl-containing polyenes and carotenoids. *J. Phys. Chem. B* **2010**, *114*, 12416-12426. DOI: 10.1021/jp106113h.

(158) Mukamel, S. *Principles of Nonlinear Optical Spectroscopy*; Oxford University Press: New York, 1995. ISBN: 0-19-509278-3.

(159) Hybl, J. D.; Ferro, A. A.; Jonas, D. M. Two-dimensional Fourier transform electronic spectroscopy. *J. Chem. Phys.* **2001**, *115*, 6606-6622. DOI: 10.1063/1.1398579.

(160) Gumy, J.-C.; Nicolet, O.; Vauthey, E. Investigation of the solvation dynamics of an organic dye in polar solvents using the femtosecond transient grating technique. *J. Phys. Chem. A* **1999**, *103*, 10737-10743. DOI: 10.1021/jp992265+.

(161) Wasielewski, M. R.; Kispert, L. D. Direct measurement of the lowest excited singlet state lifetime of all-trans-β-carotene and related carotenoids. *Chem. Phys. Lett.* **1986**, *128*, 238-243. DOI: 10.1016/0009-2614(86)80332-3.

(162) Hershberger, M. A.; Moran, A. M.; Scherer, N. F. New insights into response functions of liquids by electric field-resolved polarization emission time measurements. *J Phys Chem B* **2011**, *115*, 5617-5624. DOI: 10.1021/jp111796d.

(163) Rodriguez, J.; Holten, D. Ultrafast vibrational dynamics of a photoexcited metalloporphyrin. *J. Chem. Phys.* **1989**, *91*, 3525-3531. DOI: 10.1063/1.456883.

(164) Xu, Q.-H.; Ma, Y.-Z.; Fleming, G. R. Heterodyne detected transient grating spectroscopy in resonant and non-resonant systems using a simplified diffractive optics method. *Chem. Phys. Lett.* **2001**, *338*, 254. DOI: 10.1016/S0009-2614(01)00281-0.

(165) Christensson, N.; Milota, F.; Nemeth, A.; Pugliesi, I.; Riedle, E.; Sperling, J.; Pullerits, T.; Kauffman, H. F.; Hauer, J. Electronic double-quantum coherences and their impact on ultrafast spectroscopy: the example of β-carotene. *J. Phys. Chem. Lett.* **2010**, *1*, 3366-3370. DOI: 10.1021/jz101409r|J.

(166) Rondonuwu, F. S.; Watanabe, Y.; Zhang, J.-P.; Furuichi, K.; Koyama, Y. Internal-conversion and radiative-transition processes among the $1B_u^+$, $1B_u^-$ and $2A_g^-$ states of all-*trans*-neurosporene as revealed by subpicosecond time-resolved Raman spectroscopy. *Chem. Phys. Lett.* **2002**, *357*, 376-384. DOI: 10.1016/S0009-2614(02)00491-8.

(167) Sugisaki, M.; Yanagi, K.; Cogdell, R. J.; Hashimoto, H. Unified explanation for linear and nonlinear optical responses in β-carotene: A sub-20-fs degenerate four-wave mixing spectroscopic study. *Phys. Rev. B* **2007**, *75*, 155110. DOI: 10.1103/PhysRevB.75.155110.

(168) Sugisaki, M.; Fujiwara, M.; Yanagi, K.; Cogdell, R. J.; Hashimoto, H. Four-wave mixing signals from β-carotene and its *n* = 15 homologue. *Photosynth. Res.* **2008**, *95*, 299-308. DOI: 10.1007/s11120-007-9265-y.

(169) Fujiwara, M.; Yamauchi, K.; Sugisaki, M.; Gall, A.; Robert, B.; Cogdell, R.; Hashimoto, H. Energy dissipation in the ground-state vibrational manifolds of β-carotene homologues: A sub-20-fs time-resolved transient grating spectroscopic study. *Phys. Rev. B* **2008**, *77*, 205118. DOI: 10.1103/PhysRevB.77.205118.

(170) Garavelli, M.; Celani, P.; Bernardi, F.; Robb, M. A.; Olivucci, M. The $C_5H_6NH_2^+$ protonated Shiff base: an *ab initio* minimal model for retinal photoisomerization. *J. Am. Chem. Soc.* **1997**, *119*, 6891-6901. DOI: 10.1021/ja9610895.

(171) Garavelli, M.; Vreven, T.; Celani, P.; Bernardi, F.; Robb, M. A.; Olivucci, M. Photoisomerization path for a realistic retinal chromophore model: the nonatetraeniminium cation. *J. Am. Chem. Soc.* **1998**, *120*, 1285-1288. DOI: 10.1021/ja972695i.

(172) Garavelli, M.; Negri, F.; Olivucci, M. Initial excited-state relaxation of the isolated 11-cis protonated Schiff base of retinal: evidence for in-plane motion from ab initio quantum chemical simulation of the resonance Raman spectrum. *J. Am. Chem. Soc.* **1999**, *121*, 1023-1029. DOI: 10.1021/ja981719y.

(173) Robb, M. A.; Olivucci, M. Photochemical processes: potential energy surface topology and rationalization using VB arguments. *J. Photochem. Photobiol. A* **2001**, *144*, 237-243. DOI: 10.1016/S1010-6030(01)00453-1.

(174) Ruiz, D. S.; Cembran, A.; Garavelli, M.; Olivucci, M.; Fuß, W. Structure of the conical intersections driving the *cis–trans* photoisomerization of conjugated molecules. *Photochem. Photobiol.* **2002**, *76*, 622-633. DOI: 10.1562/0031-8655(2002)0760622SOTCID2.0.CO2.

(175) Kosumi, D.; Fujiwara, M.; Fujii, R.; Cogdell, R. J.; Hashimoto, H.; Yoshizawa, M. The dependence of the ultrafast relaxation kinetics of the S_2 and S_1 states in β-carotene homologs and lycopene on conjugation length studied by femtosecond

time-resolved absorption and Kerr-gate fluorescence spectroscopies. *J. Chem. Phys.* **2009**, *130*, 214506. DOI: 10.1063/1.3147008.

(176) Siebert, T.; Engel, V.; Materny, A.; Kiefer, W.; Schmitt, M. Probing the kinetics of a nonadiabatic transition initiating out of vibrationally excited as well as ground state modes with femtosecond time-resolved transient gratings. *J. Phys. Chem. A* **2003**, *107*, 8355-8362. DOI: 10.1021/jp022650q.

(177) Förster, T. Zwischenmolekulare Energiewanderung und Fluoreszenz. *Annu. Physik* **1948**, *2*, 55-75.

(178) Förster, T. Intermolecular energy transfer and fluorescence. *Annu. Phys.* **1968**, *2*, 55-75.

(179) Dexter, D. L. A theory of sensitized luminescence in solids. *J. Chem. Phys.* **1953**, *21*, 836. DOI: 10.1063/1.1699044

(180) Hsu, C.-P.; Walla, P. J.; Head-Gordon, M.; Fleming, G. R. The role of the S_1 state of carotenoids in photosynthetic energy transfer: the light-harvesting complex II of purple bacteria. *J. Phys. Chem. B* **2001**, *105*, 11016-11025.

(181) Mimuro, M.; Tamai, N.; Ishimaru, T.; Yamazaki, I. Characteristic fluorescence components in photosynthetic pigment system of a marine dinoflagellate, *Protogonyaulax tamarensis*, and excitation energy flow among them. Studies by means of steady-state and time-resolved fluorescence spectroscopy. *Biochim. Biophys. Acta* **1990**, *1016*, 280. DOI: 10.1016/0005-2728(90)90070-K.

(182) Frank, H. A.; Bautista, J. A.; Josue, J.; Pendon, Z.; Hiller, R. G.; Sharples, F. P.; Gosztola, D.; Wasielewski, M. R. Effect of the solvent environment on the spectroscopic properties and dynamics of the lowest excited states of carotenoids. *J. Phys. Chem. B* **2000**, *104*, 4569-4577. DOI: 10.1021/jp000079u.

(183) Bautista, J. A.; Connors, R. E.; Raju, B. B.; Hiller, R. G.; Sharples, F. P.; Gosztola, D.; Wasielewski, M. R.; Frank, H. A. Excited state properties of peridinin: Observation of a solvent dependence of the lowest excited singlet state lifetime and spectral behavior unique among carotenoids. *J. Phys. Chem. B* **1999**, *103*, 8751-8758. DOI: 10.1021/jp9916135.

(184) Vaswani, H. M.; Hsu, C. P.; Head-Gordon, M.; Fleming, G. R. Quantum chemical evidence for an intramolecular charge-transfer state in the carotenoid peridinin of peridinin-chlorophyll-protein. *J. Phys. Chem. B* **2003**, *107*, 7940-7946. DOI: 10.1021/jp030086t.

(185) Zigmantas, D.; Polívka, T.; Hiller, R. G.; Yartsev, A.; Sundström, V. Spectroscopic and dynamic properties of the peridinin lowest singlet excited states. *J. Phys. Chem. A* **2001**, *105*, 10296-10306. DOI: 10.1021/jp010022n.

(186) Zigmantas, D.; Hiller, R. G.; Yartsev, A.; Sundström, V.; Polívka, T. Dynamics of excited states of the carotenoid peridinin in polar solvents: Dependence on excitation wavelength, viscosity, and temperature. *J. Phys. Chem. B* **2003**, *107*, 5339-5348.

(187) Zigmantas, D.; Hiller, R. G.; Sharples, F. P.; Frank, H. A.; Sundström, V.; Polívka, T. Effect of a conjugated carbonyl group on the photophysical properties of carotenoids. *Phys. Chem. Chem. Phys.* **2004**, *6*, 3009-3016.

(188) Herek, J. L.; Wendling, M.; He, Z.; Polívka, T.; Garcia-Asua, G.; Cogdell, R. J.; Hunter, C. N.; van Grondelle, R.; Sundström, V.; Pullerits, T. Ultrafast carotenoid band shifts: Experiment and theory. *J. Phys. Chem. B* **2004**, *108*, 10398-10403.

(189) Papagiannakis, E.; Larsen, D. S.; van Stokkum, I. H. M.; Vengris, M.; Hiller, R. G.; van Grondelle, R. Resolving the excited state equilibrium of peridinin in solution. *Biochemistry* **2004**, *43*, 15303-15309. DOI: 10.1021/bi047977r.

(190) Wild, D. A.; Winkler, K.; Stalke, S.; Oum, K.; Lenzer, T. Extremely strong solvent dependence of the S_1 -> S_0 internal conversion lifetime of 12'-apo-β-caroten-12'-al. *Phys. Chem. Chem. Phys.* **2006**, *8*, 2499-2505.

(191) Stalke, S.; Wild, D. A.; Lenzer, T.; Kopczynski, M.; Lohse, P. W.; Oum, K. Solvent-dependent ultrafast internal conversion dynamics of n'-apo-β-carotenoic-n'-acids (n = 8, 10, 12). *Phys. Chem. Chem. Phys.* **2008**, *10*, 2180-2188.

(192) Kopczynski, M.; Ehlers, F.; Lenzer, T.; Oum, K. Evidence for an intramolecular charge transfer state in 12'-apo-β-caroten-12'-al and 8'-apo-β-caroten-8'-al: Influence of solvent polarity and temperature. *J. Phys. Chem. A* **2007**, *111*, 5370-5381.

(193) Ehlers, F.; Wild, D. A.; Lenzer, T.; Oum, K. Investigation of the S_1/ICT -> S_0 internal conversion lifetime of 4'-apo-β-caroten-4'-al and 8'-apo-β-caroten-8'-al: Dependence on conjugation length and solvent polarity. *J. Phys. Chem. A* **2007**, *111*, 2257-2265.

(194) Premvardhan, L.; Papagiannakis, E.; Hiller, R. G.; van Grondelle, R. The charge-transfer character of the $S_0 \rightarrow S_2$ transition in the carotenoid peridinin is revealed by Stark spectroscopy. *J. Phys. Chem. B* **2005**, *109*, 15589-15597. DOI: 10.1021/jp052027g.

(195) Kusumoto, T.; Horibe, T.; Kajikawa, T.; Hasegawa, S.; Iwashita, T.; Cogdell, R. J.; Birge, R. R.; Frank, H. A.; Katsumura, S.; Hashimoto, H. Stark absorption spectroscopy of peridinin and allene-modified analogues. *Chem. Phys.* **2010**, *373*, 71. DOI: 10.1016/j.chemphys.2010.01.018.

(196) Polívka, T.; Hiller, R. G.; Frank, H. A. Spectroscopy of the peridinin–chlorophyll *a* protein: Insight into light-harvesting strategy of marine algae. *Arch. Biochem. Biophys.* **2007**, *458*, 111-120. DOI: 10.1016/j.abb.2006.10.006.

(197) Guillard, R. R. L. Culture of phytoplankton for feeding marine invertebrates. In *Culture of Marine Invertebrate Animals*; Smith, W. L., Chanley, M. H., Eds.; Plenum Press: New York, 1975.

(198) Steck, K.; Wacker, T.; Welte, W.; Sharples, F. P.; Hiller, R. G. Crystallization and preliminary X-ray analysis of peridinin–chlorophyll *a* protein from *Amphidinium carterae*. *FEBS Lett.* **1990**, *268*, 48-50. DOI: 10.1016/0014-5793(90)80969-P.